



U.S. Department of Transportation
Federal Highway Administration

Errata

Date: 10/17/2018

Issuing Office: Federal Highway Administration—Office of Research,
Development, and Technology

Address: Turner-Fairbank Highway Research Center
6300 Georgetown Pike, McLean, VA 22101

Name of Document: Advanced Methodology to Assess Riprap Rock Stability at
Bridge Piers and Abutments

FHWA Publication No.: FHWA-HRT-17-054

The following changes were made to the document after publication on the Federal Highway Administration website:

Location	Incorrect Values	Corrected Values
Page 2 Editorial Correction	Source information for Figure 1 missing.	Added source information, Source: Modified by FHWA from NCHRP report 568. See Acknowledgment page.
Page 10 Editorial Correction	In addition, rocks around the upstream corner of first the abutment were colored...	In addition, rocks around the upstream corner of the first abutment were colored...
Page 88 Editorial Correction	No reference 43.	Added reference 43. Lauchlan, C.S. (1999). Pier Scour Countermeasures, Ph.D. Thesis, University of Auckland, Auckland, NZ.
Page 89 Editorial Correction	No Acknowledgment page.	Added Acknowledgment page. Figure 1 was modified by FHWA from figure 2.5 of NCHRP report 568, which in turn was modified from an original graph in C.S. Lauchlan's thesis, "Pier Scour Countermeasures." ⁴³

Advanced Methodology to Assess Riprap Rock Stability at Bridge Piers and Abutments

PUBLICATION NO. FHWA-HRT-17-054

OCTOBER 2017



U.S. Department of Transportation
Federal Highway Administration

Research, Development, and Technology
Turner-Fairbank Highway Research Center
6300 Georgetown Pike
McLean, VA 22101-2296

FOREWORD

Riprap is one of the most common materials used to protect bridge abutment and pier foundations from scour. A key element of the design of riprap countermeasures is rock sizing, which is based on equations generally derived from simplified laboratory experiments. In this study, an advanced modeling approach is developed and applied to evaluate rock stability. The advantage of this approach is that it can incorporate site-specific conditions that complicate riprap design. This report describes this advanced, numerical modeling procedure for analyzing the stability of riprap at bridge abutments and piers. The report will be useful for designers and engineers responsible for protecting bridge foundations. The study described in this report was conducted at the Federal Highway Administration's (FHWA) Turner-Fairbank Highway Research Center (TFHRC) J. Sterling Jones Hydraulics Laboratory.

Cheryl Allen Richter, P.E., Ph.D.
Director, Office of Infrastructure
Research and Development

Notice

This document is disseminated under the sponsorship of the U.S. Department of Transportation (USDOT) in the interest of information exchange. The U.S. Government assumes no liability for the use of the information contained in this document. This report does not constitute a standard, specification, or regulation.

The U.S. Government does not endorse products or manufacturers. Trademarks or manufacturers' names appear in this report only because they are considered essential to the objective of the document.

Quality Assurance Statement

The Federal Highway Administration (FHWA) provides high-quality information to serve Government, industry, and the public in a manner that promotes public understanding. Standards and policies are used to ensure and maximize the quality, objectivity, utility, and integrity of its information. FHWA periodically reviews quality issues and adjusts its programs and processes to ensure continuous quality improvement.

TECHNICAL DOCUMENTATION PAGE

1. Report No. FHWA-HRT-17-054		2. Government Accession No.		3. Recipient's Catalog No.	
4. Title and Subtitle Advanced Methodology to Assess Riprap Rock Stability at Bridge Piers and Abutments		5. Report Date October 2017		6. Performing Organization Code	
		7. Author(s) Oscar Suaznabar, Cezary Bojanowski, Steven A. Lottes, Jerry Shen, Kornel Kerenyi, and Roger Kilgore		8. Performing Organization Report No.	
9. Performing Organization Name and Address GENEX SYSTEMS, LLC 11848 Rock Landing Drive, Suite 303 Newport News, VA 23606		10. Work Unit No. (TRAIS)		11. Contract or Grant No. DTFH61-11-D00010-T-11005	
		12. Sponsoring Agency Name and Address Office of Infrastructure Research and Development Federal Highway Administration 6300 Georgetown Pike McLean, VA 22101-2296		13. Type of Report and Period Covered Pooled Fund Study Report October 2011–September 2016	
		14. Sponsoring Agency Code			
15. Supplementary Notes The Contracting Officer's Representative (COR) was Kornel Kerenyi (HRDI-40).					
16. Abstract The objectives of this research study were to: (1) assess whether detailed fluid structure interaction (FSI) modeling can inform evaluation of rock riprap movement for both the analysis of existing riprap aprons and for the design of new riprap aprons; and (2) develop recommendations for the design, installation, and monitoring of riprap aprons at bridge piers and abutments, where feasible. A new advanced computational methodology for assessing failure risk of geometrically complex riprap installations was developed for this study. The study demonstrated that detailed FSI modeling can inform evaluation of rock riprap movement for both the analysis of existing riprap aprons and for the design of new riprap aprons. The approach solved the FSI problem for the onset of rock riprap motion using weakly coupled computational fluid dynamics and computational structural mechanics software. The flow threshold for the onset of motion of riprap rocks was computed for a set of representative riprap rocks for both simplified laboratory and complex field conditions. Physical laboratory experiments were used to validate the numerical procedures. The FSI approach was also tested on a complex field case study of a riprap installation at a pier for a bridge over the Middle Fork of the Feather River. While the case study application was considered successful, the approach is limited by its high costs and limited availability. Therefore, good candidate applications for using FSI analysis to assess new or retrofit riprap installations would be those where the project cost is significant or the risks of failure are catastrophic. The study also identified recommendations for improving the design, installation, and monitoring of riprap apron installations at bridge piers and abutments, where feasible. These included: (1) verifying as-built conditions for assuring that the intended level of protection has been achieved, (2) inspecting for changes in stream morphology that may significantly change conditions from those anticipated at design, (3) recording the date of rock riprap installations and monitoring the performance of the installations after major floods, (4) applying sonar technologies for riprap monitoring, and (5) avoiding rock riprap installations for new bridge piers as they are not recommended by FHWA policy. The FSI numerical modeling approach has promise for supporting the design and evaluation of riprap installations for bridge abutments and piers. As computer capabilities increase and more detailed representations of rock riprap installations become more practical, the approach should continue to increase in its utility.					
17. Key Words Riprap, countermeasure, bridge pier, bridge abutment, fluid-structure interaction, computational fluid dynamics, computational structural mechanics, numerical modeling, flume modeling of riprap			18. Distribution Statement No restrictions.		
19. Security Classif. (of this report) Unclassified		20. Security Classif. (of this page) Unclassified		21. No. of Pages 97	22. Price

SI* (MODERN METRIC) CONVERSION FACTORS

APPROXIMATE CONVERSIONS TO SI UNITS

Symbol	When You Know	Multiply By	To Find	Symbol
LENGTH				
in	inches	25.4	millimeters	mm
ft	feet	0.305	meters	m
yd	yards	0.914	meters	m
mi	miles	1.61	kilometers	km
AREA				
in ²	square inches	645.2	square millimeters	mm ²
ft ²	square feet	0.093	square meters	m ²
yd ²	square yard	0.836	square meters	m ²
ac	acres	0.405	hectares	ha
mi ²	square miles	2.59	square kilometers	km ²
VOLUME				
fl oz	fluid ounces	29.57	milliliters	mL
gal	gallons	3.785	liters	L
ft ³	cubic feet	0.028	cubic meters	m ³
yd ³	cubic yards	0.765	cubic meters	m ³
NOTE: volumes greater than 1000 L shall be shown in m ³				
MASS				
oz	ounces	28.35	grams	g
lb	pounds	0.454	kilograms	kg
T	short tons (2000 lb)	0.907	megagrams (or "metric ton")	Mg (or "t")
TEMPERATURE (exact degrees)				
°F	Fahrenheit	5 (F-32)/9 or (F-32)/1.8	Celsius	°C
ILLUMINATION				
fc	foot-candles	10.76	lux	lx
fl	foot-Lamberts	3.426	candela/m ²	cd/m ²
FORCE and PRESSURE or STRESS				
lbf	poundforce	4.45	newtons	N
lbf/in ²	poundforce per square inch	6.89	kilopascals	kPa

APPROXIMATE CONVERSIONS FROM SI UNITS

Symbol	When You Know	Multiply By	To Find	Symbol
LENGTH				
mm	millimeters	0.039	inches	in
m	meters	3.28	feet	ft
m	meters	1.09	yards	yd
km	kilometers	0.621	miles	mi
AREA				
mm ²	square millimeters	0.0016	square inches	in ²
m ²	square meters	10.764	square feet	ft ²
m ²	square meters	1.195	square yards	yd ²
ha	hectares	2.47	acres	ac
km ²	square kilometers	0.386	square miles	mi ²
VOLUME				
mL	milliliters	0.034	fluid ounces	fl oz
L	liters	0.264	gallons	gal
m ³	cubic meters	35.314	cubic feet	ft ³
m ³	cubic meters	1.307	cubic yards	yd ³
MASS				
g	grams	0.035	ounces	oz
kg	kilograms	2.202	pounds	lb
Mg (or "t")	megagrams (or "metric ton")	1.103	short tons (2000 lb)	T
TEMPERATURE (exact degrees)				
°C	Celsius	1.8C+32	Fahrenheit	°F
ILLUMINATION				
lx	lux	0.0929	foot-candles	fc
cd/m ²	candela/m ²	0.2919	foot-Lamberts	fl
FORCE and PRESSURE or STRESS				
N	newtons	0.225	poundforce	lbf
kPa	kilopascals	0.145	poundforce per square inch	lbf/in ²

*SI is the symbol for the International System of Units. Appropriate rounding should be made to comply with Section 4 of ASTM E380.
(Revised March 2003)

TABLE OF CONTENTS

CHAPTER 1. INTRODUCTION	1
CHAPTER 2. LITERATURE REVIEW	5
CHAPTER 3. PHYSICAL MODELING	7
TILTING FLUME	7
TEST SECTION	8
EXPERIMENTAL PROCEDURE	10
Riprap Incipient Motion.....	10
Riprap Apron Condition after Failure.....	11
CHAPTER 4. NUMERICAL MODELING: TOOL DEVELOPMENT	17
INTRODUCTION AND OBJECTIVES	17
VALIDATION OF THE METHODOLOGY	19
Model Geometry.....	19
Flow Conditions.....	22
Model Results.....	23
CHAPTER 5. NUMERICAL MODELING: CASE STUDY	31
SITE CONDITIONS AND RIPRAP RISK ASSESSMENT	31
MODEL DEVELOPMENT FOR THE MIDDLE FORK FEATHER RIVER	32
Domain and Mesh.....	34
Riprap Geometry Development.....	37
<i>Geometry Based on Design Drawings</i>	37
<i>Geometry Based on Field Validation</i>	37
<i>Movable Rock Placement</i>	41
COMPARISON OF CFD AND 2D MODEL HYDRAULICS	41
ANALYSIS AND RESULTS	43
Results of the CFD Analyses.....	43
Results of the FSI Analyses.....	46
CHAPTER 6. CONCLUSIONS AND RECOMMENDATIONS	53
APPENDIX A. ANNOTATED BIBLIOGRAPHY	55
RIPRAP AT BRIDGE PIERS	55
RIPRAP AT BRIDGE ABUTMENTS OR IN STREAM CHANNELS	64
APPENDIX B. COUPLING AND VALIDATION OF THE FSI MODELS	69
COUPLING METHODOLOGIES FOR SOLVING FSI PROBLEMS	69
The Fluid and Structural Domains.....	69
Methodologies of Coupling Codes.....	70
Workflow of the File-Based Data Exchange with Weak Coupling.....	71
Challenges of Commercial Software and an Overset Mesh Alternative.....	74
APPLICATION OF THE METHODOLOGY TO A SIMPLE RIPRAP CASE	77
VERIFICATION OF THE COUPLING MECHANISM BY COMPARISON WITH A STAR-CCM+/ABAQUS BENCHMARK FSI PROBLEM	82
REFERENCES	85
ACKNOWLEDGMENT	89

LIST OF FIGURES

Figure 1. Graph. Comparison of riprap sizing curves at a rectangular pier	2
Figure 2. Illustration. FHWA tilting flume	7
Figure 3. Photo. Automated flume carriage in the TFHRC Hydraulics Laboratory	8
Figure 4. Photo. ADV probe	8
Figure 5. Sketch. Plan view of the test section	9
Figure 6. Sketch. Cross-section view of the test section.....	9
Figure 7. Photos. Riprap installation.....	10
Figure 8. Photo. Riprap apron installation for testing.....	10
Figure 9. Photos. Shear failure sequence for riprap apron installed flush with channel bed.....	13
Figure 10. Photos. Shear failure sequence for riprap installed on a slope against the abutment face	14
Figure 11. Graphic. Bathymetry of the riprap apron after failure in isometric view	14
Figure 12. Photo. After rock shear failure at the upstream corner of the abutment.....	15
Figure 13. Sketch. Plan view prototype domain	19
Figure 14. Sketch. Cross-section view of the prototype domain	20
Figure 15. Graphics. Rock layout in the CFD model	21
Figure 16. Graphics. Positions of movable rocks	22
Figure 17. Graphic. Velocity profile in a horizontal slice just above the riprap rocks with an inlet velocity of 4.27 ft/s (1.3 m/s).....	24
Figure 18. Graphic. Location of the rocks with the highest forces in a CFD analysis	24
Figure 19. Graph. Initial stabilization of vertical forces on movable rocks	25
Figure 20. Graphic. Definition of forces on a single rock	27
Figure 21. Graphics. FSI simulation for an inlet velocity of 4.27 ft/s (1.3 m/s).....	28
Figure 22. Graphics. FSI simulation for an inlet velocity of 4.59 ft/s (1.4 m/s).....	28
Figure 23. Graphics. FSI simulation for an inlet velocity of 4.92 ft/s (1.5 m/s).....	29
Figure 24. Photo. Historic, realigned, and current channel alignment	31
Figure 25. Photo. River bathymetry before installation of the riprap.....	32
Figure 26. Photo. Rock layout design for protection of pier 3	33
Figure 27. Photo. Riprap installation near pier 3 (August 2012).....	33
Figure 28. Photo. River bathymetry in 2013 after riprap installation.....	34
Figure 29. Schematic. CFD model surface characterization.....	35
Figure 30. Graphic. CFD model boundaries	35
Figure 31. Graphic. Surface mesh of the riverbed in CFD model	36
Figure 32. Graphic. Cross-section through the finite volume mesh used for the CFD model.....	36
Figure 33. Graphic. Cross-section through the subregion used in the FSI computations.....	37
Figure 34. Drawing. Design drawing (typical section) of riprap around pier 3.....	38
Figure 35. Drawing. Design drawing (section B-B) of riprap around pier 3.....	38
Figure 36. Graphic. Geometry of the riprap used in the CFD model	38
Figure 37. Image. Sonar image of pier 3 with installed riprap	39
Figure 38. Graphic. The extent of the riprap derived from the sonar bed scan	40
Figure 39. Graphic. Extent of riprap in the updated CFD model with movable rocks	40
Figure 40. Graphic. Placement of movable rocks around the pier.....	41
Figure 41. Graph. Depth-averaged velocity estimates under the bridge (looking upstream)	42
Figure 42. Graphic. Location of the rocks with the highest forces in CFD analysis	43

Figure 43. Graphic. Water surface (velocity overlain) for condition of 1.6 times the 100-year flood	46
Figure 44. Graphic. Velocity vectors on the interface between the FSI subregion and the CFD domain.....	47
Figure 45. Graphic. Velocity vectors on the plane just above the rocks	47
Figure 46. Graphics. FSI simulation for the 100-year discharge.....	48
Figure 47. Graphics. FSI simulation for 1.1 times the 100-year discharge	50
Figure 48. Graphics. FSI simulation for 1.2 times the 100-year discharge	50
Figure 49. Schematics. Stages of FSI mesh morphing	69
Figure 50. Sketch. Definition of the domains for FSI analysis of riprap stability	70
Figure 51. Flowchart. Weak FSI coupling scheme.....	71
Figure 52. Flowchart. Strong FSI coupling scheme	72
Figure 53. Flowchart. Implementation of coupling workflow between STAR-CCM+ and LS-DYNA.....	73
Figure 54. Schematics. Stages in the coupled simulation for water induced rock motion	75
Figure 55. Graphic. Rock representation with feature curves created on all edges of the mesh	76
Figure 56. Graphic. Surface triangulated representation of a rock.....	77
Figure 57. Graphics. Test CFD models	78
Figure 58. Equation. Laursen’s equation for critical velocity	79
Figure 59. Equation. Neill’s equation for critical velocity	80
Figure 60. Graphics. Time series for layout 1 at an inlet velocity of 9.8 ft/s (3.0 m/s).....	81
Figure 61. Graphics. Time series for layout 2 at an inlet velocity of 9.8 ft/s (3.0 m/s).....	82
Figure 62. Schematic. CFD domain and grid for analysis of flexible plate protruding into the flow setup for FSI analysis coupling with LS-DYNA.....	83
Figure 63. Schematics. Morphed mesh at maximum plate deflection.....	84
Figure 64. Graphs. Plate deflection.....	84

LIST OF TABLES

Table 1. Flow conditions for flume experiments12
Table 2. Forces on ten movable rocks with varying inlet velocities.....26
Table 3. Comparison of physical experiments and computational simulations.....29
Table 4. Comparison of 3D and 2D modeling results for the 100-year discharge42
Table 5. Forces on the critical rocks45

LIST OF ABBREVIATIONS AND SYMBOLS

Abbreviations

2D	two-dimensional
3D	three-dimensional
AASHTO	American Association of State Highway and Transportation Officials
ADV	Acoustic Doppler Velocimeter
ALE	Arbitrary Lagrangian-Eulerian
ASCE	American Society of Civil Engineers
Caltrans	California Department of Transportation
CD-Adapco	Computation Dynamics—Analysis and Design Application Company
CFD	computational fluid dynamics
CSM	computational structural mechanics
CUR	Center for Civil Engineering Research and Codes (translated from Dutch)
DG	<i>Design Guideline</i>
DOT	Department of Transportation
FHWA	Federal Highway Administration
FSI	fluid structure interaction
GPS	Global Positioning System
HEC	Hydraulic Engineering Circular
LSTC	Livermore Software Technology Corporation
NCHRP	National Cooperative Highway Research Program
NHI	National Highway Institute
NTSB	National Transportation Safety Board
NYSTA	New York State Thruway Authority
RANS	Reynolds-Averaged Navier-Stokes
RSP	rock slope protection
RWS	Rijkswaterstaat, Dutch Public Works Department (translated from Dutch)
TFHRC	Turner-Fairbank Highway Research Center
TRACC	Transportation Research and Analysis Computing Center
TRB	Transportation Research Board
USGS	United States Geological Survey
VOF	volume of fluid

Symbols

D_{50}	median particle (rock) size (ft (m))
Fr	Froude number (dimensionless)
i_m	iteration index (dimensionless)
K_U	unit conversion constant (varies with each equation)
l_1	abutment length (ft (m))
l_2	abutment width (ft (m))
m	number of structural solver time steps within a fluid solver time step (dimensionless)
n	time step index (dimensionless)
t	riprap apron thickness (ft (m))
V_1	approach velocity (ft/s (m/s))
V_2	contracted section velocity (ft/s (m/s))
V_{CL}	critical velocity estimated from Laursen's equation (ft/s (m/s))
V_{CN}	critical velocity estimated from Neill's equation (ft/s (m/s))
W_1	approach flow width (ft (m))
W_2	contracted (bridge opening) width (ft (m))
W_R	riprap extent (ft (m))
y	flow depth (ft (m))
y_1	approach flow depth (ft (m))
y_2	contraction flow depth (ft (m))
δt_f	fluid solver time step (s)
δt_s	structural solver time step (s)
Γ	boundary condition (dimensionless)
Ω_f	fluid occupying space (dimensionless)
Ω_s	solid body occupying space (dimensionless)

CHAPTER 1. INTRODUCTION

Local scour at bridge piers and abutments is a potential safety hazard of major concern to transportation agencies. If scour at a bridge pier or abutment can adversely affect the stability of a bridge, scour countermeasures to protect the bridge should be considered. Rock riprap is a common countermeasure used to prevent or reduce scour. While the Federal Highway Administration (FHWA) does not recommend riprap as a design countermeasure for piers on new bridges, it can be used for new bridge abutments. Rock riprap can also be used as a remedial measure for scour at piers and abutments for existing bridges.

Current riprap design methodologies and scour evaluation procedures provide a threshold size of rock that is anticipated to be stable under a pre-determined design condition. These methods are intended to be conservative in order to be useful for a wide variety of field conditions.

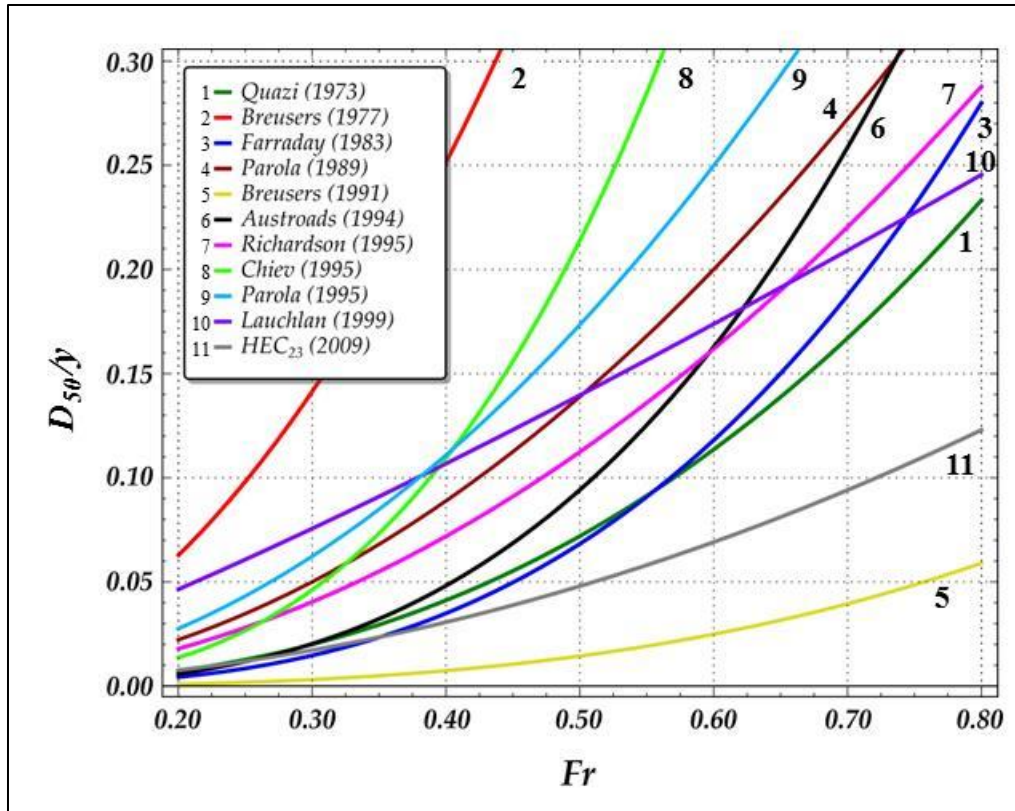
The sizing of riprap in scour countermeasure design procedures is based primarily on limited field observations and scaled laboratory tests under controlled conditions. FHWA's Hydraulic Engineering Circular No. 23 (HEC-23) *Bridge Scour and Stream Instability Countermeasures, Experience, Selection, and Design Guidelines* includes a formula that is functionally equivalent to the 1936 Isbash formula that provides a median rock size (D_{50}) based on the water depth (y) at the pier and the Froude number (Fr).⁽¹⁾ The HEC-23 formula includes a multiplicative factor on the mean velocity intended to account for higher instantaneous velocities resulting from increased turbulence intensity for pier shapes that are not simple cylinders.

However, because riprap sizing formulas are based on limited data, there is uncertainty and variation in the equations for sizing riprap. For example, there is a large spread in the design median rock size using formulas for piers proposed between 1973 and 1999. A comparison based on work by Lagasse et al. is summarized in figure 1.⁽²⁾ As is apparent in the figure, most equations yield larger values than the HEC-23 approach.

The methods also do not provide a site-specific understanding of when rocks might become displaced especially if the stream morphology or hydrology has changed from the time of design. Therefore, advanced computational mechanics techniques might offer benefits for the assessment and design of rock riprap and to ascertain the scour vulnerability of existing bridges.

The analysis of riprap stability can be considered a fluid structure interaction (FSI) problem. FSI problems involve solving for the fluid flow force on a solid surface, the response of that solid to the load, and subsequently the change of the flow conditions caused by displacement of the solid. Computational fluid dynamics (CFD) software is used for solving fluid flows and computational structural mechanics (CSM) software used is used for solving the deformations and stresses in solid bodies.

Historically, CFD and CSM have developed independently. In recent years, both have been developing additional solvers needed for FSI problems. However, at the moment, there is no integrated software package with both highly robust CSM and CFD solvers needed for general purpose FSI analyses. The current best practice is to couple highly reliable independent CFD and CSM software in an iterative analysis that requires exchange of data on common interfaces between the fluid and solid structures at small time intervals.



Source: Modified by FHWA from NCHRP report 568. See Acknowledgment page. *
Figure 1. Graph. Comparison of riprap sizing curves at a rectangular pier.

The STAR-CCM+ CFD software from the Computational Dynamics-Analysis and Design Application Company (CD-Adapco) is capable of solving flow problems in domains containing solid objects with complex, irregular geometry in relative motion along arbitrary paths through the fluid domain.⁽³⁾ The LS-DYNA CSM software from the Livermore Software Technology Company (LSTC) is a general purpose finite element program capable of simulating highly non-linear real world problems in structural mechanics with changing boundary conditions (such as contact forces between rocks that change over time), large displacements, large deformations, and non-linear material property relations.⁽⁴⁾ These were coupled for this study to analyze the stability of rock riprap under varying geomorphic and hydraulic conditions.

The objectives of this research study were as follows:

- Assess whether detailed FSI modeling can inform evaluation of rock riprap movement for both the analysis of existing riprap aprons and for the design of new riprap aprons.
- Develop recommendations for the design, installation, and monitoring of riprap apron installations at bridge piers and abutments, where feasible.

These objectives were addressed in this project through a combination of physical and numerical modeling. The numerical modeling was then tested and validated on a field case study.

Chapter 2 provides an overview of the literature review conducted to support this project. Chapter 3 describes physical modeling used to validate the numerical modeling.

*Revised 10/17/18

Chapters 4 and 5 summarize the development of the coupled FSI numerical modeling tool and its application to a field case study. Conclusions and recommendations are provided in chapter 6.

Two appendices provide detailed background information for the interested reader: appendix A provides the annotated bibliography developed during the literature search and appendix B provides additional technical information on the development and testing of the coupled FSI numerical modeling tool.

CHAPTER 2. LITERATURE REVIEW

Riprap is one of the most common countermeasures for bridge scour. For abutments, riprap can be used for design of new bridges and for scour remediation at existing bridges. FHWA does not recommended riprap for the design of new piers, but it may be used for scour remediation issues involving piers. Most reports and guidelines focus on design equations for sizing the rock size for the riprap countermeasure. However, sizing the armor is only one component of the comprehensive design, installation, inspection, and maintenance process required for successful pier or abutment scour countermeasures. Riprap countermeasures are integrated with the structural elements they are designed to protect and, therefore, must include consideration of the armor layer thickness, the filter layer, and apron termination details. Successful performance depends on the response of each component of the system to hydraulic and environmental stresses throughout its service life. All of the following are necessary: filter requirements; material and testing specifications; construction and installation guidelines; and inspection and quality control procedures.

The literature review concentrates on available information, data, studies, and guidelines for riprap failure Modes and design recommendations including significant studies completed through the National Cooperative Highway Research Program (NCHRP). Five comprehensive source documents were identified:

- NCHRP Report 568, *Riprap Design Criteria, Recommended Specifications, and Quality Control*.⁽²⁾
- NCHRP Report 593, *Countermeasures to Protect Bridge Piers from Scour*.⁽⁵⁾
- Hydraulic Engineering Circular (HEC) 23, *Bridge Scour and Stream Instability Countermeasures: Experience, Selection, and Design Guidelines*, Third Edition.⁽¹⁾
- Melville and Coleman's reference book, *Bridge Scour*.⁽⁶⁾
- Center for Civil Engineering Research and Codes (CUR), *Manual on the Use of Rock in Hydraulic Engineering*.⁽⁷⁾

Appendix A contains the annotated bibliography developed for this study. Additional sources included bridge scour related papers and abstracts published in the American Society of Civil Engineers (ASCE) Compendium of Papers from ASCE Water Resources Engineering Conferences from 1991 to 1998.⁽⁸⁾ This Compendium contains 371 abstracts and 75 full papers, including a section dedicated to countermeasures.

CHAPTER 3. PHYSICAL MODELING

Physical modeling was conducted at the Turner-Fairbank Highway Research Center (TFHRC) to provide a dataset for validation of the numerical modeling described in chapter 4. TFHRC designed and conducted a laboratory experiment of a vertical-wall abutment that encroaches into the channel at a scale of 1:18 (model:prototype).

TILTING FLUME

A flume with transparent glass side walls and a width, depth, and length of 6 ft, 1.8 ft, and 70 ft (1.83 m, 0.55 m, and 21.35 m), respectively, was used to conduct the experiments. The flume recirculated water and could be tilted to create a variety of flow conditions. A schematic drawing of the flume is presented in figure 2.

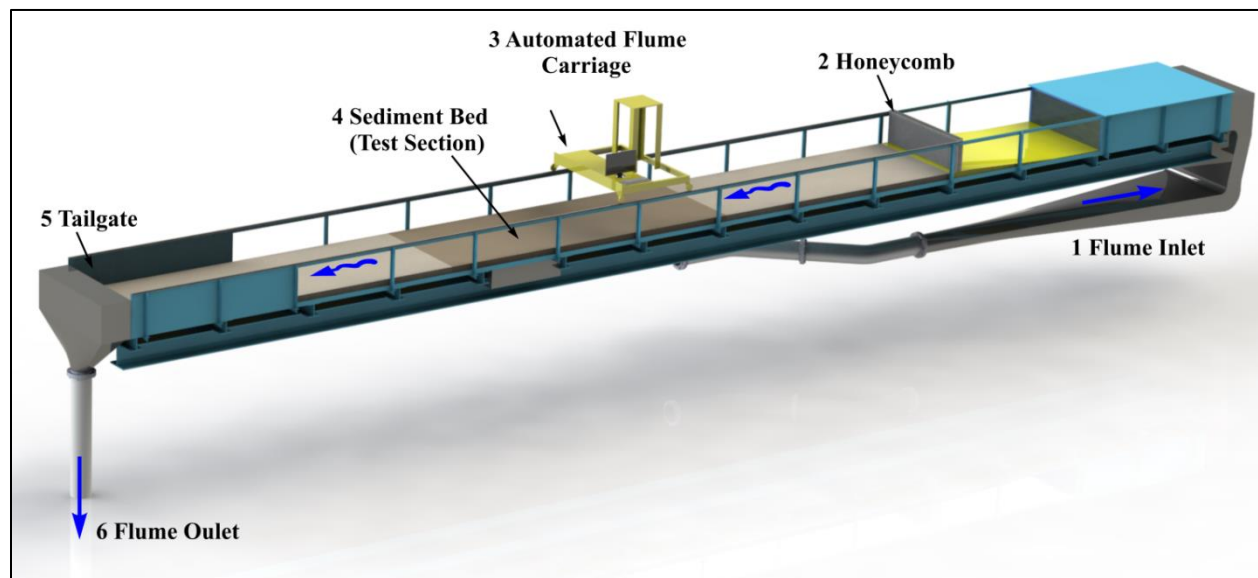


Figure 2. Illustration. FHWA tilting flume.

The flume's skeleton was composed of U-shaped lateral steel frames supported on box-sectioned longitudinal girders. A walkway was provided on one side of the structure. Water was supplied to the flume by a circulation system with a sump of 7400 ft³ (210 m³) and a pump with a maximum capacity of 10.6 ft³/s (0.3 m³/s). The discharge was measured by an electromagnetic flowmeter before the flow was introduced to an upstream head box equipped with a screen and filter. Rapid development of a fully turbulent boundary layer was achieved through an upstream ramp followed by a honeycomb mesh as a flow straightener and an upstream transition zone composed of a layer of coarse sediments carefully placed on the flume bed to provide excess friction. The flow depth was regulated through a computer-operated adjustable tail gate.

Figure 3 shows the flume instrumented with an automated three-axis positioning system with traversing capability for the entire length, width, and height of the flume at a 0.039 inches (1 mm) resolution. This carriage can position probes at any location within the test section to

make point velocity measurements using an Acoustic Doppler Velocimeter (ADV) (shown in figure 4) and to characterize bed surface bathymetry using a laser-distance sensor.

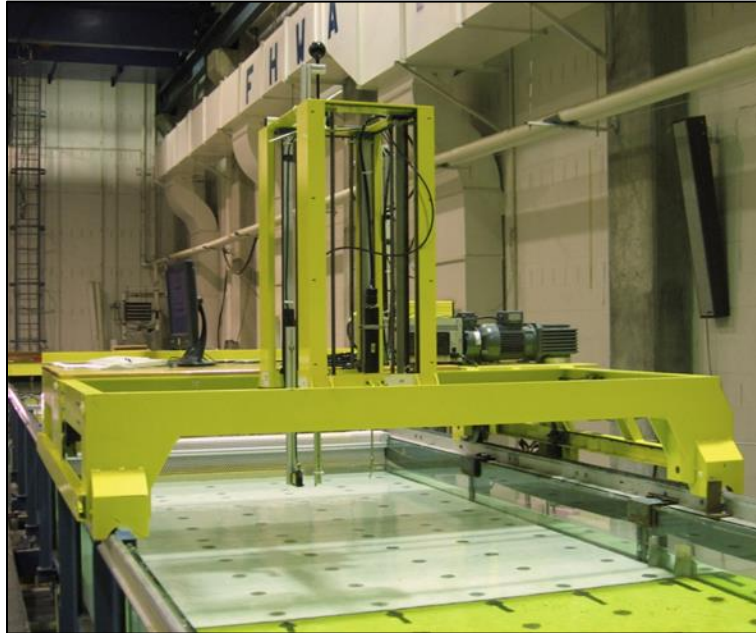


Figure 3. Photo. Automated flume carriage in the TFHRC Hydraulics Laboratory.



Figure 4. Photo. ADV probe.

TEST SECTION

Figure 5 and figure 6 show plan and cross-section views, respectively, of the experimental layout in the test section. The approach channel width (W_1) was 6 ft (1.83 m) and the contracted (bridge opening) width (W_2) was 3.87 ft (1.18 m). Identical geometry vertical-wall abutments with an

abutment length (l_1) of 2.23 ft (0.68 m) and abutment width (l_2) of 1.07 ft (0.325 m) were placed on each side of the flume. The approach velocity (V_1), approach flow depth (y_1), the contracted section velocity (V_2), and the contracted flow depth (y_2) are also shown on the figures. One abutment was constructed of a transparent material to allow recording of rock movement.

A riprap apron was installed flush with the fixed channel bed around both vertical-wall abutments per HEC-23 *Design Guideline* (DG) 14.⁽¹⁾ The average rock layer protrusion exposed to the flow was 10 to 15 percent of the D_{50} . The riprap apron layer thickness (t) was two times the D_{50} of 0.67 inches (17 mm), which was estimated using HEC-23 DG 14. The riprap apron extent (W_R) was two times the flow depth in all directions as recommended by HEC-23 DG 14.

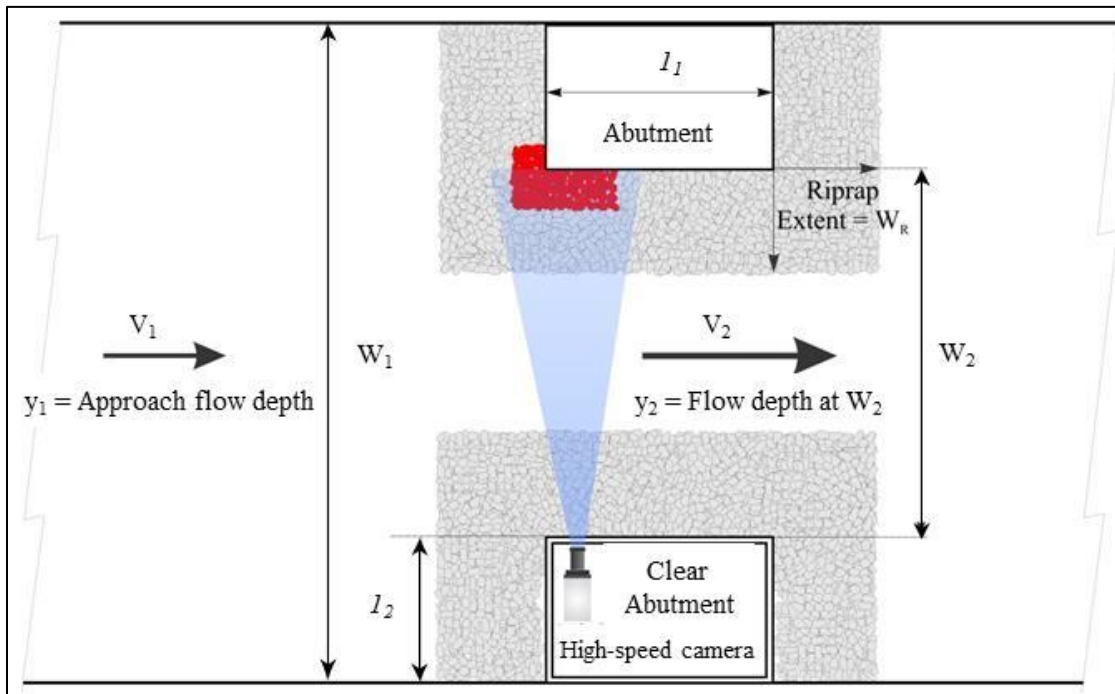


Figure 5. Sketch. Plan view of the test section.

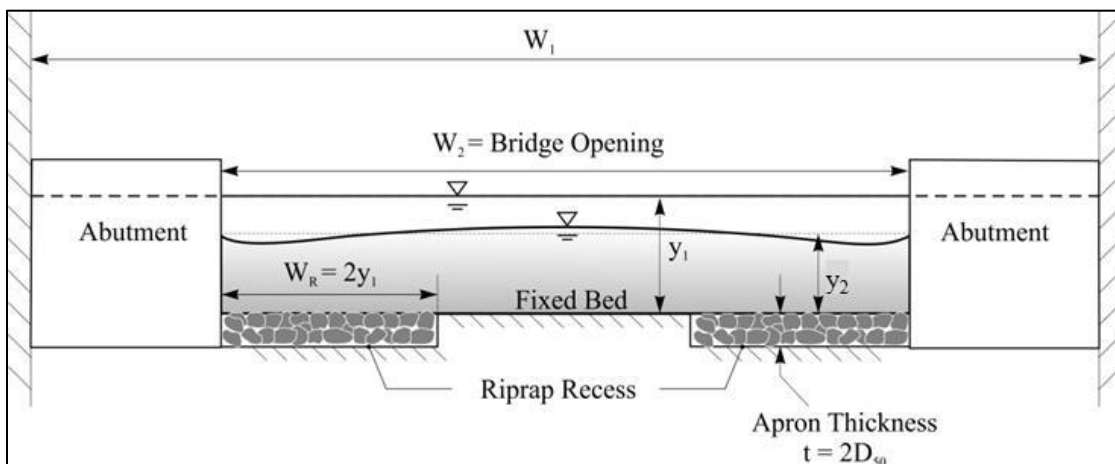


Figure 6. Sketch. Cross-section view of the test section.

In addition, rocks around the upstream corner of **the*** first abutment were colored with a lighter color (blue) for the bottom first layer and a darker color (red) for the top second layer as shown in figure 7. Figure 8 shows the installation before testing. The colored rocks were placed in the potential “failure zone” based on observations and measurements from experiments conducted by Pagán-Ortiz.⁽⁷⁾



A. Bottom layer.

B. Top Layer.

Figure 7. Photos. Riprap installation.



Figure 8. Photo. Riprap apron installation for testing.

EXPERIMENTAL PROCEDURE

The experimental procedure was designed to identify the conditions for incipient motion of the riprap and to assess the nature of the riprap apron after failure.

Riprap Incipient Motion

Incipient motion of individual rocks was monitored and recorded with a high-speed camera that was positioned inside the transparent abutment as shown in figure 5. The recording frame rate

*Revised 10/17/18

varied within the range of 62 to 125 ft/s (18.9 to 38.1 m/s). The velocity was increased stepwise at very small increments. During this process, the approach flow depth remained constant at 0.56 ft (0.17 m) for all runs, although small fluctuations in the flow depth were impossible to avoid as the velocity increased. When incipient motion of the riprap was detected, the approach velocity that caused the shear failure was maintained for a period of 4 h at which time the test was concluded.

Figure 9 shows a failure sequence for one of the runs with the flush apron installation around the abutment that was used for the comparison with the numerical modeling approach that is described in chapter 4. Figure 10 shows another example with the riprap installed at a slope of 1V:2H against the front face of the abutment using the same riprap size and the same upstream flow depth.

Riprap Apron Condition after Failure

A laser distance sensor was used to scan the bathymetry of the riprap apron to characterize the failure zone around the abutment. Figure 11 shows an isometric view of the surface mapping results after shear incipient motion failure of the first layer of rocks at the upstream corner of the abutment.

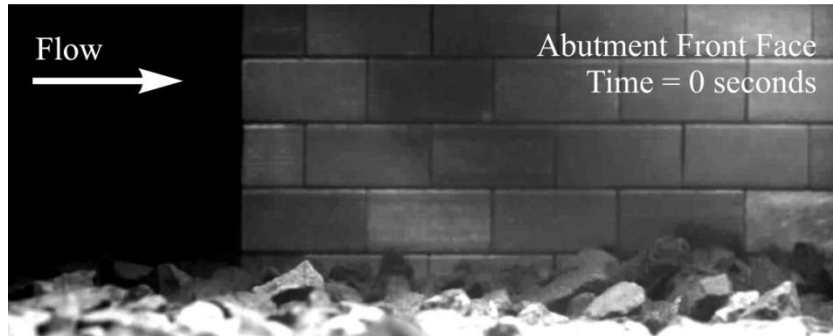
Figure 12 shows the same run with the painted rocks clearly outside the area in which they were placed. The results for all runs confirmed that the rock incipient failure zone was located at the upstream corner of the vertical-wall abutment. The tests also showed that the majority of the entrained rock settled downstream along and near the abutment front face.

The experiments were conducted with a range of approach velocities as summarized in table 1. In all cases the approach flow depth was 0.56 ft (0.17 m). During the experiments, only the upstream average velocities were recorded to avoid any interference with the ADV probe submerged in the contracted (bridge opening) section. The average velocity in the contracted section was estimated using conservation of mass.

As can be seen in table 1, at the lowest velocity, the rocks appeared stable. With increasing velocity, some shaking was observed but no movement. At the three experiments with the highest approach velocities, shear failure was observed.

Table 1. Flow conditions for flume experiments.

Measured Upstream Velocity, ft/s (m/s)	Estimated Average Velocity in Contraction, ft/s (m/s)	Froude Number in the Contraction	High Speed Camera Recordings
0.89 (0.27)	1.71 (0.52)	0.44	Rocks stable
1.18 (0.36)	2.33 (0.71)	0.62	Some rocks shaking, but no entrainment observed
1.25 (0.38)	2.40 (0.73)	0.64	
1.28 (0.39)	2.49 (0.76)	0.66	
1.38 (0.42)	2.66 (0.81)	0.70	Shear failure, rocks moved
1.44 (0.44)	2.82 (0.86)	0.75	



A. Time equals 0 seconds.



B. Time equals 0.5 seconds.



C. Time equals 2.25 seconds.



D. Time equals 7.25 seconds.

Figure 9. Photos. Shear failure sequence for riprap apron installed flush with channel bed.

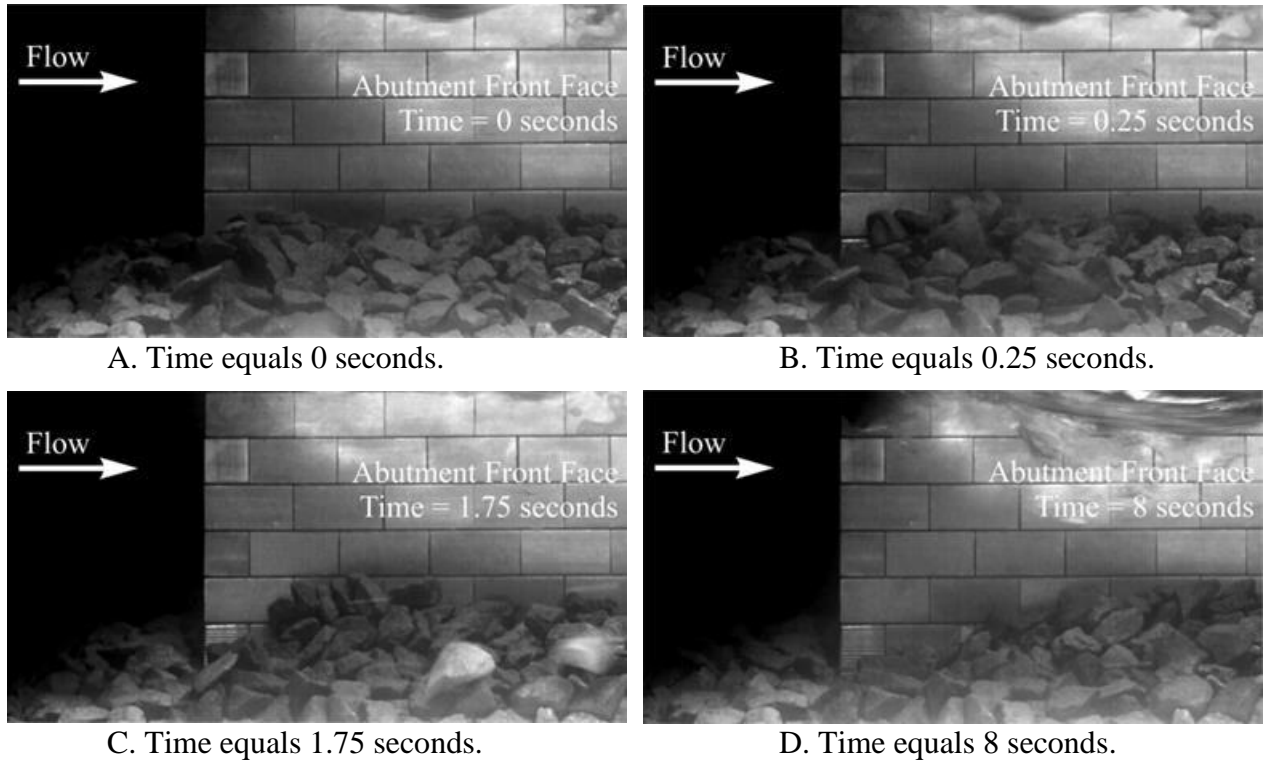


Figure 10. Photos. Shear failure sequence for riprap installed on a slope against the abutment face.

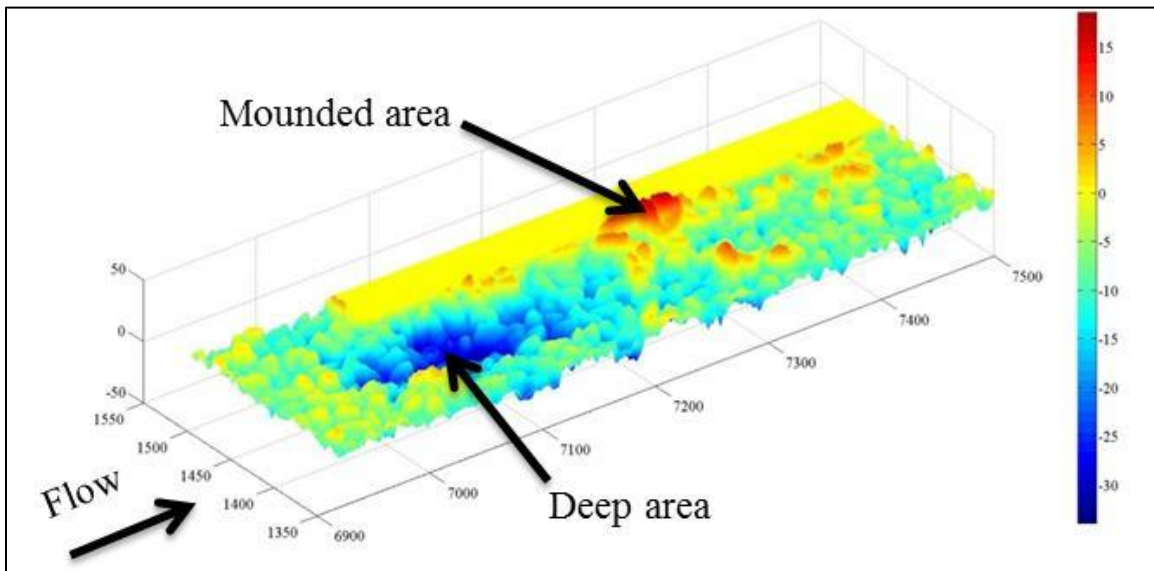


Figure 11. Graphic. Bathymetry of the riprap apron after failure in isometric view.

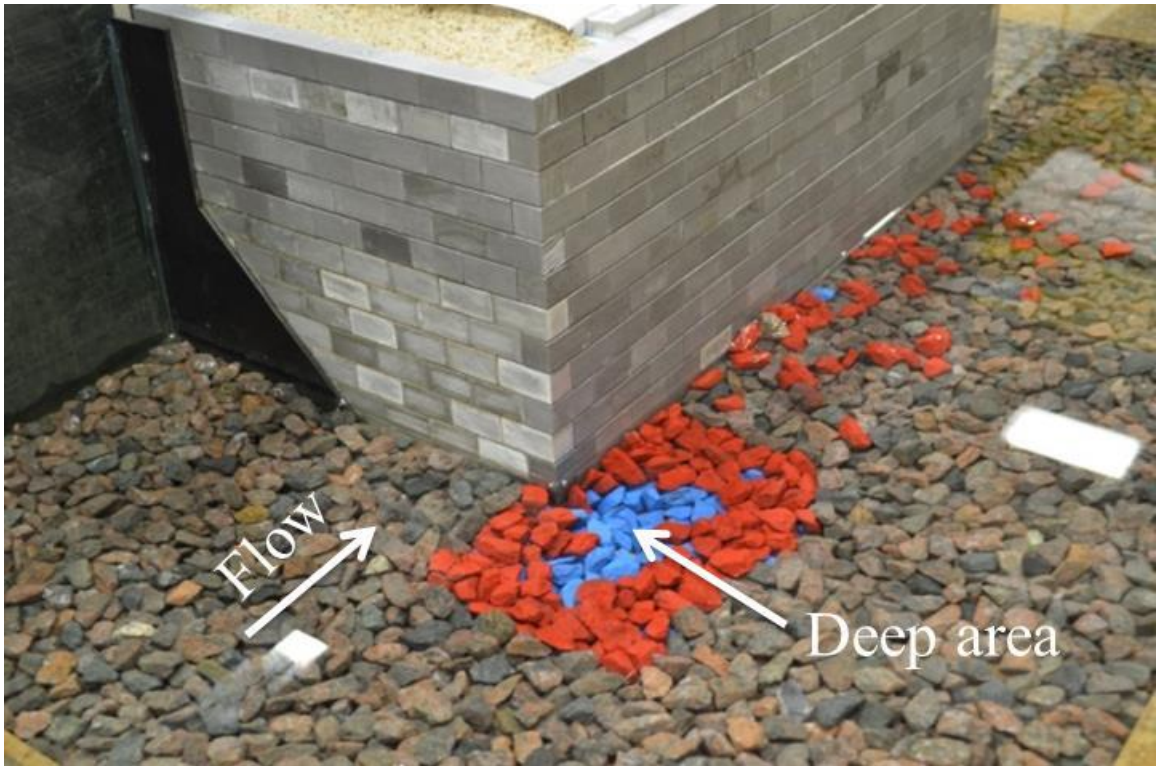


Figure 12. Photo. After rock shear failure at the upstream corner of the abutment.

CHAPTER 4. NUMERICAL MODELING: TOOL DEVELOPMENT

Numerical modeling to evaluate the incipient motion and movement of rock riprap was conducted at the Transportation Research and Analysis Computing Center (TRACC) at Argonne National Laboratory. Most of this chapter describing the development and testing of the modeling tools is taken from Bojanowski et al.⁽¹⁰⁾ The interested reader will find more detail in that reference, and in appendix B.

INTRODUCTION AND OBJECTIVES

From a computational mechanics point of view, the analysis of riprap stability can be considered an FSI problem. FSI problems involve solving for the fluid flow forces on a solid surface, the response of that solid to the load, and subsequently, the change of the flow conditions caused by displacement of the solid. CFD software is used for solving fluid flows and CSM software is used for solving the deformations and stresses in solid bodies.

Historically, these software tools developed independently. In recent years, a number of CFD and CSM software vendors have been developing the capabilities needed to solve FSI problems. In many cases, these vendors are recognized leaders in the field of either CFD or CSM but not both. Integrated FSI software, if available, is not yet mature nor well tested by industry. Until industry-proven FSI solvers are available, coupling highly robust and reliable CFD and CSM software through the development of data exchange and concurrent control coupling procedures appears to be the best approach for solving complex engineering FSI problems.

For this project, FHWA engaged the services of the TRACC for FSI modeling. TRACC has licenses, a user base, and in-house expertise in the use of the software for the STAR-CCM+ CFD software and the LS-DYNA CSM software. For this project, TRACC developed coupling procedures between these software packages to support detailed analysis of riprap stability.

NCHRP report 568 lists four major failure Modes for riprap revetments: (1) slope failure resulting in a slide, (2) riprap particle erosion, (3) erosion beneath the riprap armor layer, and (4) erosion of the toe or key of the revetment leading to a slide.⁽²⁾ The methods described in this chapter can be applied to analyze failure Modes (1), (2), and (4). However, a model capable of describing scour beneath riprap revetment would be required to analyze failure Mode (3).

Modeling rock motion must overcome several challenges. One is sufficient characterization of the complex geometry of the bed in the vicinity of a pier or abutment. A riprap apron may include hundreds of rocks placed in a semi-organized manner in several layers. Representing each rock in the model is currently infeasible. However, sufficient engineering accuracy may be obtained with a reasonable approximation of the armored bed geometry.

A second problem pertains to the extent of the domain to be modeled with CFD for proper representation of flood conditions. The upstream boundary of the computational domain needs to be a sufficient distance away from the zone of interest so that the velocity profile can develop by the time the flow reaches the area of the bridge. Variations in river bed bathymetry constantly perturb the velocity profile. In most cases, placing the upstream boundary at least ten river hydraulic diameters upstream is sufficient. Similarly, the downstream outlet boundary must be

sufficiently removed from flow obstructions so that recirculation zones created by flow obstructions, such as bridge piers, do not cross the outflow boundary. If the downstream boundary is too close to an obstruction, a recirculation zone may pull fluid into the domain through the outlet boundary violating the boundary conditions and the computation normally diverges. The outlet boundary should also be sufficiently removed from the zone of interest. Placing the outflow boundary at least ten river hydraulic diameters downstream of the last obstruction is usually sufficient.

STAR-CCM+ can address both issues because it can accommodate millions of computational cells. However, physically obtaining detailed bathymetry of a river bed is difficult and expensive.

Proper handling of the changes in the geometry within the CFD model is a third issue. STAR-CCM+ is capable of solving flow problems in domains containing solid objects with complex, irregular geometry in relative motion along arbitrary paths through the fluid domain using mesh motion and mesh morphing techniques. These capabilities allow for the deformation of the computational mesh to accommodate moving boundaries. During this process, new cells are not created and the solution is mapped from the old mesh to the new deformed mesh. However, large displacements of rocks as well as collisions between the rocks may cause the stretched cells to lose sufficient cell quality for an accurate solution of the governing equations or the algorithm may collapse cells causing negative volume cell termination of the computation. Automatic interaction between morphing and remeshing of the domain when cell quality becomes too poor is not available in STAR-CCM+. While STAR-CCM+ can model some rigid body interactions with a fluid in motion and has some capability to describe collisions between solid bodies, modeling of collisions is not yet sufficiently robust to describe the onset of motion for rocks.

LS-DYNA software is a general purpose finite element program capable of simulating highly non-linear problems in structural mechanics including changing boundary conditions (such as contact forces between rocks that change over time), large displacements, large deformations, and non-linear material property relations. Recent updates to LS-DYNA included the release of a new CFD solver that is coupled to its structural solver. LS-DYNA includes morphing and automatic remeshing interaction; however, the coupled CFD solver is not capable of handling the large domains required for stream flood modeling. In addition, the meshing capabilities are limited to tetrahedral elements and the physics models in LS-DYNA are limited compared with STAR-CCM+.

These issues with LS-DYNA or STAR-CCM+ lead to the conclusion that it is not practical to solve the FSI problem for onset of riprap motion with either software system by itself. Therefore, the primary objectives of numerical modeling tool development for this project were as follows:

- Develop an efficient and automatic procedure for file-based data exchange between STAR-CCM+ and LS-DYNA for the purpose of FSI modeling of the motion of large riprap rocks in river flow.
- Develop java macros internal to STAR-CCM+ to automatically update the model geometry and mesh based on rock motion data from LS-DYNA.

After development of the tools, they were tested by application to a case study of riprap at a bridge pier in the Middle Fork Feather River described in chapter 5. The following section describes validation of the methodology.

VALIDATION OF THE METHODOLOGY

The coupled FSI modeling tools were validated against the physical modeling described in chapter 3. After validating the numerical modeling tools against the flume modeling data, the results of the physical experiments were scaled up using Reynolds number similarity to evaluate the modeling with full-scale geometry.

Model Geometry

The numerical model geometry was derived from scaling up the experimental flume setup by a factor of 18. Figure 13 shows the plan view of the domain prototype dimensions including the rectangular channel, abutments forming the contracted section, and the riprap aprons intended to protect against local abutment scour. In the numerical analysis, only a half of this symmetrical domain was modeled to reduce the computational burden. Figure 14 shows the domain in a cross-section view.

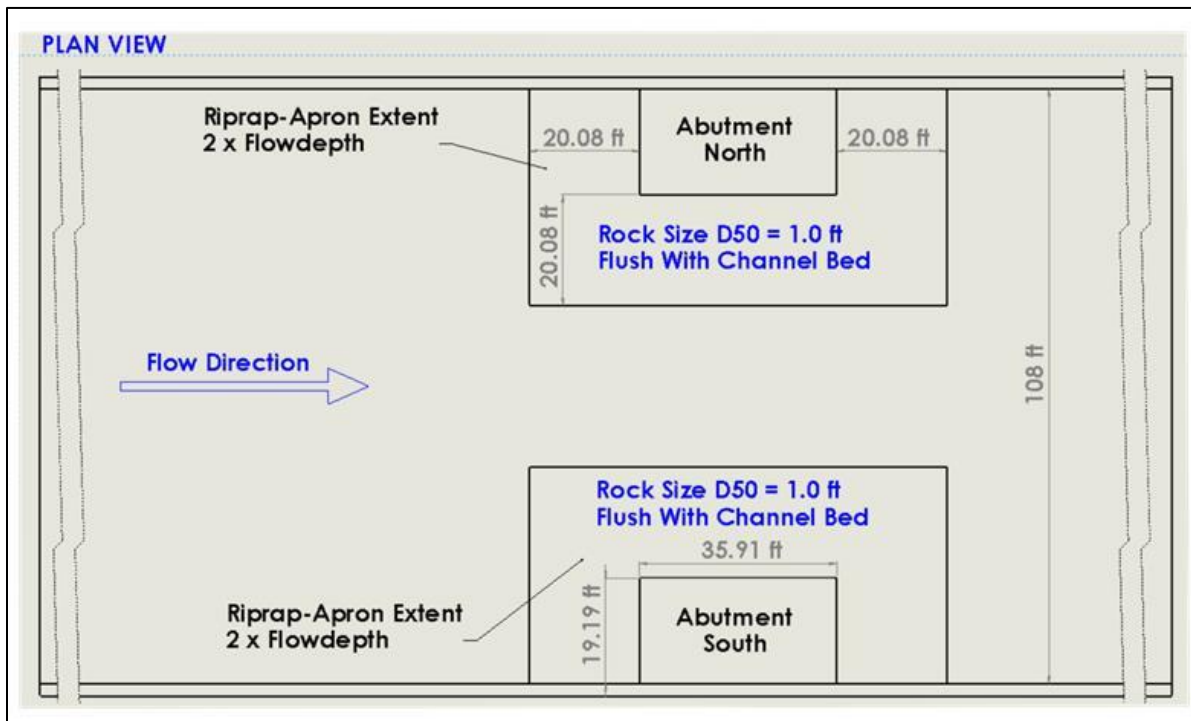


Figure 13. Sketch. Plan view prototype domain.



Figure 14. Sketch. Cross-section view of the prototype domain.

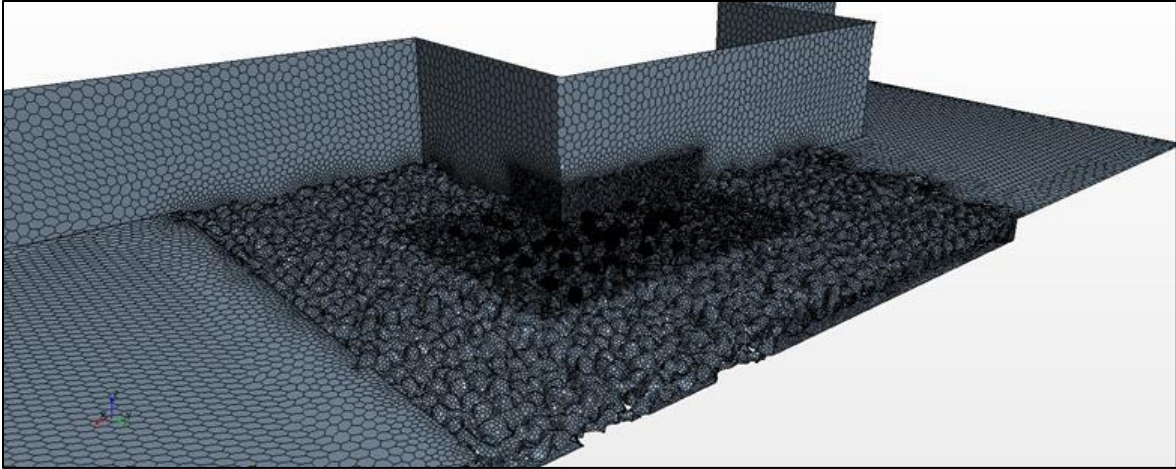
One challenge for the numerical model was to determine the appropriate level of detail for the description of the rocks in the riprap apron, including randomized size, shape, and placement. To address this challenge, a limited number of rocks were allowed to move with the majority being fixed in the modeling. The implementation of the coupling mechanism described in appendix B requires the user to define many settings for each movable rock in STAR-CCM+, as well as in the LS-DYNA model. This process cannot be automated and is very time consuming.

Also, the structural part of the coupling relies on simulation restart capabilities in LS-DYNA that consume a significant amount of computer memory and time. The more movable rocks there are in the model, the longer it takes to restart the LS-DYNA model in each coupling time step. This is one of the limits of the coupling mechanism. These coupling limits, along with the domain remeshing in CFD, are the most time consuming elements of the computation.

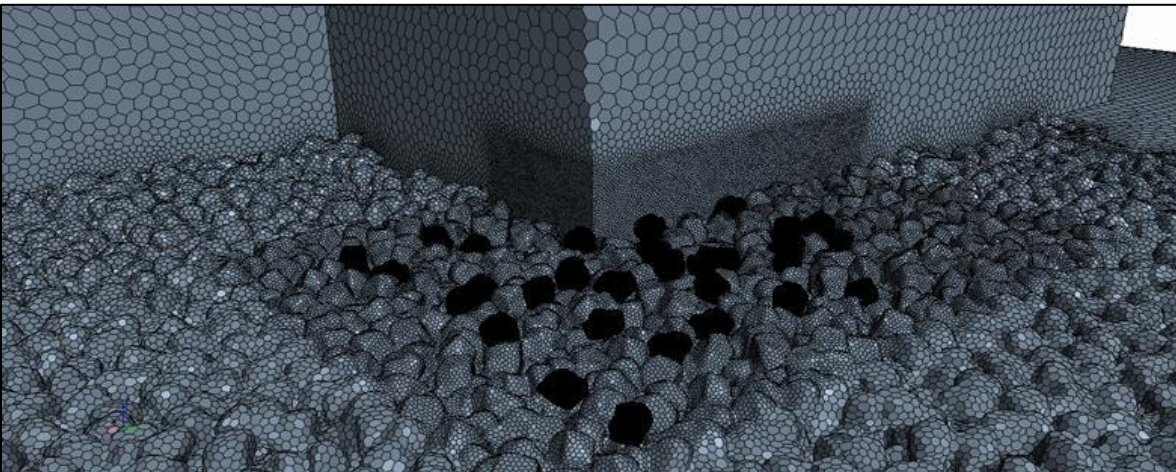
For these reasons, the number of movable rocks was limited to 30. The fine mesh following all feature curves on the rocks were retained only for the movable rocks. The mesh in the CFD model around the movable rocks is very dense but coarsens farther away from them. Approximately 3,000 stationary rocks were manually placed in the testing area. Their packing was not as dense and random as in reality because of computational limitations.

After placing the rocks, the domain was wrapped with the surface wrapper before building the volume mesh. Wrapping the surface closed many small gaps and eliminated problems with intersecting boundaries. The edge size of the largest cells around the rocks distant from the movable ones was around 2.95 inches (75 mm), while the smallest edges sizes near to the movable rocks were less than 0.2 inches (5 mm). The resulting CFD model shown in figure 15 contains 4.4 million polyhedral cells.

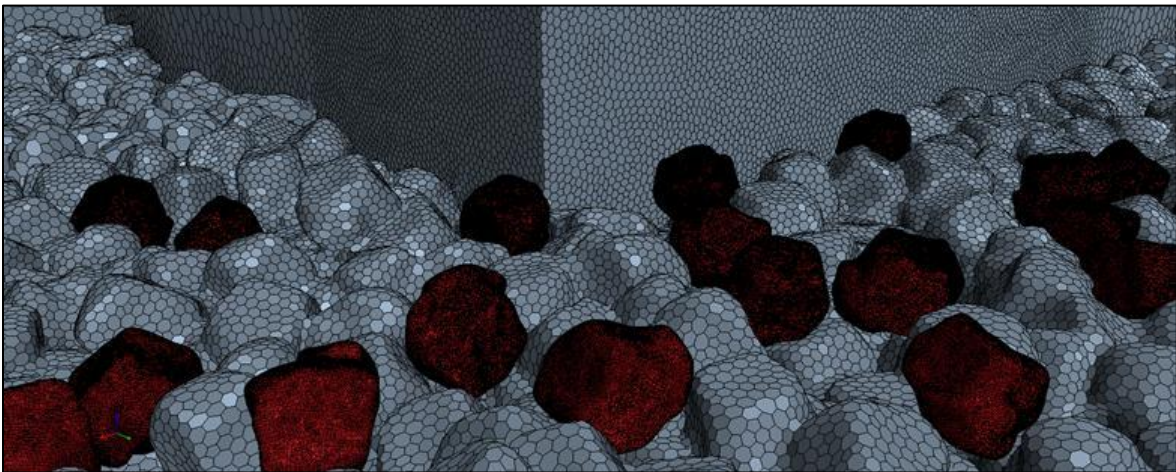
The movable rocks were placed sparsely in the same failure location described for the physical experiments. All 30 movable rocks had the same shape, but their orientation was randomized. The movable rocks are shown in figure 15 as darker in both middle panel and lower panels of the figure.



A. Broad perspective.



B. Medium perspective.

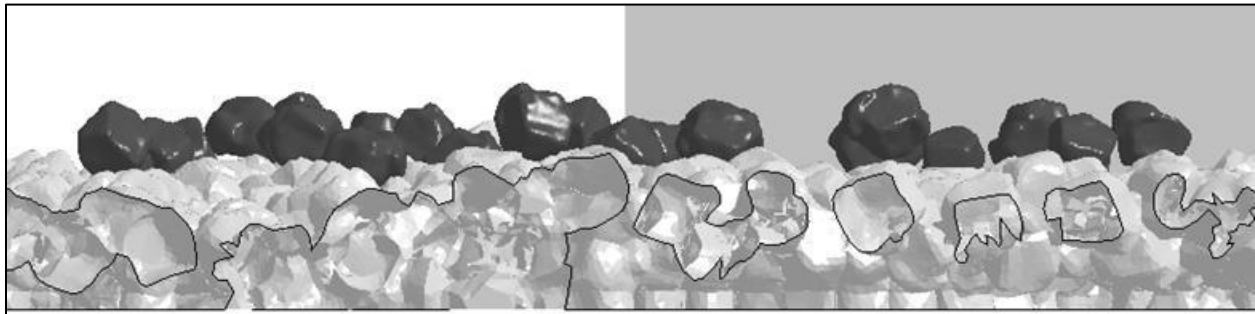


C. Close perspective.

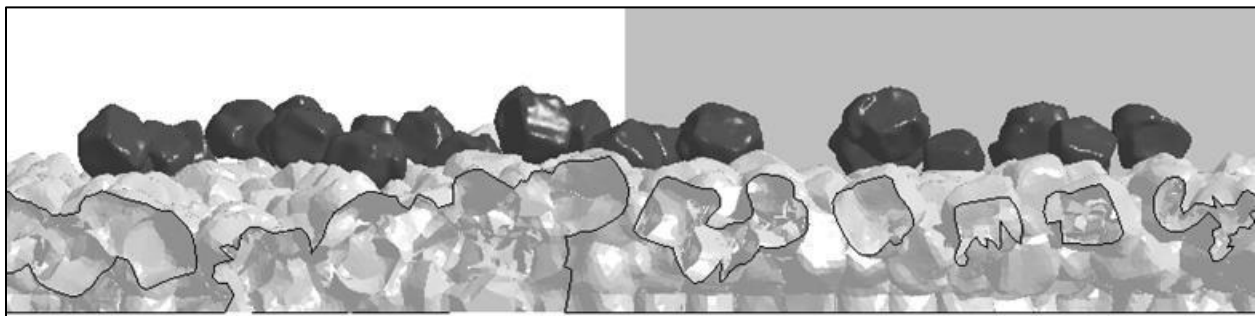
Figure 15. Graphics. Rock layout in the CFD model.

Within LS-DYNA, the placement of the movable rocks could not be performed manually. Equilibrium positions for each rock were determined in a finite element simulation so that they

had proper contact with the ground and would not shift only from the application of gravitational forces. The LS-DYNA model included 1.3 million shell elements and 30 inertia elements attached to the center of gravity of the movable rocks. The stationary bed was constructed from the wrapped surface from STAR-CCM+. Explicit time integration was used with a time step of 4.50E-06 s. The rock drop simulation was run for 10 s of real time. That procedure took approximately 7 h on 64 cores of the TRACC Zephyr cluster. The initial positions of movable rocks as well as their final equilibrium positions are shown in figure 16.



A. Pre-drop.



B. Final.

Figure 16. Graphics. Positions of movable rocks.

The surfaces describing the final position of the movable rocks were extracted from LS-DYNA and imported to the STAR-CCM+ model. The shell elements used for movable rocks in LS-DYNA represent a zero thickness surface, but actually have a thickness of 0.039 inches (1 mm). The contact definition in LS-DYNA does not allow for penetrations of the movable rocks into the bed, which results in at least a 0.039 inch (1 mm) gap between the rocks and the bed in STAR-CCM+ model. This definition is required to prevent computational instabilities resulting from squeezing the computational cells to zero thickness in the case of contacts or collisions between movable rocks and the bed.

Flow Conditions

The force resulting from gravity is important for modelling rivers and other fluids with free surfaces. Therefore, the major governing non-dimensional parameter for model/prototype scaling is the Froude number. Flow conditions in the prototype-scale CFD simulations were calculated based on the Froude similarity with the experimental conditions. The approach flow depth was 10.0 ft (3.06 m) and the D_{50} was 12 inches (306 mm). The prototype range of velocities from the physical experiments described in chapter 3 ranged from 3.76 to 6.11 ft/s (1.145 to 1.87 m/s).

The CFD analyses were performed on a subset of these inlet velocities—3.76, 4.27, 4.59, 4.92, 5.25, and 5.58 ft/s (1.145, 1.3, 1.4, 1.5, 1.6, and 1.7 m/s)—to create initial states for the FSI analyses. This subset was needed to identify the conditions of initial rock motion in the FSI analyses. The inlet velocity was assumed constant across the inlet boundary.

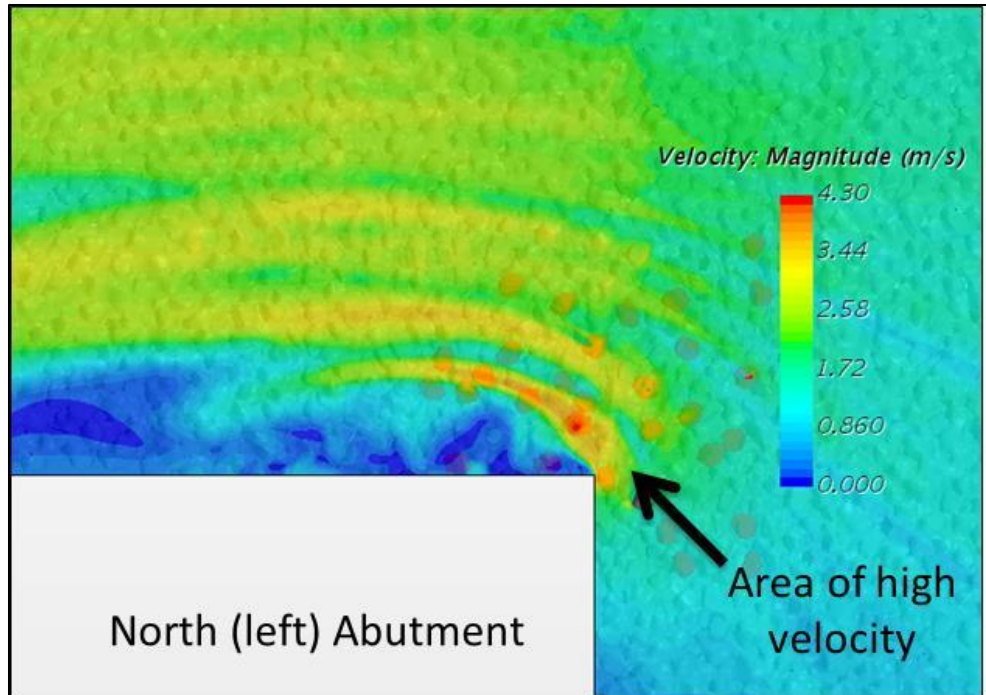
To simplify the analyses, the two-phase nature of open channel flow (water and air) was disregarded and only the water phase was simulated using a “closed-lid” representation. The closed-lid approach was chosen over the more realistic two-phase volume of fluid (VOF) approach because it is significantly less computationally intensive and more robust. The closed-lid assumption forces a constant water height in the model and uses a symmetry boundary condition at the water surface. The disadvantage of the closed-lid approach is that in reality the water level would drop slightly in the contraction zone and rise upstream of the contraction. Therefore, the numerical modeling with a closed-lid would indicate a smaller contraction flow area in the upstream portion of the contraction and upstream of the contraction than would be observed in the physical experiments. In this part of the domain, the closed-lid approach was considered to be conservative because the average velocity in the numerical model would be higher than in the physical model, causing rocks to be set in motion at a slightly, lower-approach water velocity. Once the lower contraction depth is fully established, the closed-lid approach would result in an over-estimate of velocity and not provide a conservative estimate. These differences were assumed to be minor.

A time step of 0.025 s was used in the unsteady Reynolds-Averaged Navier-Stokes (RANS) solver for the CFD and the FSI modeling. The standard k-epsilon turbulence model was used in the analyses.

Model Results

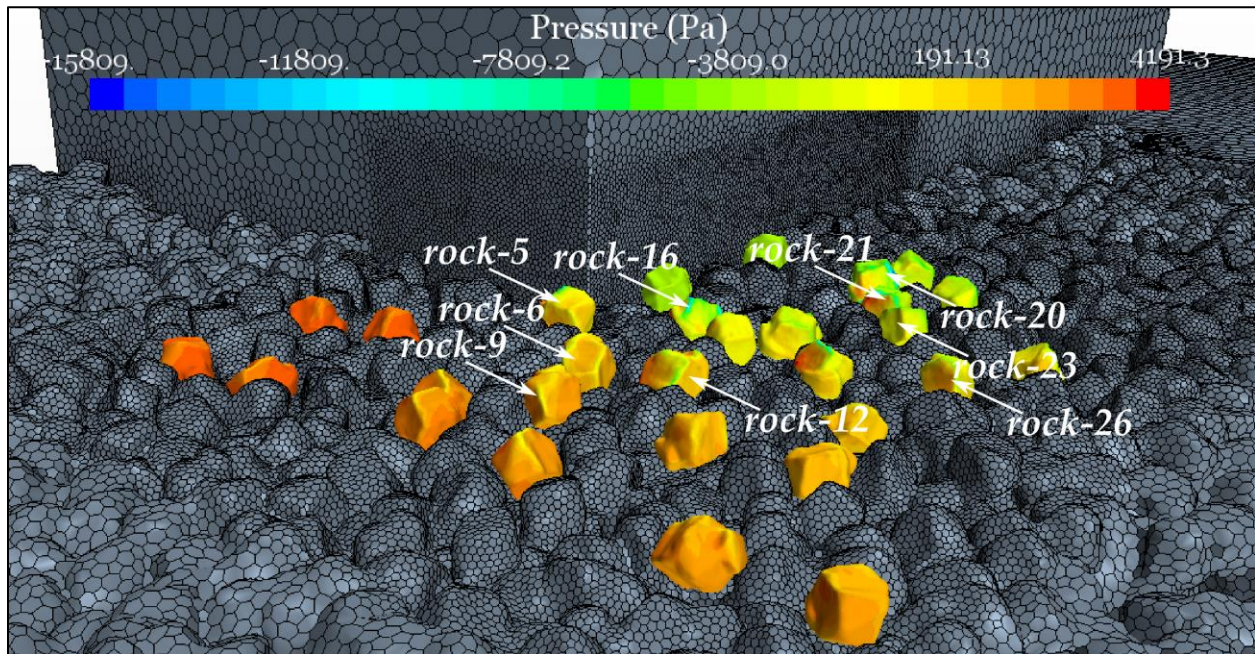
The CFD analysis with an inlet velocity of 4.27 ft/s (1.3 m/s) was identified as the threshold velocity for which failure of riprap was detected. Figure 17 shows a velocity distribution just above the riprap rocks from that simulation. Although the average velocity in the contraction zone is approximately 8.2 ft/s (2.5 m/s), the local water velocity can be as high as 14.1 ft/s (4.3 m/s) near the corner of the abutment.

Figure 18 shows a perspective view of the abutment at the end of the CFD simulation. The pressure was overlaid on the surface of the movable rocks. The ten rocks experiencing the highest pressures are identified in the figure. All are located by the inlet to the contraction zone where the flow acceleration occurs. Both pressure and shear forces were included in the analysis, however, the pressure components are significantly higher than shear by two to three orders of magnitude.



1 ft/s = 0.305 m/s

Figure 17. Graphic. Velocity profile in a horizontal slice just above the riprap rocks with an inlet velocity of 4.27 ft/s (1.3 m/s).

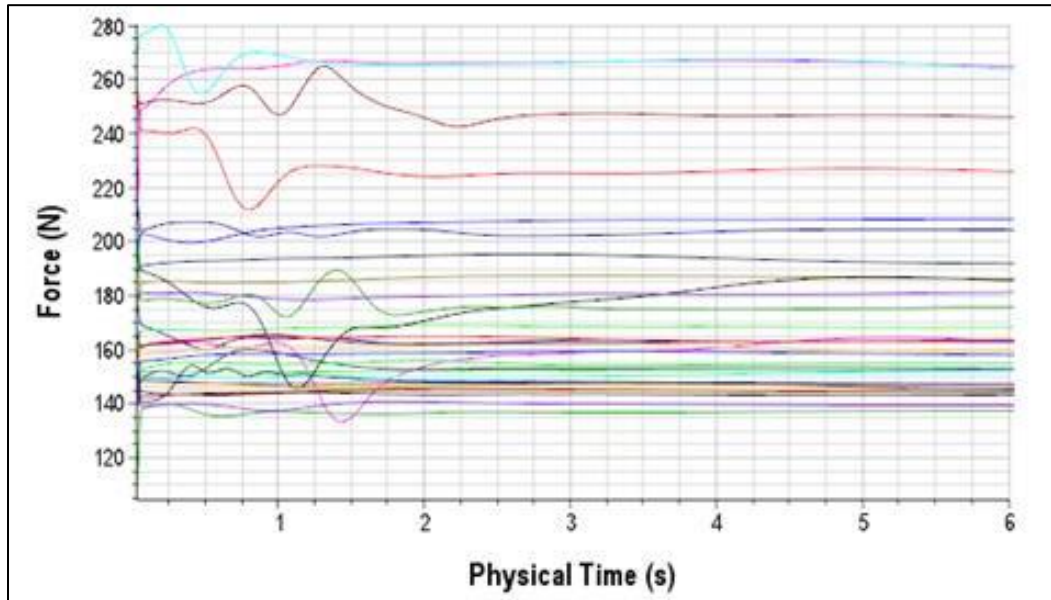


1 lbf/ft² = 47.88 Pa

Figure 18. Graphic. Location of the rocks with the highest forces in a CFD analysis.

Figure 19 shows a representative example of force time histories in the Z-direction (vertical) for several individual rocks with an inlet velocity of 4.27 ft/s (1.3 m/s). Analogous force time

histories were also available for the X-direction (flow direction). Forces in the Y-direction were not reported as they are significantly smaller than forces in the X- and Z-directions. As can be seen in figure 19, the forces were initially unstable but stabilized within approximately 5 s of simulated time.



1 lbf = 4.45 N

Figure 19. Graph. Initial stabilization of vertical forces on movable rocks.

To ensure consistency between the time series of the CFD and CSM analyses, the CFD runs were terminated at 5 s after the instabilities were resolved and the CFD time step was reset to zero retaining all state variables at the stabilized condition. This termination allowed a consistent specification of time equal zero between the two modeling components. The retained state variables from CFD were then imported to the CSM for time equals zero. In this way, both the CFD and CSM analyses were initialized consistently for the FSI analyses.

The primary forces acting on each individual rock are the drag, net weight (weight minus buoyancy), and contact forces. Net weight acts in the vertical direction. However, the direction of the drag force depends on the surrounding flow field; the direction of the contact forces depends on the orientation of neighboring rocks and the locations of their points of contact. Table 2 summarizes the X and Z forces at the end of the simulation, as well as the total resultant force, on the ten identified rocks. The rocks closest to the leading corner of the abutment (5 and 16) experienced the highest forces. Figure 20 illustrates the definition of the coordinate directions and the resultant force on an individual rock.

Movement of an individual rock will depend on the resultant force (including its direction), the weight of the rock (354 N), and the positioning of the movable rock with respect to the other rocks. The Z component of the force is larger than the X component in all cases. The Z component results from the weight and buoyancy as well as from the drag from significant flow in the voids between the stationary rocks. Recall that the packing density of the rocks results in greater void volumes than occurs in the physical experiments. In addition, the rocks away from

the movable rocks are smoothed because of the larger cell sizes. Therefore, the Z forces are likely overestimated, which represents a conservative simplification of the model.

Table 2. Forces on ten movable rocks with varying inlet velocities.

Rock No.	Inlet Velocity 4.27 ft/s (1.3 m/s)			Inlet Velocity 4.59 ft/s (1.4 m/s)	Inlet Velocity 4.92 ft/s (1.5 m/s)
	Z Force (N)	X Force (N)	Resultant (N)	Resultant (N)	Resultant (N)
16	262	145	299	330	370
5	264	122	291	319	352
21	246	86	261	282	306
15	225	46	230	257	279
6	208	36	211	222	237
23	204	45	208	221	237
26	181	95	204	220	234
20	185	78	200	210	236
12	186	59	195	205	217
9	191	37	194	202	220

1 lbf = 4.45 N

By accounting for the collisions and contacts between all rocks, the FSI modeling determines rock movements. The FSI simulations were performed with a coupling time step of 0.025 s, which was also the time step in the CFD modeling. The time step in LS-DYNA of 4.50E-06 s was significantly smaller to account for the collisions and contacts between the movable and stationary rocks. For each time step in STAR-CCM+, there were approximately 5,550 time steps in LS-DYNA. Ideally, these steps should be either equal to or inner iterations within one time step to achieve better accuracy. However, if 5 inner iterations within a time step are needed, then the overall computation time increases 5 times. For these validation studies, each simulation took approximately one week of computation time. This time is a reasonable duration for production runs. The assumed approach is believed to be a good compromise between the accuracy, efficiency, and the conservatism of the results.

Figure 21 shows several snapshots from the FSI simulation for the case with an inlet velocity of 4.27 ft/s (1.3 m/s). Three rocks with the highest forces on them are labeled. Rock 5 is positioned near the abutment corner and it is not moving in the FSI simulation at all. The other rocks experience a sudden push when they are “allowed” to move at the beginning of the FSI simulations. That causes them to oscillate, but they eventually return to their initial positions adjusted for the hydrodynamic forces introduced in the FSI.

Forces on the same ten movable rocks at inlet velocities of 4.59 ft/s (1.4 m/s) and 4.92 ft/s (1.5 m/s) at the end of the stationary CFD simulation are also summarized in table 2. For the inlet velocity of 4.59 ft/s (1.4 m/s), the order of forces is the same as for the lower velocity, but increase between 3 and 10 percent. At this velocity in the FSI analysis, more rocks leave their initial positions. Figure 22 shows several snapshots from the FSI simulation for that case. Rocks 9, 15, 16 and 23 exhibited the most noticeable movement. Several other rocks in the vicinity

oscillated in position. Collisions of the rolling rocks with surrounding rocks triggered local motion of several more rocks. This inlet velocity was considered to be the threshold between stable and failing riprap.

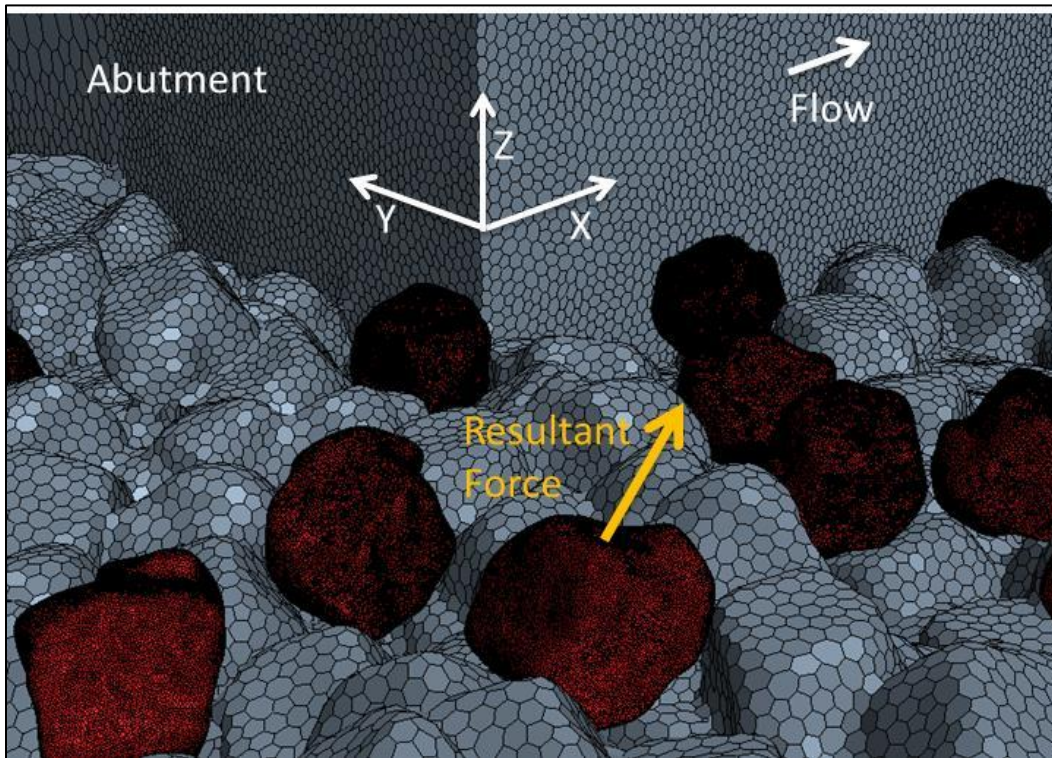
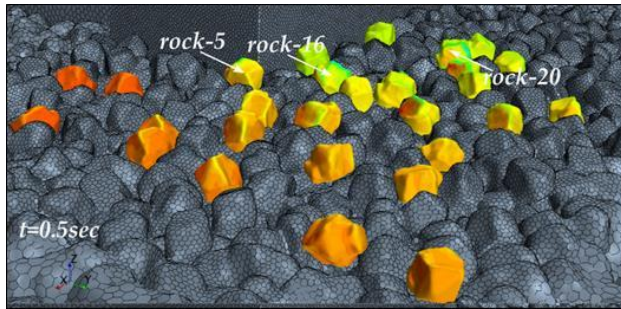


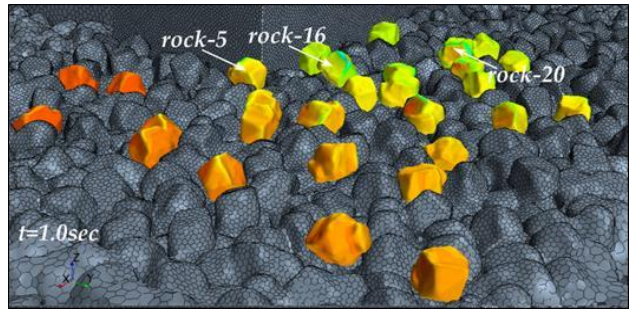
Figure 20. Graphic. Definition of forces on a single rock.

In the case with an inlet velocity of 4.92 ft/s (1.5 m/s) riprap failure became more apparent. The resultant forces increased approximately 10 percent over the previous inlet velocity condition. Figure 23 shows snapshots from that simulation. The rocks with most noticeable motions (9, 15, 16, 18, 23, 26) are labeled in this figure. In addition, rocks 6, 12, 18, and 20 become quite unstable and move locally.

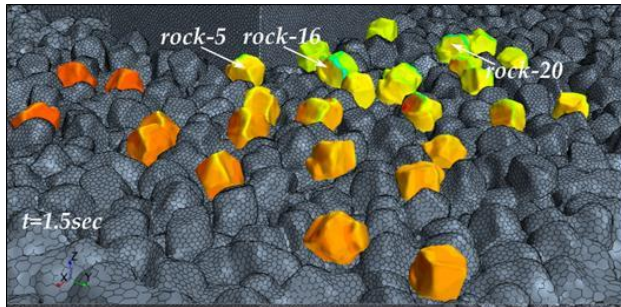
Table 3 compares scaled results from the experiments with the results from the simulations. Scaling up the physical experiments to the prototype scale, the physical experiments validated that the riprap should be stable at an inlet velocity of 3.76 ft/s (1.145 m/s). Similarly, in the CFD simulation at this inlet velocity the rocks do not move from their initial positions. In the physical experiments, the threshold of rock displacement occurred at approximately 5.41 ft/s (1.65 m/s). In the numerical simulations, the threshold was judged to be at approximately 4.27 ft/s (1.3 m/s), approximately 21 percent lower. These results suggest that the numerical simulations are conservative, but are a reasonable representation of the physical behavior. It is hypothesized that the differences between the physical experiments and numerical simulations can be further decreased by more detailed mapping of the stationary rocks in the numerical simulations.



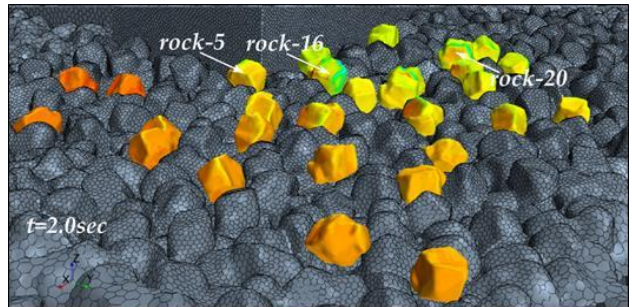
A. 0.5 seconds.



B. 1.0 seconds.

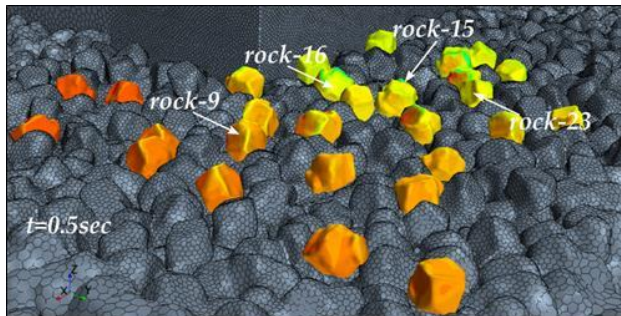


C. 1.5 seconds.

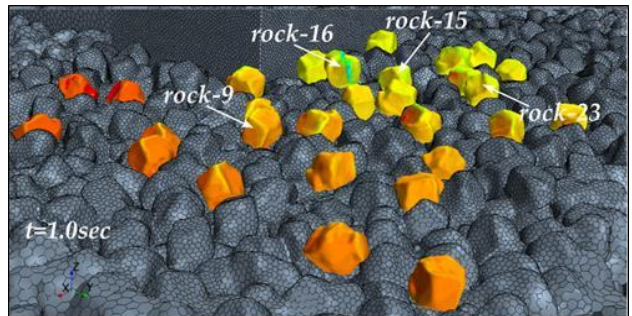


D. 2.0 seconds.

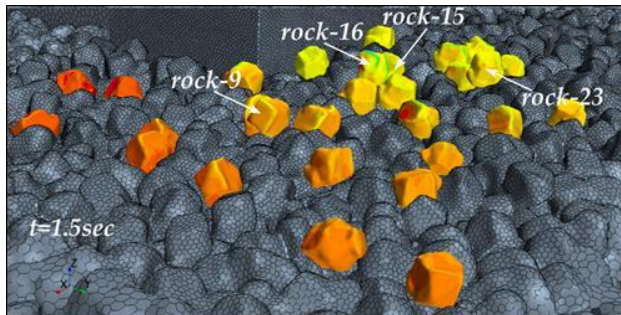
Figure 21. Graphics. FSI simulation for an inlet velocity of 4.27 ft/s (1.3 m/s).



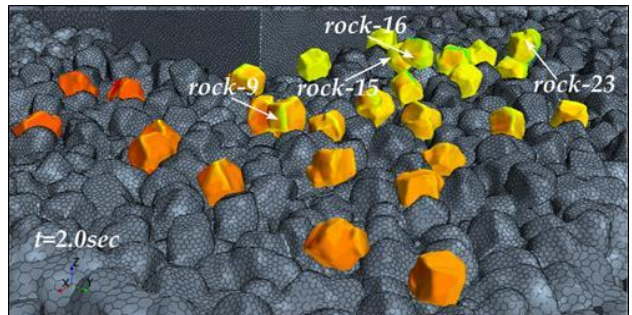
A. 0.5 seconds.



B. 1.0 seconds.



C. 1.5 seconds.



D. 2.0 seconds.

Figure 22. Graphics. FSI simulation for an inlet velocity of 4.59 ft/s (1.4 m/s).

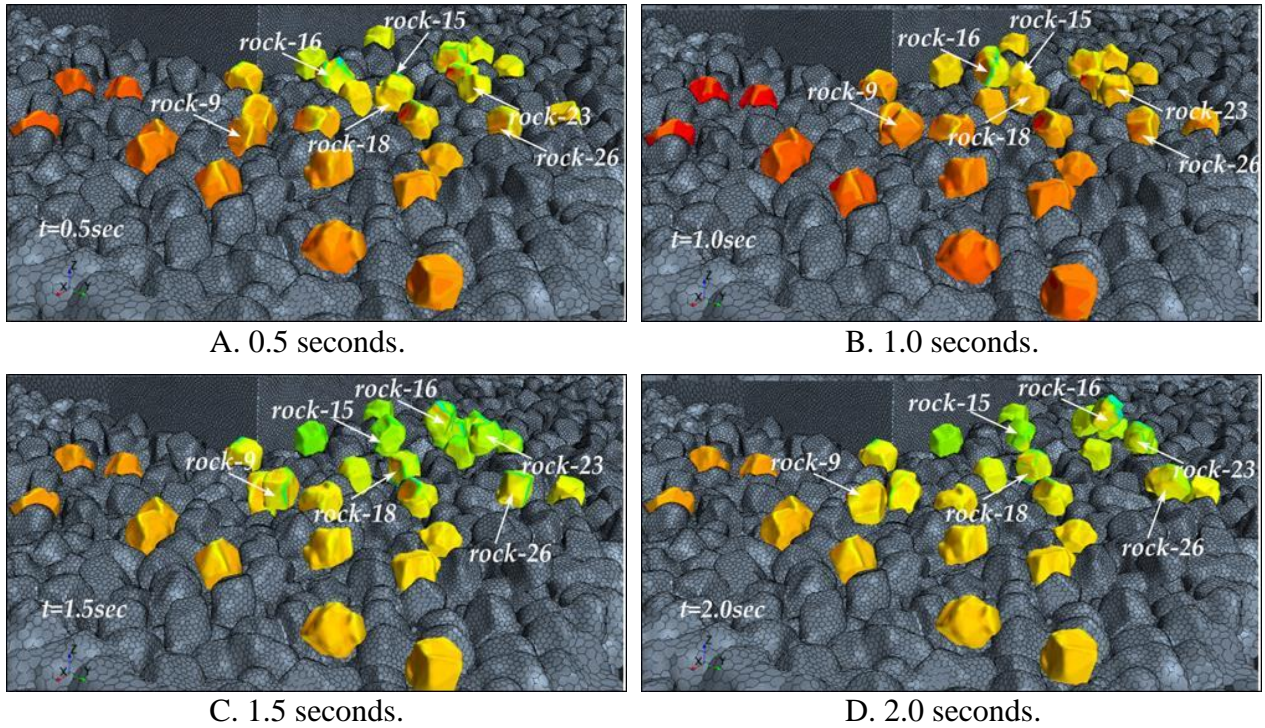


Figure 23. Graphics. FSI simulation for an inlet velocity of 4.92 ft/s (1.5 m/s).

Table 3. Comparison of physical experiments and computational simulations.

Physical Experiments Scaled to Prototype		CFD/FSI Prototype Simulations	
Upstream Velocity, ft/s (m/s)	Observation from Physical Experiment	Upstream Velocity, ft/s (m/s)	Observation from Simulation
3.76 (1.145)	Rocks stable, design velocity	3.76 (1.145)	Rocks stable
5.41 (1.65)	Upper limit where some rocks shaking, but no entrainment	4.27 (1.3)	Potential instability of riprap
5.84 (1.78)	Shear failure, rocks moved	4.27 (1.3)	Potential riprap failure
6.11 (1.87)		4.59 (1.4)	

CHAPTER 5. NUMERICAL MODELING: CASE STUDY

The numerical modeling approach described in chapter 4 was applied to a complex field case study to evaluate the potential for such a tool to evaluate and to design riprap protection for bridge piers and abutments. Current design methodologies and scour evaluation procedures are often based on laboratory studies or straight forward field situations. This case study will illustrate the potential for use of advanced computational mechanics techniques to assess rock stability and bridge vulnerability.

SITE CONDITIONS AND RIPRAP RISK ASSESSMENT

The case study represents an opportunity to study the effectiveness of riprap installed to protect a bridge pier in Plumas County, California. The bridge carries State Route 89 over the Middle Fork of the Feather River near the towns of Blairsden and Graeagle. The bridge was built in 1955 and the river channel was realigned at the time to straighten the flow upstream of the bridge as shown in figure 24.

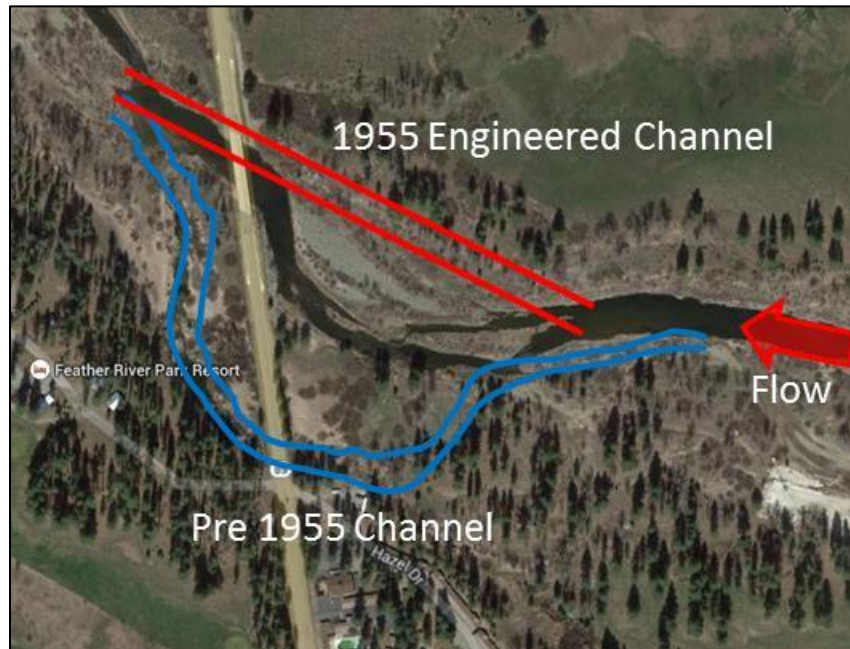
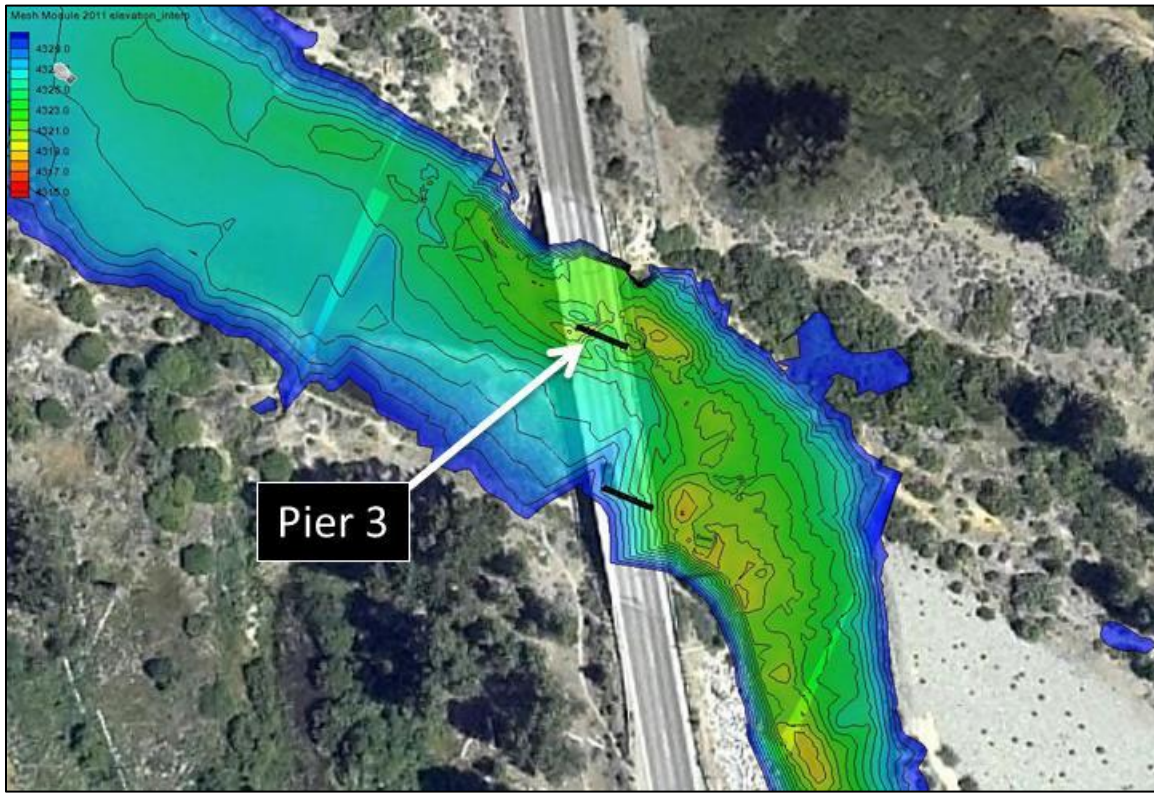


Figure 24. Photo. Historic, realigned, and current channel alignment.

During high winter flows in 1988, the river avulsed from its 1955 realignment and moved toward its historic streambed and flow path. As a result, the flow approaches the bridge at the sharp angle shown in figure 24, causing excessive backwater and deep scour at one of the piers.

Later, the California Department of Transportation (Caltrans) determined that the bridge was scour critical based on vertical contraction scour and local pier scour. In 2011, a field survey was conducted at the bridge site. The survey included acquisition of river bathymetry from a boat and Global Positioning System (GPS) coordinates of ground features near the bridge. The bathymetric survey was conducted using a SonarMite depth finder by Seafloor Systems. Figure

25 shows the riverbed elevation model built based on that data with the deepest scour in front of the pier of primary concern: pier 3.



1 ft = 0.305 m

Figure 25. Photo. River bathymetry before installation of the riprap.

In August 2012, Caltrans placed rock riprap over filter fabric around the most vulnerable pier to protect the bridge. A 1-ton average rock size was specified for this work. Figure 26 shows the extent of the riprap apron design around pier 3. Figure 27 shows the work area near pier 3 during the riprap installation.

In 2013, Caltrans performed a follow-up riverbed survey. Reconstructed bathymetry based on this survey is shown in figure 28. The scour hole was completely leveled with the surrounding bed. However, subsequent investigation of the project site suggested that the riprap design velocities were underestimated and, therefore, the riprap may be under sized to withstand the 100-year design event.⁽¹¹⁾ This concern led to further analysis using the advanced numerical modeling developed for this research project and described in the following section.

MODEL DEVELOPMENT FOR THE MIDDLE FORK FEATHER RIVER

The numerical modeling techniques for FSI analyses described in chapter 4 were applied to the Middle Fork of the Feather River. The following sections describe the development of the CFD and CSM models.

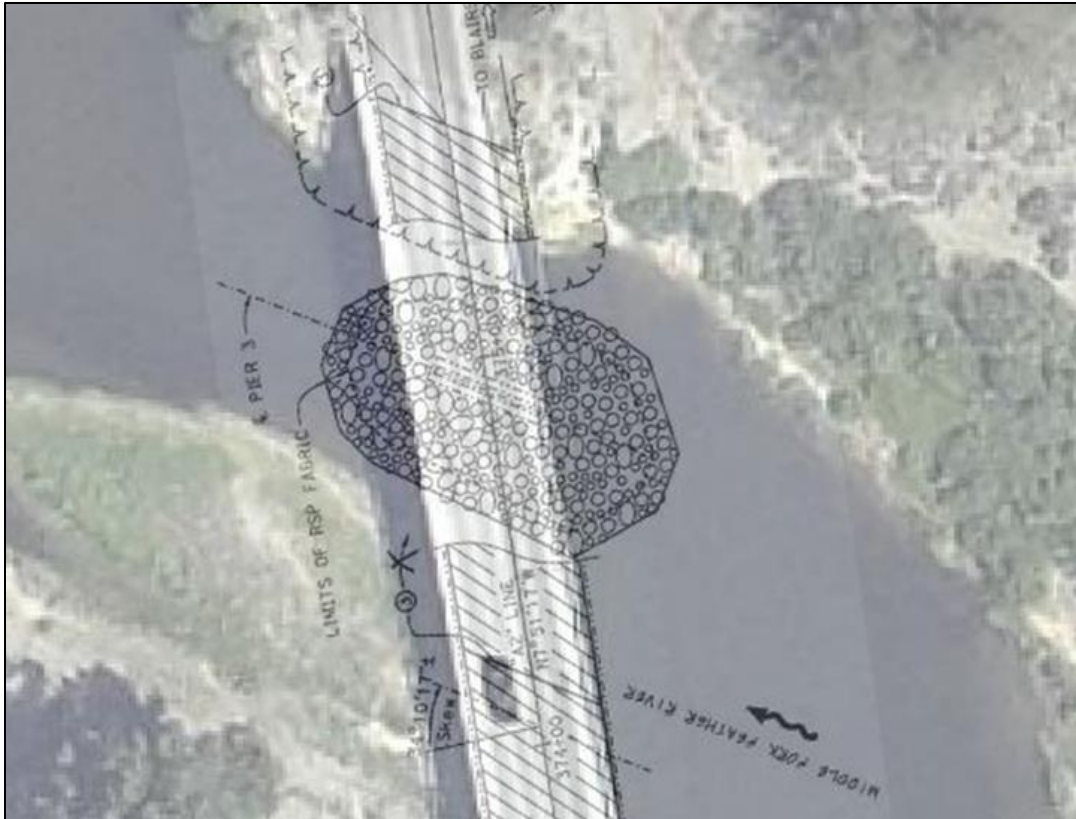


Figure 26. Photo. Rock layout design for protection of pier 3.



Figure 27. Photo. Riprap installation near pier 3 (August 2012).

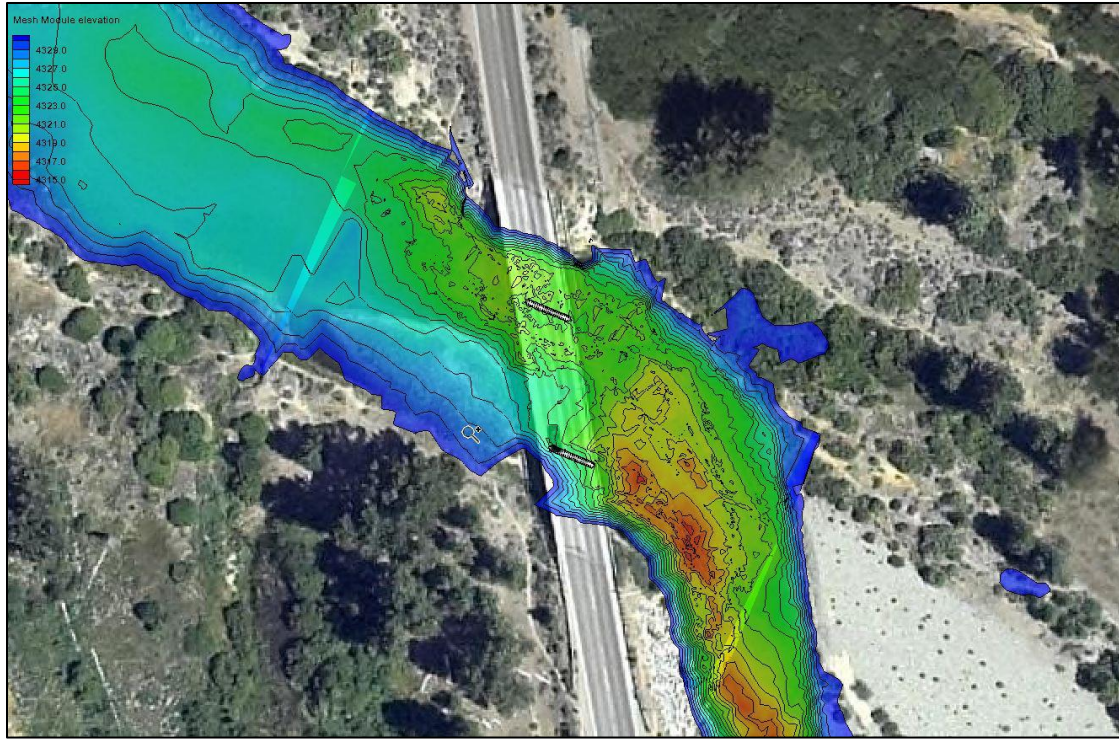


Figure 28. Photo. River bathymetry in 2013 after riprap installation.

Domain and Mesh

The riverbed geometry model was constructed based on the 2011 bathymetric survey and GPS coordinates of the areas around the river. The bed surface in the CFD model was subdivided into river bed and grass surfaces with appropriate roughness coefficients for these boundaries as shown in figure 29. In addition, an area surrounding the pier was bounded with a box where a denser mesh could be used for more accurate results.

The point cloud bathymetry was numerically enhanced using Matlab and MeshLab.^(12,13) The enhanced point cloud was triangulated to obtain a raw surface and imported into STAR-CCM+ as the initial geometry for the numerical model. Next, the bed geometry and the bridge geometry were transformed into a surface mesh. A volume mesh was generated with polyhedral cells. The covered domain was approximately 935 ft (285 m) long, 394 ft (120 m) wide, and 23 ft (7 m) high. As shown in figure 30, the model included pressure, velocity, and symmetry boundary types.

With this domain, large recirculation zones developed near the outlet creating problems enforcing pressure boundary conditions on the outlet. To remedy this situation, the domain was extended downstream another 984 ft (300 m). In the absence of detailed profile data for the river in that region, the extension was based on the most downstream cross-section of the surveyed domain and a longitudinal slope of 0.3 percent.

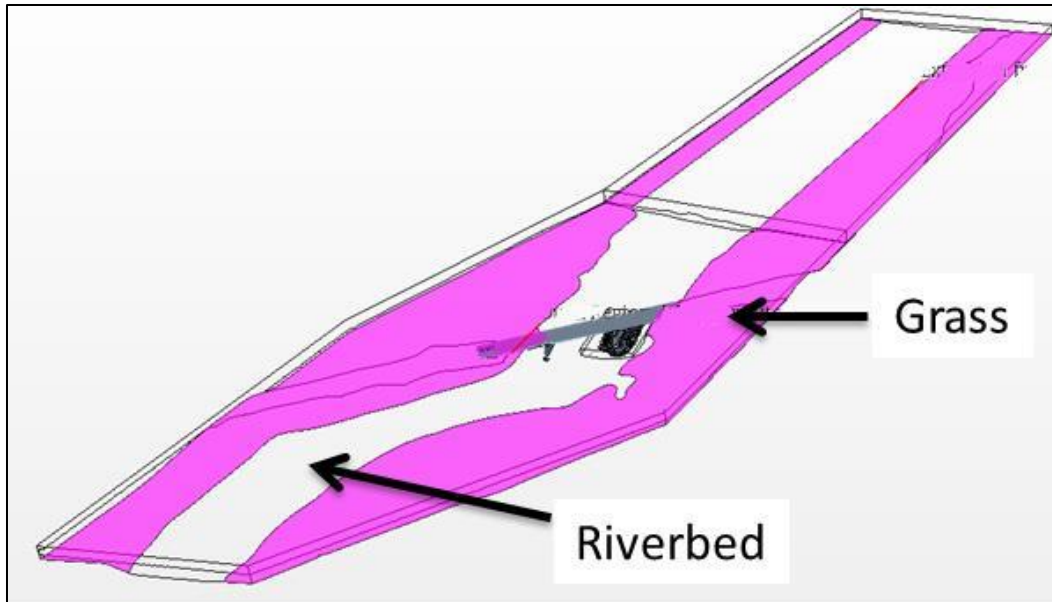


Figure 29. Schematic. CFD model surface characterization.

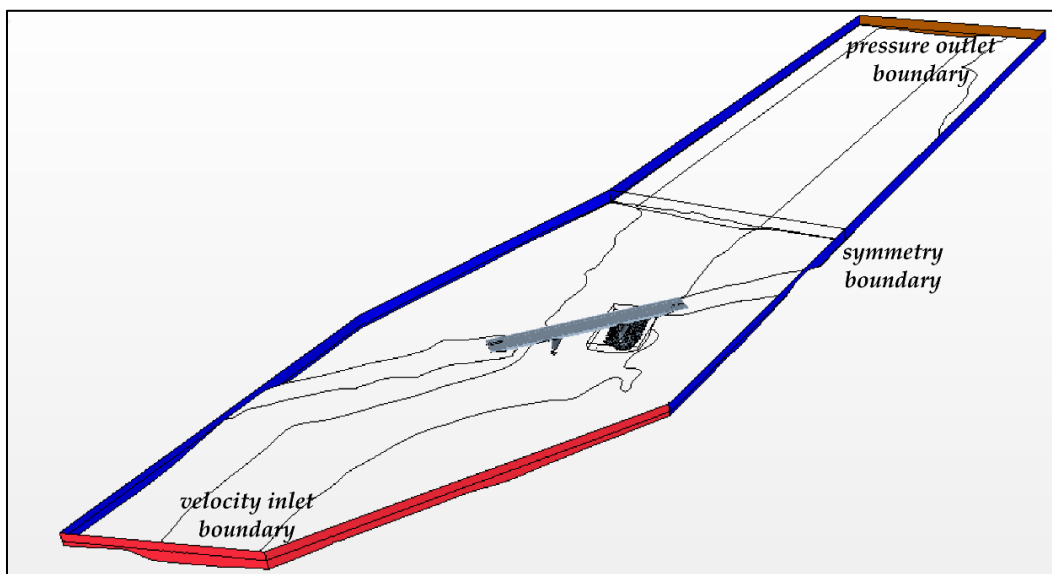


Figure 30. Graphic. CFD model boundaries.

Figure 31 shows the surface mesh of the riverbed in the CFD model with the deepest point near pier 3. STAR-CCM+ software allows for fine gradation of the computational mesh in three dimensions. Very fine meshes can be specified in the areas of highest interest such as pier 3 in this application. Coarse meshes can be used in other areas to reduce computational cost. Local refinements can be further defined based on control volumes, surfaces, or edges.

The region in the vicinity of pier 3 was separated from the rest of the domain in the CFD model to facilitate data exchanges for the subsequent FSI analyses and to control the mesh size. Internal interfaces were placed on the boundaries of that subregion in contact with the outer global region. For the CFD modeling the extended global domain was used. However, for the FSI

computations, only the subregion around pier 3 was used. Figure 32 shows the cross-section through the volume mesh in the global domain. The section marked with lighter (purple) color is the subregion used in the FSI modeling.

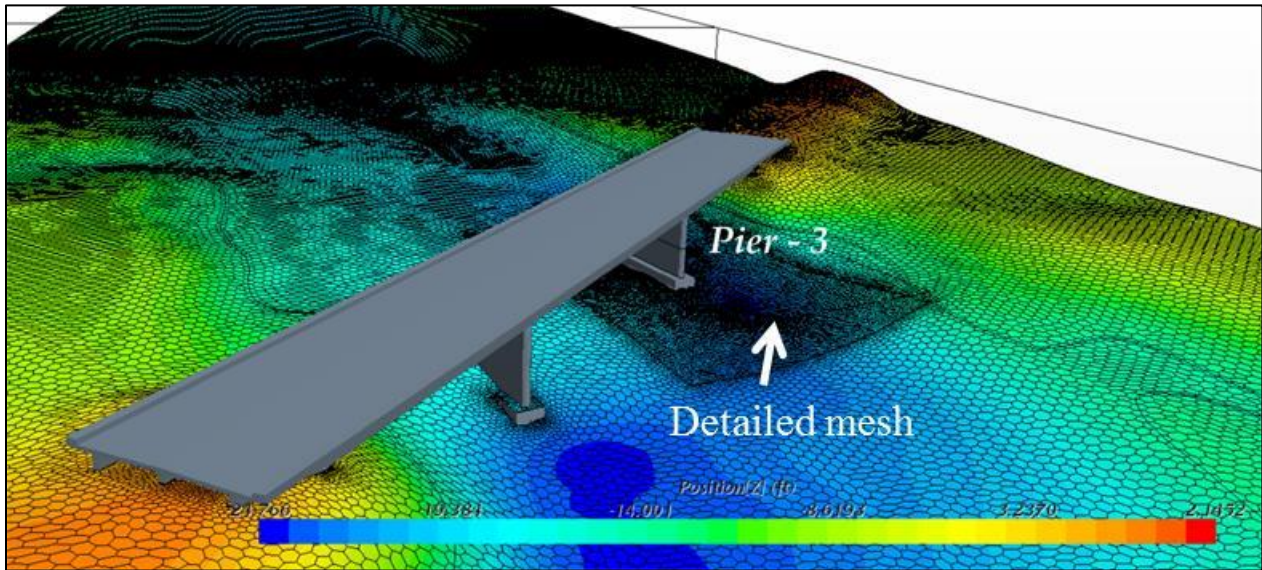


Figure 31. Graphic. Surface mesh of the riverbed in CFD model.

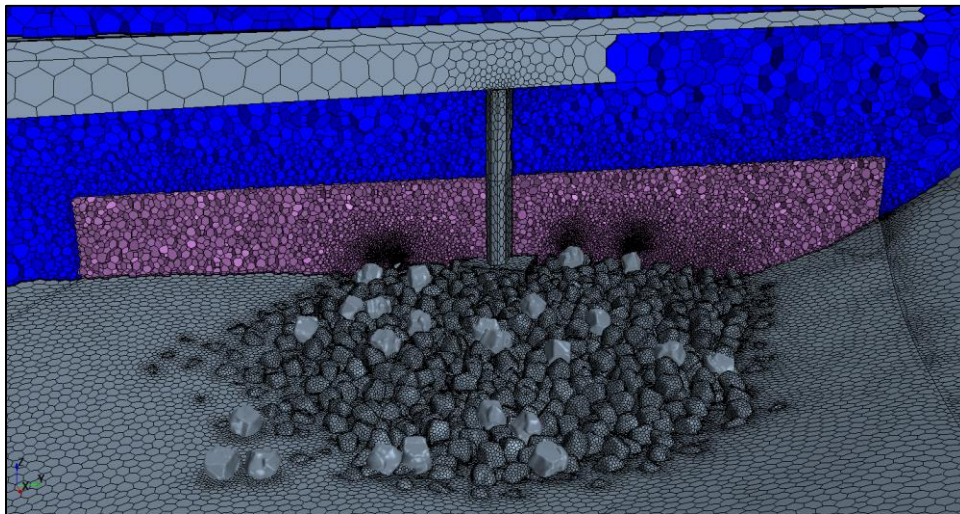


Figure 32. Graphic. Cross-section through the finite volume mesh used for the CFD model.

Figure 33 shows a close-up view of the mesh in the subregion. Mesh in that region is significantly denser than in the rest of the global model. The subregion contained approximately 2.2 million cells, while the global model covering a much larger volume included nearly 4.1 million cells.

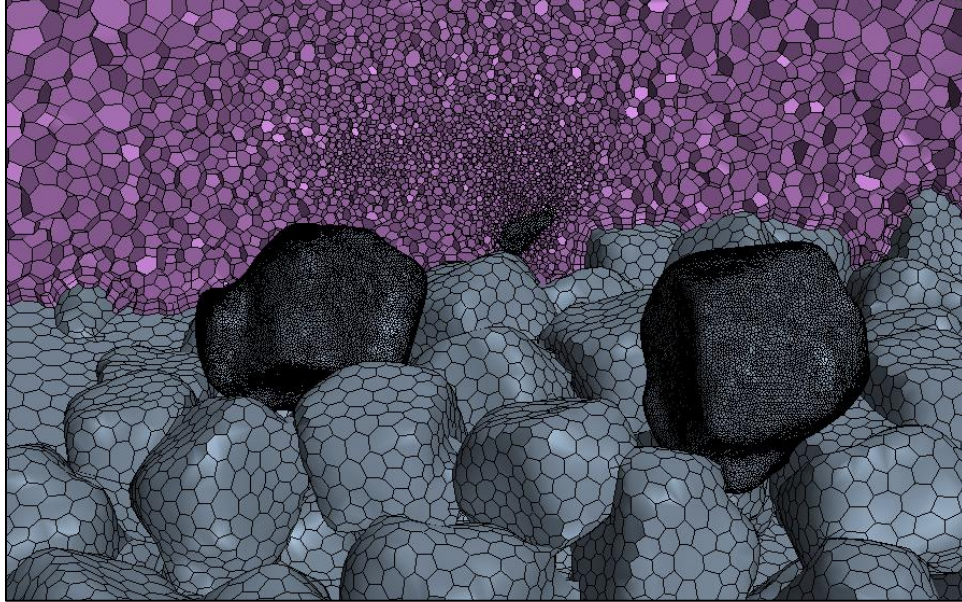


Figure 33. Graphic. Cross-section through the subregion used in the FSI computations.

Riprap Geometry Development

As with the validation effort, the description of the riprap within the numerical models was a significant undertaking. These sections describe the development of these models from the design drawings with adjustments based on sonar soundings.

Geometry Based on Design Drawings

The riprap extent and surface slopes of the rock slope protection (RSP) were initially modeled after the design drawings shown in figure 34 and figure 35. Over 2,500 rocks were included in the CFD model. They were placed in the scour hole semi-manually, meaning smaller clusters of rocks were copied and changed slightly to introduce some variation in their shape and orientation. Once the desired layout was achieved, the STAR-CCM+ surface wrapper was used to smooth the geometry and create a continuous bed boundary. The final triangulated surface of the river bed is shown in figure 36. As noted in chapter 4, the rock geometry is simplified. The shape and orientation of the rocks are much less random than they are in reality and void spaces between the rocks may be larger allowing for more flow within the riprap voids.

Geometry Based on Field Validation

In many riverine environments, as-built conditions may differ from design plans. To investigate as-built conditions, multiple sonar technologies were employed to characterize the bed at the pier. Initially, it was hoped that the sonar would help both in better defining the void spaces within the rock riprap installation, as well as for confirming the overall extent and surface shape of the riprap apron installation.

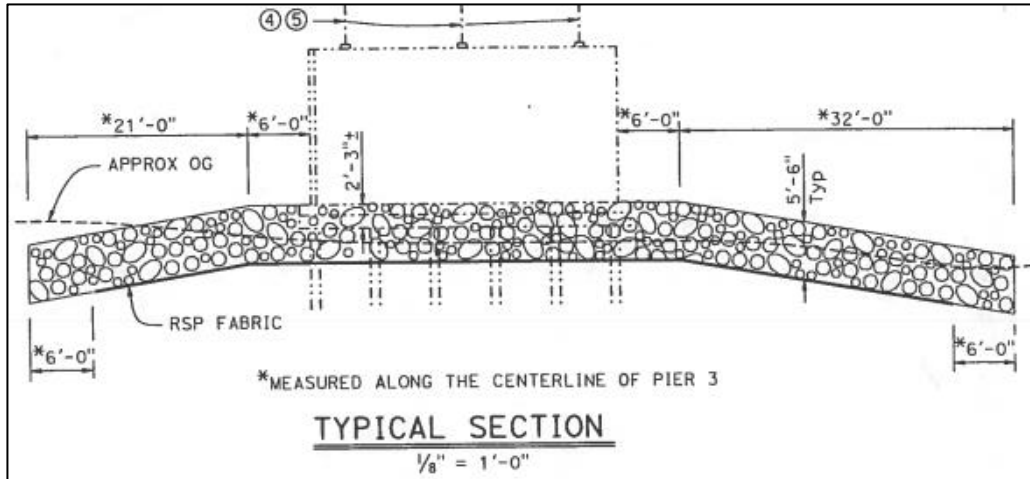


Figure 34. Drawing. Design drawing (typical section) of riprap around pier 3.

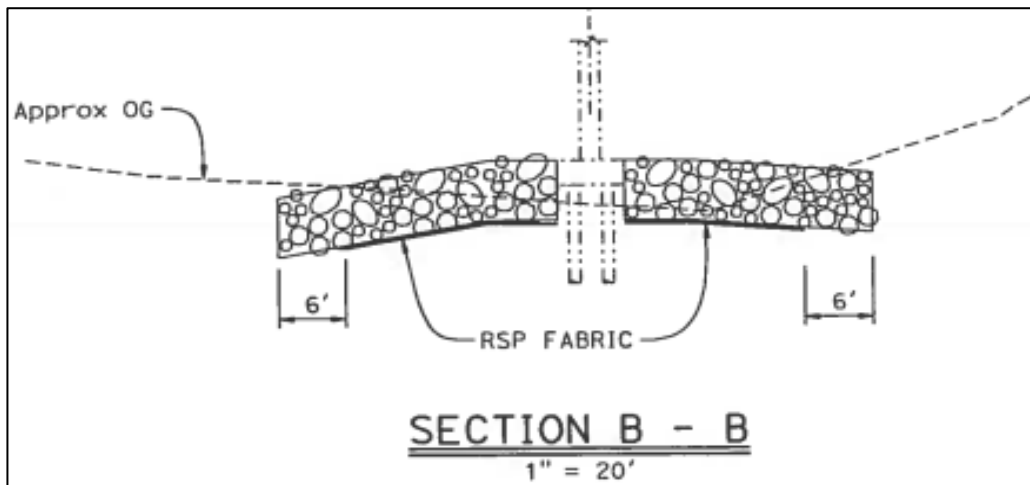


Figure 35. Drawing. Design drawing (section B-B) of riprap around pier 3.

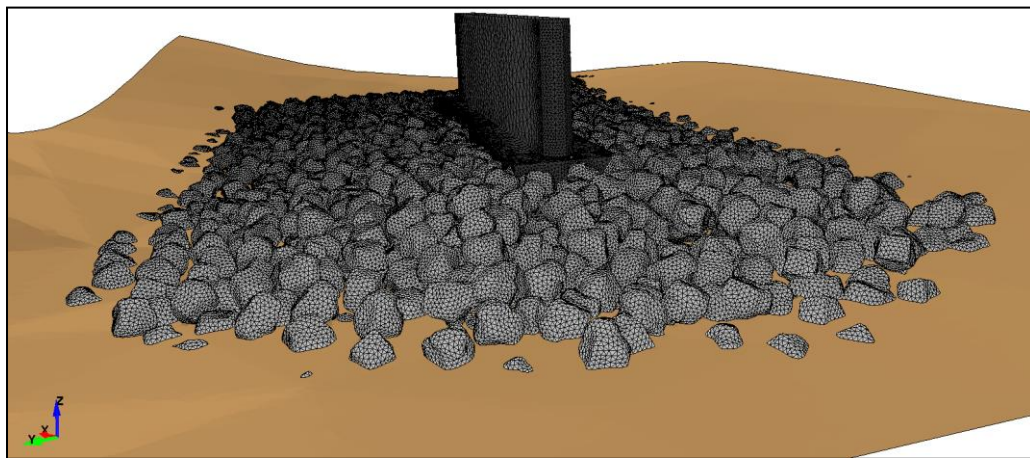


Figure 36. Graphic. Geometry of the riprap used in the CFD model.

With respect to the void spaces, none of the sonar technologies were successful because they were not able to scan voids between the rocks; the void spaces were predominately out of the equipment view lines. Geometries created based on these limited scans would reduce flow between the rocks, effectively closing voids in the rock layers that do not show up in scans.

However, the sonar scans were successful in defining the overall riprap installation geometry. The scans identified the extent of the riprap and surface slopes on each side of the pier. The shape of a new embankment was also identifiable. Figure 37 shows a point cloud based on sonar scanning of the bed.

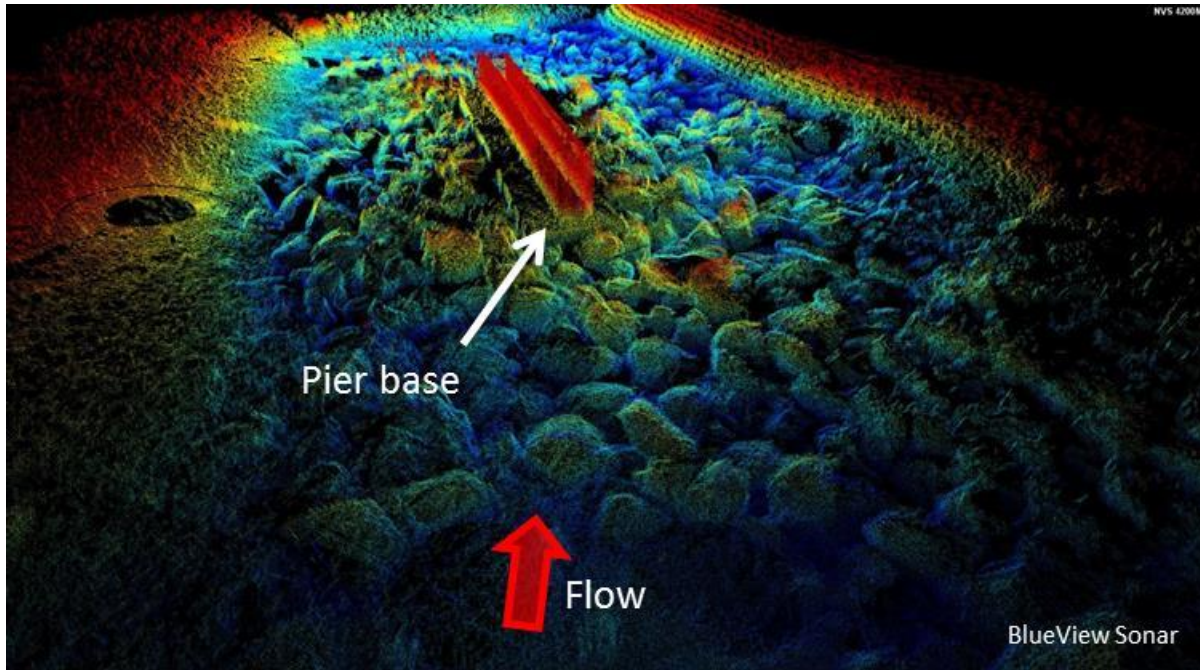


Figure 37. Image. Sonar image of pier 3 with installed riprap.

The scans reveal that the edges of the riprap installation differ from the design plans. An embankment not represented in the design drawings is also apparent in the sonar scans. Figure 38 shows the extent of the boundaries of the riprap installation based on the scan. These boundaries were compared with the extents included in the initial CFD model based on the design plans. The bed geometry and riprap boundaries in the model were adjusted with this new information, including the addition of the embankment on the right (looking downstream) of pier 3.

Figure 39 shows the updated model geometry of the riprap installation near pier 3. Most of the rocks are fixed. As described in chapter 4, movable rocks are placed in key locations for evaluating conditions under which they begin to move. The location of 40 movable rocks for this CFD model are also shown figure 39, in a darker shade.

According to the design documents, the average rock size for the riprap installation was specified to be 1 ton.⁽¹¹⁾ For typical rock density, 1-ton rocks are roughly equivalent to 3-ft (0.91-m) spheres or somewhat larger considering the irregular rock shapes. As a reference, the pier foundation is 6 ft (1.8 m) wide, meaning that the median rock size in the riprap installation should have dimensions slightly more than half of the pier footing width. In accordance with the

specified riprap gradation, some rocks should be larger than 1 ton and some rocks may be smaller.

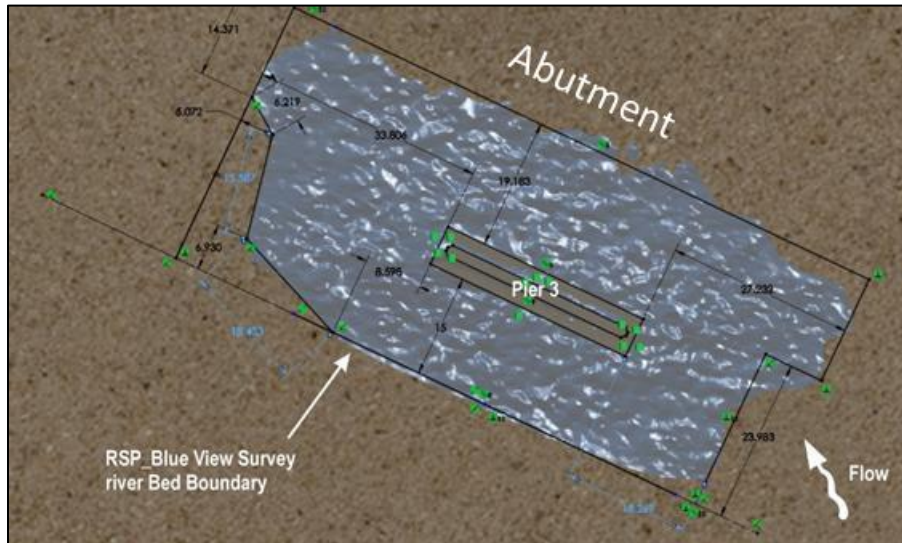


Figure 38. Graphic. The extent of the riprap derived from the sonar bed scan.

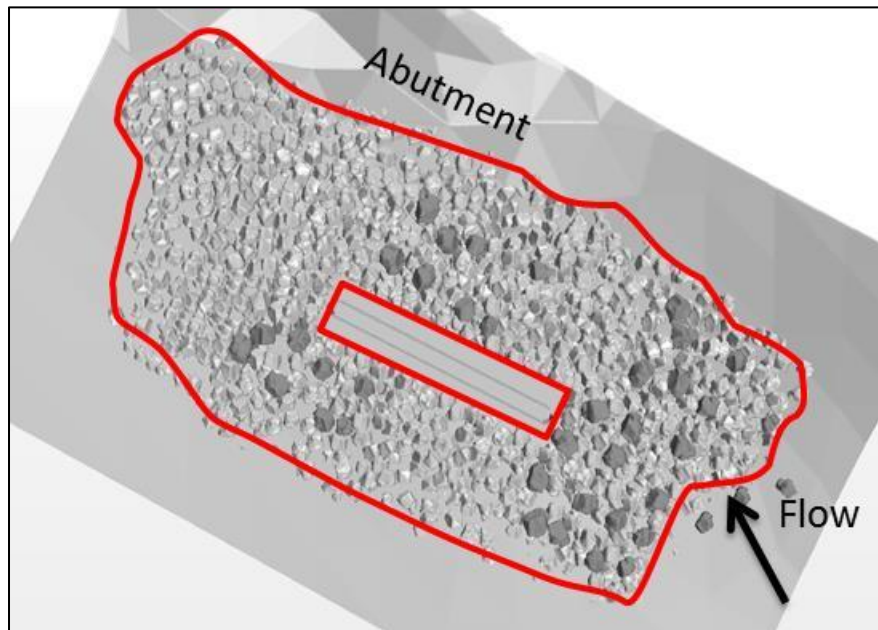


Figure 39. Graphic. Extent of riprap in the updated CFD model with movable rocks.

Inspection of the photo documentation record during the riprap installation (e.g., Figure 27) and the sonar results (e.g., Figure 37) suggests that few rocks at the site exceed 1 ton and many are smaller. Because of this observation, 10 movable rocks in each of 4 sizes (1 ton, 0.8 ton, 0.6 ton, and 0.4 ton) were included in the model.

Movable Rock Placement

The placement of movable rocks for this case study followed the same procedure described in chapter 4. After wrapping, the surface of the rocks was extracted and used in LS-DYNA as a rigid boundary. Approximate locations for the movable rocks were selected before the extraction. Subsequently, the movable rocks were dropped into position in the LS-DYNA simulation so that their final position is semi-random. The simulated drop assures that the rocks are in an equilibrium position before the FSI simulation starts. Figure 40 shows these positions and the rock sizes in the vicinity of pier 3. Some of the movable rocks protrude slightly above neighboring stationary rocks. Several of the smallest rocks (0.4 ton) rest at the front edge of the riprap installation and are entirely exposed to the flow.

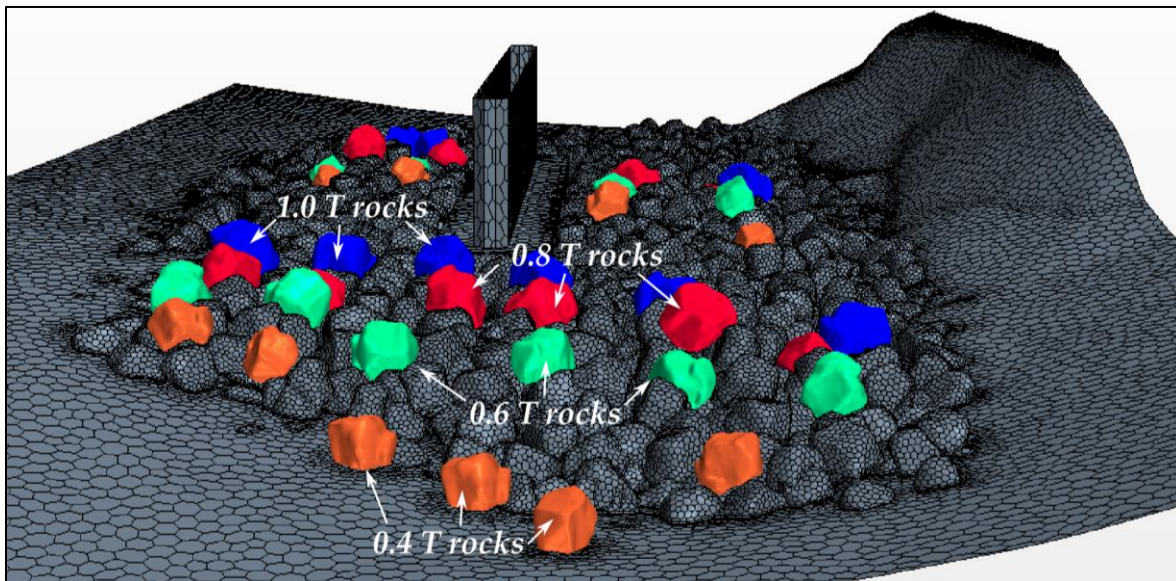


Figure 40. Graphic. Placement of movable rocks around the pier.

COMPARISON OF CFD AND 2D MODEL HYDRAULICS

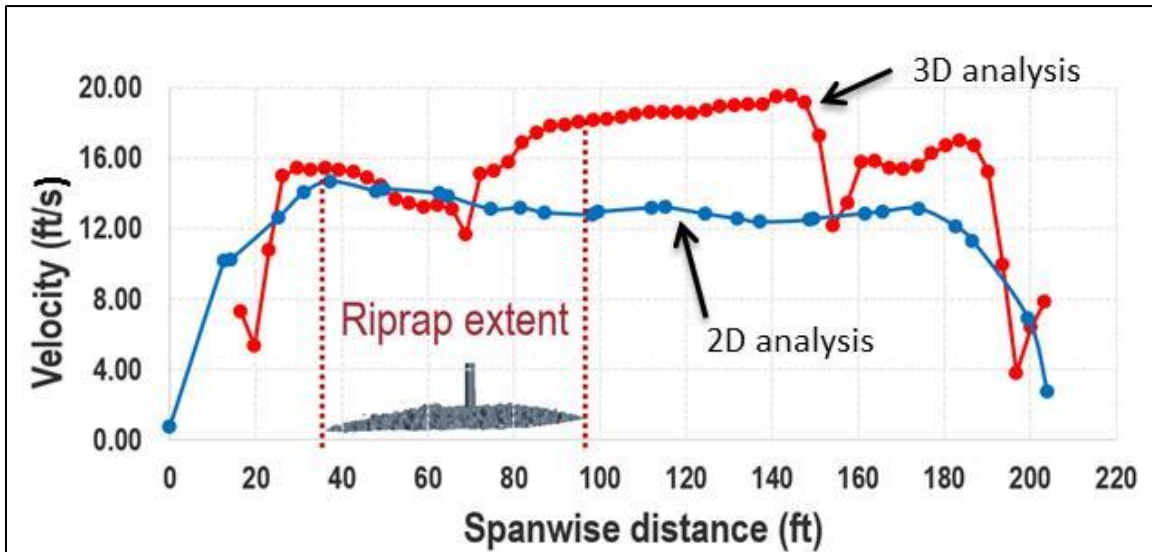
The three-dimensional (3D) CFD analyses were compared with the results of two-dimensional (2D) analyses performed by Caltrans.⁽¹¹⁾ The 100-year discharge of 30,100 ft³/s (852 m³/s) was used in both models. Table 4 summarizes the estimated depths upstream and downstream of the bridge. Both models show a significant elevation change between locations upstream and downstream of the bridge, but the 2D model depths are higher than the 3D model depths. Because of the higher upstream depths, the 2D model predicts that the bridge will be overtopped at the 100-year event, and the 3D model predicts the bridge will pressurize the flow under the bridge but will not overtop it.

Table 4. Comparison of 3D and 2D modeling results for the 100-year discharge.

Parameter	3D CFD	2D
Depth downstream of bridge, ft (m)	11.5 (3.5)	14 (4.3)
Depth upstream of bridge, ft (m)	18 (5.5)	24 (7.3)
Bridge overtopping?	No	Yes

Caltrans noted that for the 2D modeling the downstream boundary water surface elevation was estimated using a normal depth computation and a 0.3 percent slope, which may have resulted in an error of up to 2 ft (0.61 m).⁽¹¹⁾ This might explain some of the differences between the 3D and 2D models downstream of the bridge.

3D CFD calculations were performed with a time step of 0.1 s. Quasi-steady state conditions were achieved in about 700 s of simulated time. It is not trivial to extract depth-averaged velocities (and other quantities) from 3D modeling to compare with the 2D model results. Therefore, the depth-averaged velocity was only calculated for a cross-section under the bridge as shown in figure 41. The velocities are in agreement only on the outer side of pier 3. However, for much of the cross-section, the velocity obtained in the 3D analysis was significantly higher averaging approximately 17.5 ft/s (5.3 m/s) compared with approximately 13.5 ft/s (4.1 m/s) for the 2D analysis. Higher velocities under the bridge estimated by the 3D model are consistent with the lower depths noted previously in table 4.



1 ft = 0.305 m; 1 ft/s = 0.305 m/s

Figure 41. Graph. Depth-averaged velocity estimates under the bridge (looking upstream).

The results shown in figure 41 suggest that rock riprap designed using the 2D modeling results could be under-designed if the 3D results are a better representation of expected circumstances during the 100-year event. Furthermore, the occurrence of pressure flow for the 100-year event

may contribute to under-designed rock riprap. The FSI modeling will be used to explore further the possibility that the rock might be under-designed.

ANALYSIS AND RESULTS

The coupled FSI (CFD and CSM) models were implemented for the Middle Fork of the Feather River for the 100-year flood and two alternative scenarios. The results of the CFD and CSM analyses are described in this section.

Results of the CFD Analyses

From the initial CFD analyses, hydrodynamic forces on all movable rocks were extracted in a local coordinate system aligned with pier 3 and flow under the bridge. Figure 42 shows the location of the rocks with highest forces in each weight category from the CFD simulation of a 100-year flood event. For the 100-year event, the average inlet velocity was 11.1 ft/s (3.38 m/s).

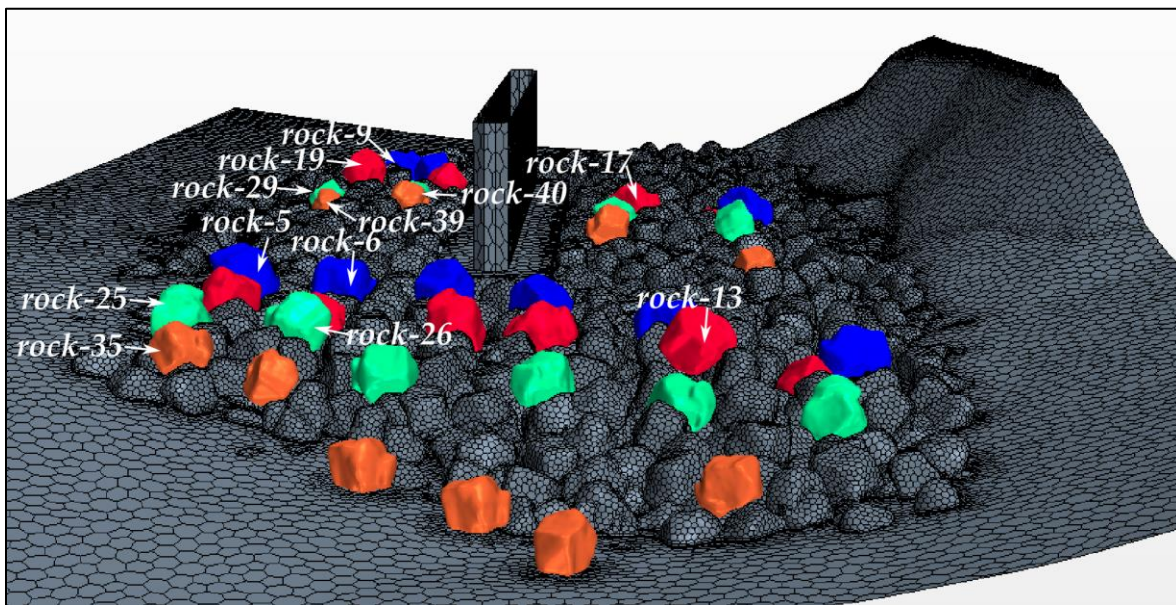


Figure 42. Graphic. Location of the rocks with the highest forces in CFD analysis.

Table 5 summarizes the forces on the rocks, most of which are located to the west of the pier. Although these are the rocks experiencing the highest forces, other factors such as force angle and rock position influence which rocks may move first. The table also includes ratios of the hydrodynamic force on the rock to its weight. For 0.4-ton rocks weighing 800 lbf (3560 N) the ratios range from 0.77 to 0.87 while for the 1-ton rocks weighing 2000 lbf (8900 N) the ratios are lower and range from 0.62 to 0.65. As expected, it appears that the most vulnerable rocks are the smallest. Finally, the table includes information on rocks that move based on the FSI analysis discussed in the following section.

Two additional CFD analyses were conducted using incrementally higher inlet velocity and flow values. Table 5 also summarizes the resulting forces on the identified rocks and the ratio of the resultant forces to the rock weights. Holding the water surface elevation constant, the discharge

and inlet velocities were increased by 10 percent (1.1 times the 100-year) and 20 percent (1.2 times the 100-year).

The objective of increasing the discharge and inlet velocity was to attempt to identify at what conditions the 1-ton rocks will begin to move. Small changes (10 and 20 percent increases) were used to avoid several potential problems. For example, an increase in discharge may make it difficult to compare one result to another because flow under the bridge might be different in these conditions if the entire river is modeled. In addition, overtopping of the bridge may occur for larger floods changing the velocity profile around the bridge.

Table 5. Forces on the critical rocks.

Rock #	Rock Weight (lbf)**	Force (lbf x 10 ⁻³)*						Ratio to Rock Weight**		
		Q ₁₀₀ X Force	Q ₁₀₀ Y Force	Q ₁₀₀ Z Force	Q ₁₀₀ Resultant	1.1 Q ₁₀₀ Resultant	1.2 Q ₁₀₀ Resultant	Q ₁₀₀	1.1 Q ₁₀₀	1.2 Q ₁₀₀
5	2,000	-196	551	1,146	1,285	na	1,488	0.64	<0.67	0.74
6	2,000	-13	378	1,236	1,292	1,467	1,593	0.65	0.73	0.80
8	2,000	na	na	na	na	1,431	1,445	<0.62	0.72	0.72
9	2,000	-294	326	1,157	1,238	1,346	na	0.62	0.67	<0.72
13	1,600	20	247	843	879	980	969	0.55	0.61	0.61
17	1,600	-90	382	831	919	975	1,016	0.57	0.61	0.63
19	1,600	-34	562	1,202	1,328	1,613	1,728	0.83	1.01	1.08
25	1,200	-213	297	775	856	998	1,045	0.71	0.83	0.87
26	1,200	-85	243	775	818	960	1,031	0.68	0.80	0.86
27	1200	na	na	na	na	na	na	<0.68	<0.79	<0.86
29	1,200	-54	238	798	834	946	1,056	0.69	0.79	0.88
35	800	97	281	629	697	807	910	0.87	1.01	1.14
37	800	na	na	na	na	na	na	<0.77	<0.82	<0.98
39	800	22	180	596	622	748	845	0.78	0.94	1.06
40	800	22	270	551	613	654	782	0.77	0.82	0.98

*1 lbf = 4.45 N.

**Shaded ratios indicate rocks that moved from their location based on the FSI analysis.

Another potential problem is achieving realistic 3D CFD multi-phase simulation results in a reasonable amount of time. In VOF free surface simulations, specific conditions are set at a flow inlet, while fairly weak outlet boundary conditions are set. The outlet boundary conditions are normally either a specified pressure or a zero-gradient condition where the mass flow arriving at the outlet simply passes through with no velocity gradient, as though it is a fully developed flow field. A free surface or water elevation cannot be specified at an outlet. The problem with this is that for subcritical flows, the flow in the domain is controlled by the outlet conditions, most importantly the water elevation, that, while known, is not enforced by the software.

To overcome this challenge, the proper specification of the inlet water level and initial conditions in the entire domain is critical. A primary reason is that these flows are normally highly convective and information slowly propagates numerically from the outlet upstream to the inlet. An initial condition that is too far from the final solution may cause a sudden jump in water level at the inlet boundaries raising questions about the validity of the solution domain. Figure 43 illustrates this behavior for an analysis of the entire domain when the discharge was increased by 60 percent above the 100-year conditions.

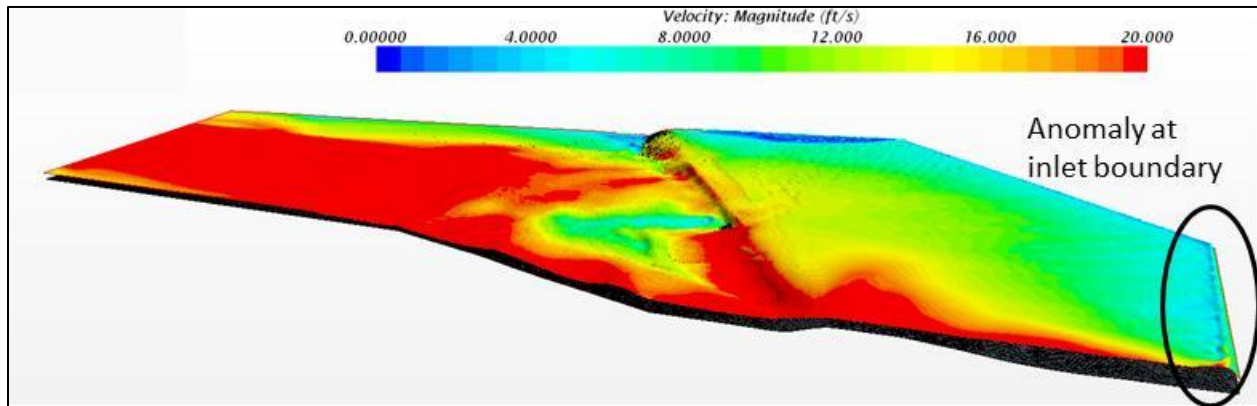
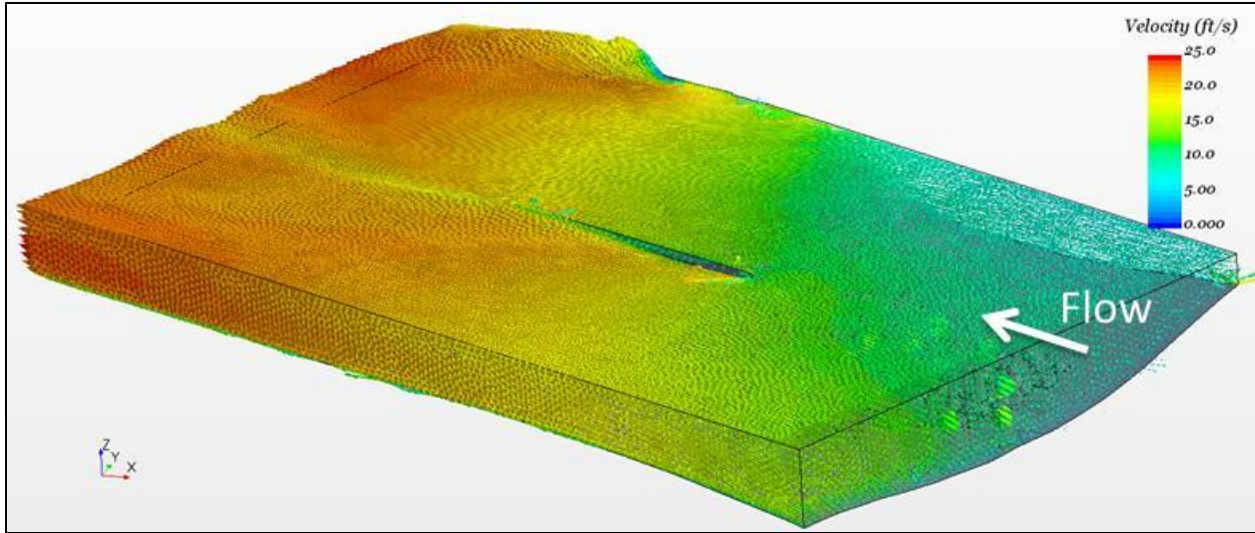


Figure 43. Graphic. Water surface (velocity overlay) for condition of 1.6 times the 100-year flood.

A second reason this challenge is difficult to overcome is that the CFD runs require several days on high performance computers to converge to a quasi-steady state. One solution is to take an iterative approach to adjust the water height at the inlet and the water height in the domain by changing the resistance of the flow in the domain (bed roughness, surface slope, and other solution parameters). However, for this approach to be practical, the size of the domain must be reduced. The reduced domain combined with the iterative approach provides more control over the inlet conditions and, ultimately, a more direct relationship between the inlet velocity and the velocities around the rock riprap installation.

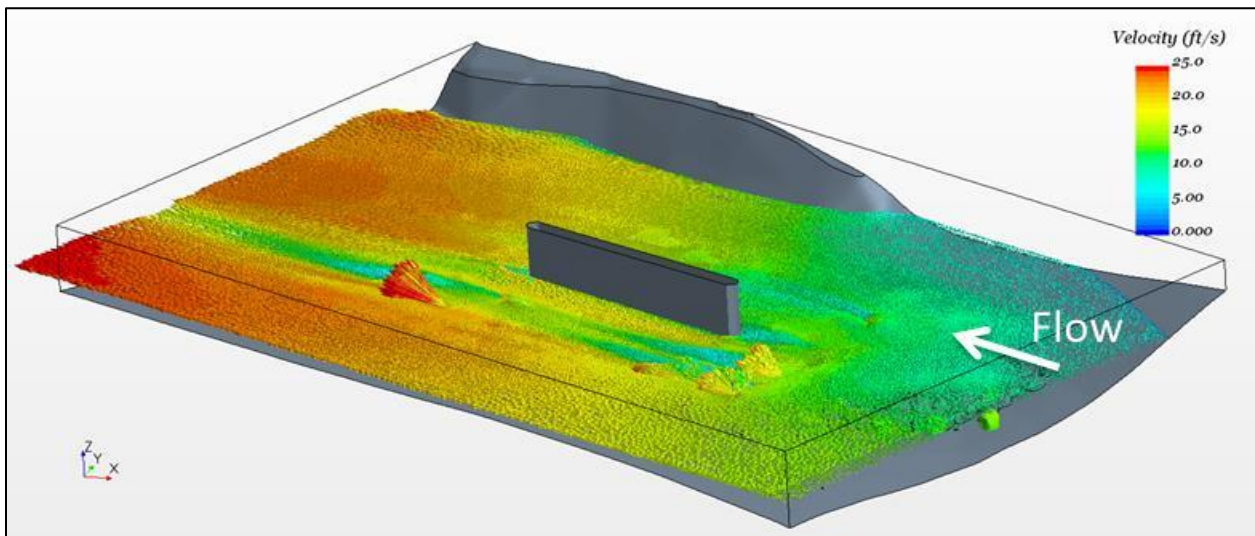
Results of the FSI Analyses

As described previously, only the region closest to the pier with highest scour risk was used in the FSI modeling. The subdomain of interest together with velocity vectors for the 100-year flood on the outer boundaries are shown in figure 44. Velocities in the plane just above the riprap rocks are shown in figure 45. Average inlet velocity on the frontal face for that case was 11.1 ft/s (3.38 m/s).



1 ft/s = 0.305 m/s

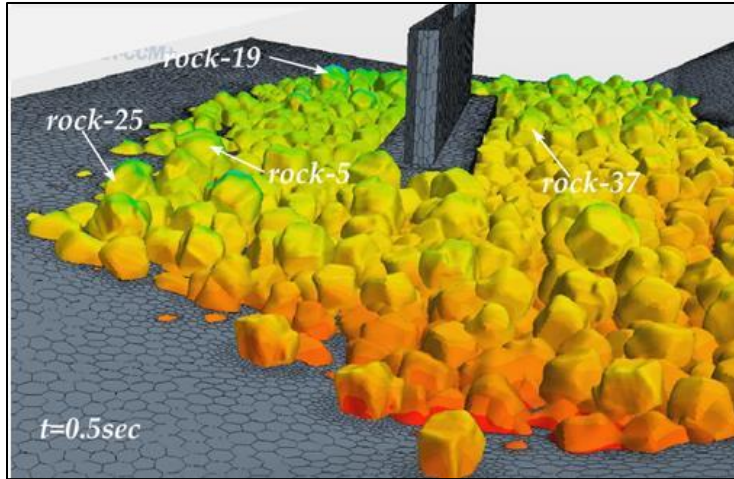
Figure 44. Graphic. Velocity vectors on the interface between the FSI subregion and the CFD domain.



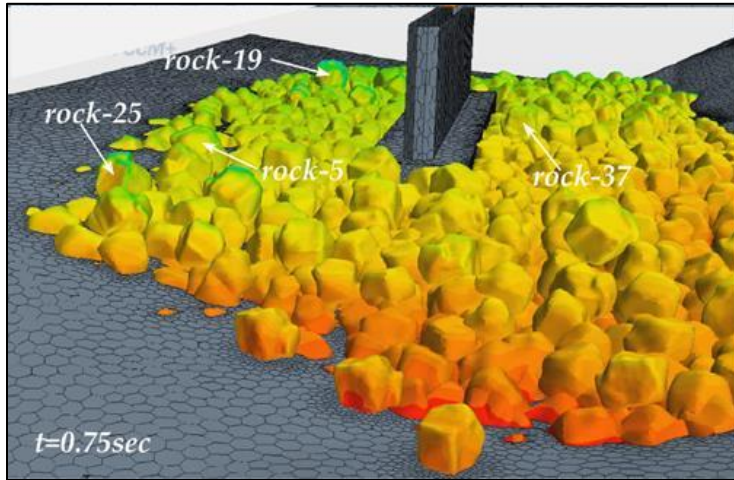
1 ft/s = 0.305 m/s

Figure 45. Graphic. Velocity vectors on the plane just above the rocks.

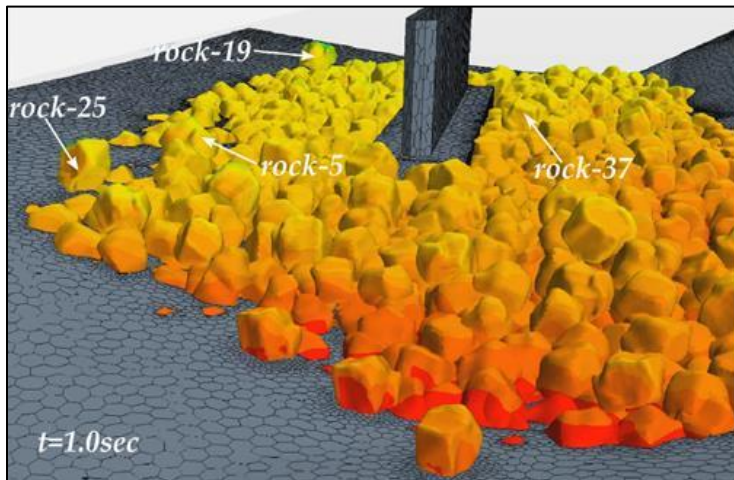
Figure 46 shows snapshots from the FSI simulation for the 100-year flood event. Of the 40 movable rocks in the simulation, only 2 moved from their placed location: rock 25 (0.6 ton) and rock 19 (0.8 ton). Another two—rock 5 (1 ton) and rock 37 (0.4 ton)—only moved locally. Table 5 provides the rock weight ratios and indicates which rocks moved during this simulation. Although all of the rock weight ratios were less than 1, the position and moment arms for the particular rocks contributed to their movement.



A. 0.5 seconds.



B. 0.75 seconds.



C. 1.0 seconds

Figure 46. Graphics. FSI simulation for the 100-year discharge.

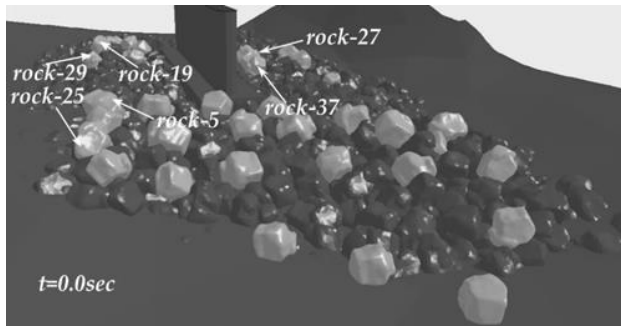
In the FSI simulation for 1.1 times the 100-year flood, movement of 6 out of the 40 movable rocks was detected. Five moved away from their initial positions within the simulated time: rock 5 (1 ton), rock 19 (0.8 ton), and rocks 25, 27, and 29 (0.6 ton). Rock 37 (0.4 ton) moved locally. Figure 47 shows several snapshots from that simulation. Table 5 provides the rock weight ratios and indicates which rocks moved during this simulation. This result also demonstrates that the rocks with the highest forces are not necessarily the ones that will move first because gravity and the reaction forces of surrounding rocks also play an important role in initiating and maintaining motion.

This FSI simulation was not conducted by slowly ramping up the velocity from the 100-year flood simulation as would be accomplished in physical modeling. Rather, a new simulation is started with new flow and boundary conditions. At current levels of computational power and software capabilities, a gradual ramping up of water velocity is too expensive. However, restarting at new conditions may introduce anomalies. For example, movable rock behavior at higher inlet velocities may appear to be unrealistic as instead of rolling over the neighboring rocks they are leaving their positions at steeper angles.

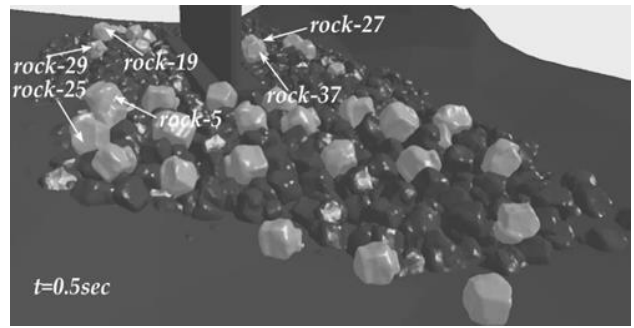
In the next case, the discharge and velocities at the inlet were multiplied by a factor of 1.2 times the 100-year simulation. At this faster flow, with more rocks moving, the mesh around the moving and colliding rocks experiences drastic deformations causing frequent simulation failure. Manual intervention was required to restart the analysis with modified mesh conditions to push the simulation forward. Because of these difficulties, this flow condition was only run for slightly more than 1.0 s of real time.

The FSI analysis indicates that eight rocks moved during the simulation; however, the simulation was not sufficiently long to conclude that other rocks would not have moved given more simulation time. Only a single 1-ton rock moved: rock 5. Also, only one 0.8-ton rock, rock 19, was set in motion. Four 0.6-ton rocks (25, 26, 27, and 29) moved and two 0.4-ton rocks (35 and 37) moved. Figure 48 shows the snapshot series for this flow condition. Table 5 provides the rock weight ratios and indicates which rocks moved during this simulation.

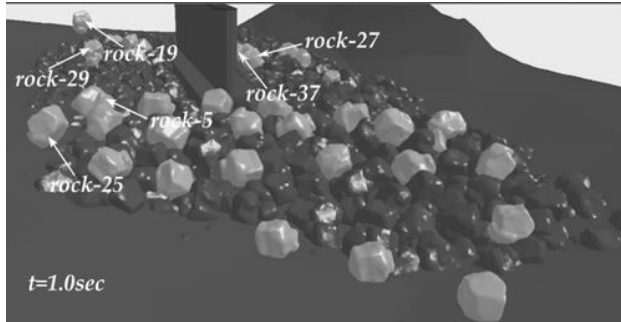
One objective for applying the FSI numerical modeling to the Middle Fork Feather River case study was to evaluate whether these tools could be effective for evaluation or design of riprap apron installations to protect bridge abutments and piers. The riprap installation at pier 3 of the bridge was intended to be stable for the 100-year flood event. The observations from the 100-year simulation were that only 2 rocks out of the 40 movable rocks moved from their original location and that neither of these rocks were the larger 1-ton rocks. When increasing the discharge and inlet velocity by 10 percent and 20 percent, the numbers of rocks moving were 5 and 8, respectively. These observations suggest that the installation will protect the pier foundation at the design discharge, but small increases in the discharge will likely result in riprap installation instabilities and, possibly, failure. Recalling from the validation process for the numerical modeling technique that rocks will move sooner in the numerical simulation compared with the physical situation reinforces the notion that the riprap is adequate for the 100-year flood.



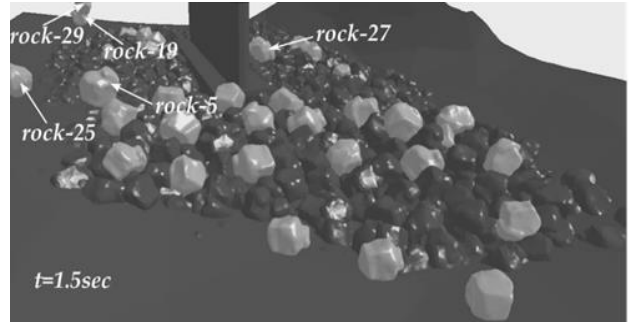
A. 0.0 seconds.



B. 0.5 seconds.

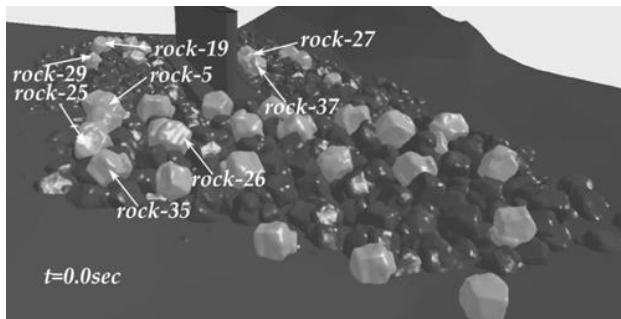


C. 1.0 seconds.

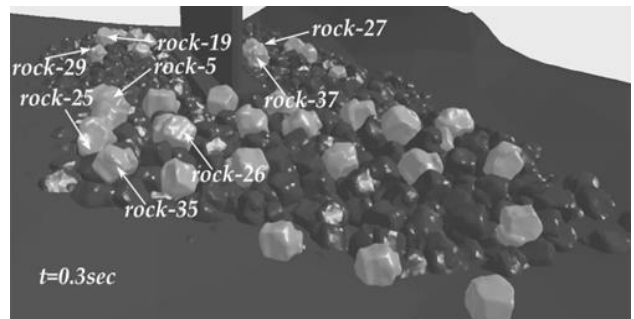


D. 1.5 seconds.

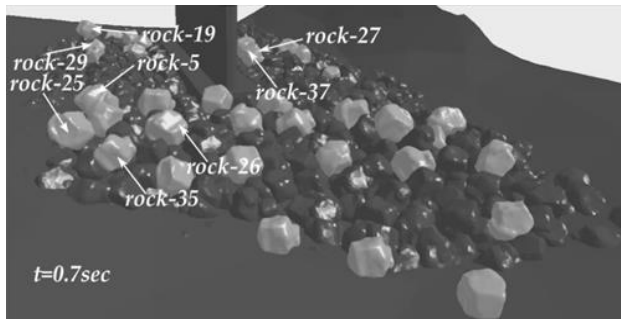
Figure 47. Graphics. FSI simulation for 1.1 times the 100-year discharge.



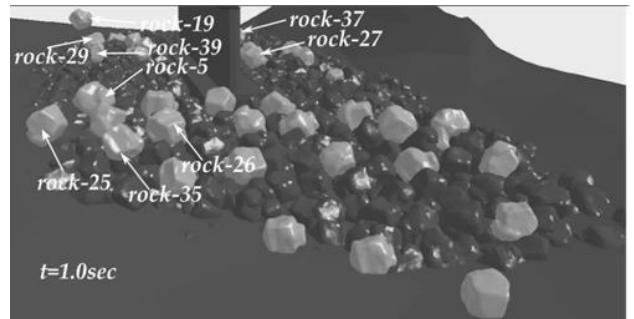
A. 0.0 seconds.



B. 0.3 seconds.



C. 0.7 seconds.



D. 1.0 seconds.

Figure 48. Graphics. FSI simulation for 1.2 times the 100-year discharge.

Working against the conclusion that the riprap will protect the pier foundation is that the bed in the numerical model is fixed except for the 40 movable rocks. Because of this finding, the modeling may not identify fixed locations that might move causing an unraveling of the riprap integrity. In addition, the fixed bed does not allow for evaluation of the potential for undermining of the riprap resulting from an inadequately designed or installed filter layer.

CHAPTER 6. CONCLUSIONS AND RECOMMENDATIONS

As stated in the introduction, the objectives of this research study were to:

- Assess whether detailed FSI modeling can inform evaluation of rock riprap movement for both the analysis of existing riprap aprons and for the design of new riprap aprons.
- Develop recommendations for the design, installation, and monitoring of riprap apron installations at bridge piers and abutments, where feasible.

With respect to the first objective, the results of this study demonstrate that detailed FSI modeling can inform evaluation of rock riprap movement for both the analysis of existing riprap aprons and for the design of new riprap aprons. A new advanced computational methodology for assessing failure risk of geometrically complex riprap installations was developed for this study. This methodology solves the onset of motion analysis problem as a weakly coupled FSI problem. In this method, the detailed flow force distribution on riprap rock surfaces including both pressure and local shear on the solid surface was computed using the 3D CFD software STAR-CCM+. The CFD software is coupled through file data exchanges with the computational structural mechanics software LS-DYNA. The flow threshold for the onset of motion of riprap rocks was computed for a set of representative rocks for both simplified laboratory and complex field conditions.

Physical laboratory experiments were used to validate the FSI numerical modeling. Qualitative agreement was demonstrated between the experiments and the simulations with the numerical modeling estimating rock movement at somewhat lower velocities. Given the engineering simplifications needed to run the numerical modeling over several weeks after problem setup, the conservative numerical modeling result was considered to be good.

The FSI approach was tested on a complex field case study of a riprap installation at a pier for a bridge over the Middle Fork of the Feather River. Preparation of the numerical model used sonar scans of the as-built riprap installation. Observations of the effectiveness of this numerical modeling application include:

- Sonar scans of the riprap installation were useful in defining the boundaries of the riprap at the site and confirmation of as-built conditions was useful for establishing the model. However, the data from the scan could not be used to generate the bed geometry of the computational domain because the scans did not capture hidden interstitial spaces between riprap rocks.
- The FSI analysis showed that the onset of motion did not necessarily occur for the rocks with the highest flow force to weight ratios. The analyses confirmed that the reaction forces that arise from the arrangement and position of rocks with respect to their neighbors play a significant role in the initiation of motion.
- The numerical modeling suggests that the riprap installation at pier 3 remains stable during the 100-year flood because only 2 of 40 movable rocks moved during the simulation and none of those moved were the larger 1-ton rocks. However, this conclusion is tentative because most of the bed around the pier is stationary in the model.

- The numerical modeling suggested that the installation at pier 3 may unravel with small increases of flow and inlet velocity. Increases of 10 and 20 percent over the 100-year values resulted in the movement of 5 and 8 rocks, respectively. Not only do these represent a significant portion of the movable rocks, but the movement included a 1-ton rock.
- It is unclear whether more rock motion would be observed if all rocks in the riprap installation could move. The fact that some rocks are immovable likely creates a more stable situation than would be experienced in the field.
- This FSI numerical modeling procedure does not account for the effects of undermining whether filters (filter fabric or granular) are omitted or improperly installed.

Evaluation of the numerical modeling technique also considered its costs and availability. The cost is certainly much more expensive than a relatively quick calculation using current riprap sizing formulas. The method is also not broadly available to the design community because high performance modeling facilities and expert modeling skills are required. Therefore, candidate applications for using FSI analyses to assess new or retrofit riprap installations would be those in which the project cost is significant or the risks of failure are catastrophic.

With respect to the second objective, the study identified recommendations for improving the design, installation, and monitoring of riprap apron installations at bridge piers and abutments:

- Verifying as-built conditions is important for assuring that the intended level of protection has been achieved. For the Middle Fork Feather River case study, the photographic record of the installation combined with sonar scan images indicated that the riprap installation was not installed as designed. A larger fraction of rocks smaller than 1 ton seemed to be present than the gradation permitted.
- Monitoring for changes in stream morphology is critical because changes may significantly alter conditions from those anticipated at design.
- Recording the date of rock riprap installations and monitoring the performance of the installations after major floods is needed to insure the riprap apron continues to provide the needed protection.
- Sonar technologies may be a useful means for riprap monitoring.
- Rock riprap installations for piers are not recommended by FHWA policy.
- The FSI modeling approach has the potential for supporting the evaluation of riprap sizing equations such as those in HEC-23. However, the limited experiments in this study do not provide sufficient basis for such an evaluation.

The FSI numerical modeling approach shows promise for supporting the design and evaluation of riprap installations for bridge abutments and piers. As computer capabilities increase and more detailed representations of rock riprap installations become more practical, the approach should continue to increase in its utility. At such time as the computational requirements are reduced sufficiently and the modeling representation of riprap and other countermeasures is sufficiently accurate, this technology should be tested for use in further evaluation of countermeasures and for the development of design guidelines.

APPENDIX A. ANNOTATED BIBLIOGRAPHY

This appendix contains an annotated bibliography of literature addressing riprap as a countermeasure for pier scour and related topics. Much of this literature describes failure Modes and layout guidelines.

RIPRAP AT BRIDGE PIERS

Riprap is commonly used to protect bridge piers from scour and has been studied for decades. In 1929, Engels produced one of the earliest reports of the use of riprap at bridge piers that was based on the results of hydraulic model experiments undertaken in 1893.⁽¹⁴⁾ Prior to these experiments, it was the general opinion that the greatest danger to pier foundations occurred at the downstream end of the pier rather than the upstream end and it was common practice to place riprap around the piers up to the low water mark. Engels concluded that the protection was most needed at the upstream end of the pier and that the riprap should be placed flush with the bed.

In 1959, de Sousa Pinto completed his thesis “Riprap Protection Against Scour Around Bridge Piers” under the supervision of Dr. C. J. Posey at the State University of Iowa.⁽¹⁵⁾ His study examined the use of riprap protection against erosion around a circular pier. Riprap layouts around the pier were circular with “filter” grading with respect to the sand bed. Various layout diameters and levels of placement were studied and a correlation was obtained between the needed size of the protection and the dimensions of the unprotected scour hole. An exploratory study of possible modifications on the design of the protective layer was undertaken. Among the conclusions from this study were as follows:

- The Terzaghi-Vicksburg riprap specifications for a horizontal layer around the pier provide an efficient protection against scour. It was observed, moreover, that a certain deviation from the Terzaghi-Vicksburg specifications can be tolerated without appreciable loss of filter properties.
- Unless the velocity of flow is too high for the size of the riprap, the stability of the layer as a whole depends on the conditions at the edge. When the edge is unexposed or leveled with the bed, no movement of the particles is observed. If the sand is eroded around the layer, then failure of the protection starts to take place.
- For a circular pier, a criterion was obtained to determine the required areal extension of the riprap protection. The riprap layer should be extended to the dimensions of the unprotected scour hole at the corresponding level of emplacement. All indications are that such a criterion can be extended to other pier geometries; however, further study is recommended before a definite conclusion can be reached.
- A test indicated the possibility of modifying the riprap layer by sloping down the layer and reducing the thickness toward the edge. Future study should indicate the most convenient solution from the points of view of safety and economy.

The Schoharie Creek bridge failed in 1987 and was attributed to inadequate pier riprap, resulting in a significant increase in the interest in riprap protection of bridge piers.⁽⁵⁾ The failure of the I-90 bridge over Schoharie Creek near Albany, New York on April 5, 1987, cost 10 lives. The

foundations of the four bridge piers were large spread footings without piles. The footings were set into the stream bed in very dense ice contact stratified glacial drift, which was not considered erodible by designers at the time. However, subsequent flume studies of samples of the stratified drift showed that some material would erode at velocities that might occur at design flood flows.

Design plans for the Schoharie Creek Bridge called for the footings to be protected with riprap. Over a period from 1953 to 1987, much of the riprap was removed by high flows. The National Transportation Safety Board (NTSB) gave as the probable cause "...the failure of the New York State Thruway Authority (NYSTA) to maintain adequate riprap around the bridge piers, which led to severe erosion in the soil beneath the spread footings. Contributing to the severity of the accident was the lack of structural redundancy in the bridge."

The NYSTA inspected the bridge annually or biennially with the last inspection before the failure on April 1, 1986. A 1979 inspection by a consultant hired by the New York State Department of Transportation indicated that most of the riprap around the piers was missing; however, the 1986 inspection failed to detect any problems with the condition of the riprap at the piers. Based on the NTSB findings, the conclusions from this failure are that inspectors and their supervisors must recognize that the presence of some riprap does not necessarily make a bridge safe from scour, and inspectors must be trained to recognize when riprap is missing and the significance of this condition.

As reported in 1993, Ruff and Nickelson conducted experiments to examine the effect of riprap size and coverage on reducing local scour at bridge piers.⁽¹⁶⁾ Pier diameter, bed material size, and riprap size were varied during the study. Scour depths with no riprap were compared with scour depths with a single layer riprap mat with 100- and 50-percent areal coverage. They found that scour depths could be reduced 40 to 99 percent by placing a riprap mat around the pier that is 5 to 8 times the diameter of the pier.

They also concluded that the extent of riprap coverage is an important parameter in predicting scour depths. Scour essentially ceased when the riprap slid or rolled into the scour hole and formed a mat of approximately 100 percent of riprap coverage in the scour hole when it started at 50-percent coverage on the bed. This study emphasized the need for periodic inspections of bridge pier riprap protection because time and floods can remove individual rocks in a riprap mat and reduce the coverage, thereby reducing the degree of protection originally intended.

Parola investigated the stability of riprap at bridge piers by considering the influences of the 3D flow on the trajectory of bedload sediment, the seepage gradient within the streambed, and boundary stresses.⁽¹⁷⁾ Maximum mean boundary stresses were inferred from velocity measurements to assess riprap stability. The stability of riprap was considered with respect to several dimensionless parameters. Relative size of the rock compared with the pier and elevation of riprap placement were shown to significantly influence the stability of riprap. Parola also made recommendations regarding the minimum extent of riprap protection required to protect the streambed around piers.

Parola also noted that the local pressure variation on the streambed can be substantial. He built on the work of others who showed that the change in pressure along the streambed can vary significantly from the front corner of a pier to the side of the pier and that such pressure

differentials could set up seepage gradients that cause the removal of fine-grained material from beneath the riprap protection.^(18,19) Parola concluded that pressure fluctuations on the streambed near separation zones and under wake vortices could cause streambed material to migrate through riprap protection. To prevent this migration, a properly designed filter should be placed below the riprap protection, especially near corners of rectangular piers and in the region of wake vortices. Riprap should be extended to cover regions of high boundary stresses and regions where sediment is diverted from the streambed. Parola noted that the extent of the riprap layer is sensitive to the angle between the approach flow direction and the longitudinal axis of the pier; therefore, all likely angles of attack should be considered when designing riprap protection. Protection of the region downstream of the pier is required for circumstances in which scour holes downstream of the pier are unacceptable.

Bertoldi et al. completed a study of several scour protection countermeasures as remedial alternatives for scour at bridge piers.⁽²⁰⁾ Countermeasures were evaluated in terms of failure Modes and techniques for analyzing expected stability. Alternatives to riprap vary in size, shape, and mass as well as in their design flexibility. The authors evaluated grout mats and grout bags, extended footings, tetrapods, cable-tied blocks, high-density particles, tile mats, and anchors (used in conjunction with other countermeasures). While riprap is the most common and best documented scour protection at bridge piers, alternatives are used for many situations, such as when riprap is not available, unreasonable riprap sizes would be required for high velocity streams, or riprap placement would be difficult. The study provided insight into the overall behavior and effectiveness of various countermeasures:

- Confirmed previous recommendations to extend the countermeasure at least two pier widths laterally from the pier to provide adequate protection from local scour.
- Confirmed the need for filter fabric (or other filter material) to seal voids between the pier and countermeasure.
- Determined that two techniques were appropriate for analyzing stability: (1) particle displacement criteria patterned after Shields and Izbash incipient motion formulas and (2) drag coefficients to characterize overturning forces. Both of techniques involve dimensionless parameters that can potentially be transferred from laboratory to full-scale conditions.
- Confirmed that loose particle countermeasures such as rock riprap, tetrapods, or other precast concrete particles and high-density particles can be analyzed by particle displacement criteria and can be compared with one another by using an equivalent spherical diameter as a characteristic size.

Chiew published a paper addressing the mechanics of riprap failure at bridge piers.⁽²¹⁾ In this study, experiments conducted in a laboratory flume identified three different Modes of riprap failure at a cylindrical bridge pier. Acting alone or in combination, these Modes of failure are as follows:

- Shear failure: the riprap stones are too small or light to withstand the down flow and horseshoe vortices associated with the pier scour mechanism under the given flow condition.

- Widdowing failure: widdowing of the underlying finer bed material through the voids or interstices of the coarse riprap stones.
- Edge failure: the instability at the edge of the coarse riprap layer stones and the finer bed material initiates the formation of a local scour hole that affects the stability of the riprap.

The study proposed a semi-empirical method to size stones for riprap protection. The experimental data showed that a thick riprap layer can prevent widdowing in the absence of a filter layer. The thick riprap layer can also sustain a partial breakup of the layer with the capability of rearmoring the scour hole, preventing a total disintegration of the riprap layer. Finally, the study proposed empirical relationships that describe the effects of riprap thickness and cover on the stability of the riprap layer.

In a subsequent effort, Lim and Chiew examined failure mechanisms of riprap layers around a cylindrical bridge pier under live-bed conditions.⁽²²⁾ They concluded that the most important factors affecting the stability of the riprap layer are the turbulent flow field around the pier and fluctuations of the bed level caused by the migration of bed features past the pier. The latter phenomenon causes the riprap stones to lose their support. Observations showed that the riprap stones will eventually degrade to a level defined by the height of the largest dune and the local pier scour.

Further work by Lim and Chiew examined the failure behavior of a riprap layer around a cylindrical bridge pier.⁽²³⁾ The study confirmed the inherent flexibility of a riprap layer to offer a self-healing process. This flexibility helps to reduce further erosion under a steady flow condition allowing an equilibrium state to be attained when the erosion ceases. When the flow velocity was increased steadily, the riprap layers eventually failed in two Modes: total disintegration and embedment. The failure occurred when the erosion power is higher than the self-healing ability. The study showed that the eventual failure Mode can be determined by comparing the relative magnitude of the critical shear velocity of the bed sediment and the adjusted threshold velocity of the riprap layer.

Melville et al. performed a laboratory study of the stability of riprap protective layers at piers under mobile-bed conditions.^(24,25) The authors emphasized the role of the placement level of the riprap layer in maintaining stability. The results indicated that the deeper the initial level of the riprap layer, the lesser the depth of local scour at the pier, i.e., the better the protection afforded. They also noted decreasing riprap stability with increasing flow velocity and discussed mechanisms of riprap layer disintegration.

Melville et al. reported four failure mechanisms during the live bed study:

- Shear failure: the riprap stones are entrained by the flow because they are too small to resist movement.
- Widdowing failure: the finer underlying bed material is eroded through voids between riprap stones.
- Edge failure: scouring at the periphery of the riprap layer undermines stones.
- Bedform-induced failure: passing bed forms cause riprap settlement.

The first three Modes were previously observed under clear water conditions.⁽²¹⁾ The additional mechanism relates to the presence of bed forms in a mobile bed. When a deep trough passes the pier, settlement of the riprap layer is initiated. Further settlement can occur if there are subsequent deep troughs that pass. The fluctuating bed level caused by the movement of bed features causes the riprap stones to lose support and stability. If the trough of the bed form is deeper than the riprap layer, stones are undercut and move down into the lower trough region. Ahead of the bed forms is an area of high turbulence and correspondingly high shear stresses are induced for short periods. Riprap stones can be plucked from the layer and be transported to the lee of the pier and beyond. Removal of stones allows increased winnowing.

Hoffmans and Verheij created a scour manual to provide civil engineers with practical methods to calculate the dimensions of scour holes and to furnish an introduction to the most relevant literature.⁽²⁶⁾ The manual reflects the cumulative findings of Dutch scour research projects. Among other topics, the manual provides specific guidance on the schematically simplified shape and extent of a pier scour hole as a function of the side slopes, the radius of an upstream half circle, and the length of the axis of a downstream half ellipse. From these schemata, the volume and minimum extent of bed protection can be determined. Citing other literature, the manual recommends estimating a minimum length of bed protection around circular bridge piers based on the projected width of the pier.^(19,27) However, if the width of the pier influences the flow pattern strongly (e.g., if the pier width is half of the flow width), the cited relations are not applicable.

In another study to determine countermeasure effectiveness to protect bridge piers, Parker et al. determined that placing a geotextile under a riprap layer with the same areal coverage as the riprap layer, resulted in a relatively poor riprap performance.⁽²⁸⁾ With live-bed conditions, the rocks at the edges tended to slide or be plucked off, exposing the underlying geotextile and ultimately resulting in failure of the riprap layer as successive bed forms passed and plucked more rocks from the riprap layer. Additional test results from the study confirmed that riprap performance was best when a geotextile filter extended two-thirds the distance to the periphery of the riprap.

Fotherby and Ruff evaluated large scale riprap and concrete armor units to prevent pier scour.⁽²⁹⁾ They combined the data generated from their study with that of previous studies to demonstrate that countermeasure equations are adequate when a ratio of the characteristic axis length of the countermeasure to the pier width is less than 0.15, but are conservative for greater values of the ratio. In addition, they proposed a design procedure that enveloped the points of incipient motion of riprap and several shapes of concrete armor units. The procedure incorporates the relative pier size and provides the recommended dimensions for the countermeasure.

Chiew and Lim performed live-bed experiments to examine the failure behavior of riprap at a cylindrical bridge pier.⁽³⁰⁾ They observed that riprap fails in one of two Modes: total disintegration or embedment. The former refers to the break-up of the entire riprap layer where the stones are washed away by the flow field generated at the pier. The latter refers to the burying (embedment) of the riprap in the sediment. The authors proposed a criterion to demarcate the limiting condition between the two types of failure. In addition, they observed that embedment failure is the more common riprap failure Mode under live-bed conditions. The causes of embedment failure are twofold: (1) bed feature destabilization and (2) differential

mobility. Bed level fluctuations caused by the propagating bed features resulted in bed feature destabilization, whereas differential mobility is the result of the different response of the riprap stones and bed sediments to the flow field. Experimental results also showed that the riprap layer can degrade to an equilibrium level for a given flow condition. Finally, the authors proposed a semi empirical equation to compute the maximum depth of riprap degradation, which occurs at the upper end of dune regime.

Transit New Zealand and its predecessor the National Roads Board had long recognized the national importance of bridge scour research in New Zealand. Since about 1972, these bodies have supported many bridge scour research projects, the majority of which were completed at the University of Auckland with the involvement of Dr. Bruce Melville. Recognizing the need for a summary of the state of knowledge of bridge scour, Transfund facilitated the preparation of the Bridge Scour Manual.⁽⁶⁾ This manual provides comprehensive coverage of bridge scour primarily based on procedures, guidance, and experience developed in New Zealand.

Thirty-one detailed case studies of scour-induced bridge failure (primarily in New Zealand) are presented in the Manual. These provide designers with an understanding of processes involved and also cases against which design methodologies can be tested. One chapter presents principles of scour-resistant design along with a comprehensive summary of scour protection methods and remedial methods for preventing bridge scour.

Lim and Chiew performed a parametric study of riprap protection around a cylindrical bridge pier with uniform bed sediments.⁽³¹⁾ The authors examined the role of riprap layer thickness, cover width, and placement level, as well as the median grain size and density of the riprap stone on the riprap stability. Maintaining an undisturbed approach flow depth, the tests were conducted with a sequence formation of ripples, dunes, and transition flat bed. Observations showed that a riprap layer will eventually degrade to a maximum embedment level. The embedment velocity was defined as the velocity at which the riprap layer has embedded to its maximum level. The experimental results showed that variations of the characteristic parameters have no influence on the embedment failure at the upper end of the dune regime. The authors also proposed a maximum embedment velocity that defines a critical flow velocity at which all riprap layers will fail, irrespective of the characteristic parameters.

Lauchlan and Melville evaluated failure mechanisms, stability, and placement level effects for riprap at bridge piers.⁽³²⁾ The authors assessed the ability of riprap stones to protect bridge piers under a wide range of flow conditions. The effects of placing the riprap layer at depth within the sediment bed, rather than level with the bed surface, were also investigated. The study showed that, as the flow velocity increases, the ability of riprap stones to protect a pier decreases asymptotically until the scour depth in the riprap layer reaches that of an equivalent unprotected pier. In addition, it was found that the deeper the placement level the less exposed the riprap was to destabilizing bed forms and the better the protection against local scour. Lowering the placement level also meant that the riprap performed better than for surface-placed layers as the flow velocity increased. The Mode of riprap failure also changed as the placement level below the bed surface is lowered. A pier riprap size prediction equation was proposed, including a parameter to account for placement level. The authors concluded the following:

- Destabilization of riprap layers protecting bridge piers by the progression of bed forms past the pier is the dominant failure Mode under live-bed conditions. Edge, shear, and winnowing mechanisms play secondary roles.
- Riprap stones subside into the bed sediment with the passage of bed forms past the pier and eventually settle at the level of the passing bed-form troughs. The stones subside as a layer and therefore remain capable of providing protection.
- Under live-bed conditions, over a range of riprap stone sizes, the relative local scour depth increased asymptotically with relative flow velocity up to a point. This result is in agreement with the findings of others.⁽³⁰⁾
- Riprap installed below the sediment bed surface is less vulnerable to the destabilizing influence of passing bed forms and is, therefore, more effective in protecting the pier.
- Under live-bed conditions, a larger stone size provides a greater scour protection for a given flow intensity. It is possible to predict the stone size necessary to provide a certain degree of local scour protection.
- Increasing layer thickness increases riprap stability, with an approximate 70 percent reduction in local scour when increasing the layer thickness from 1 to 3 times the median rock size.
- Synthetic filter layers placed beneath the riprap improve riprap stability. The lateral extent of the synthetic filter should be limited to about 75 percent of the lateral extent of the riprap. The reduced coverage of the synthetic filter ensures that edge stones in the riprap layer are able to protect the synthetic filter from being rolled-up by the flow.
- The pier size, relative to the riprap size, has a relatively minor effect on riprap stability under live-bed conditions. This finding is contrary to that of Parola for clear-water conditions.^(17,33)
- Neither pier shape nor pier alignment is a significant factor in terms of riprap stability.

Chiew conducted an experimental study examining local scour and riprap stability at bridge piers in rivers subject to bed degradation.⁽³⁴⁾ The data showed that the equilibrium bed profile associated with the “with” or “without” pier condition is essentially the same, except for the section around the pier. Total scour depth is shown to be the sum of bed degradation and local pier scour depth. The latter can be computed from the time-averaged live-bed scour depth associated with the undisturbed velocity ratio before bed degradation.

Chiew notes that when an alluvial channel bed degrades, a riprap layers around bridge piers is subject to destabilization. Experimental observations showed that the initial instability of the riprap stones occurred at the riprap layer boundary with the finer bed sediment. As bed degradation starts, edge stones experience undercutting, causing them to slip into the scour region. With time, dune forms move toward the riprap layer causing more stones to be displaced especially when the dune trough arrives at the pier. As general scour took place over a long duration, a mound eventually formed as more edge stones slid onto the degraded bed. An auxiliary test showed that the mound is very vulnerable to another flood flow accompanied by large dunes. This type of riprap instability is defined as bed-degradation induced failure.

The objectives of the NCHRP Report 593 study were to synthesize information and studies evaluating countermeasures to protect bridge piers from scour and to provide recommendations for guidelines and specifications for their design, construction, inspection, maintenance, and performance evaluation.⁽⁵⁾ The report included several pier scour countermeasures including riprap, partially grouted riprap, articulating concrete blocks, gabion mattresses, grout mattresses, and geotextile sand containers. The objectives were accomplished with the support of extensive testing in the hydraulics laboratory at Colorado State University.

The report notes that when properly designed and installed, riprap has an advantage over rigid countermeasures for pier scour protection because it is flexible when under attack by river currents. It can remain functional even if individual stones may be lost and it can be repaired relatively easily. Properly designed and installed riprap can provide long-term protection if it is inspected and maintained on a periodic basis as well as after flood events. For State transportation departments, riprap has been the most common countermeasure installed at bridge piers.

Gaps in the current state of the practice were summarized in NCHRP Report 593 and a specific test, or series of tests, was designed to address each deficiency. Each test series was designed to permit one configuration to be carried forward to the next series. This served to quantify the repeatability of the test program as well as to identify inconsistencies that could arise in the experimental set up. In addition, the testing program addressed stability and performance issues associated with the extent of the countermeasure placement around the pier, and the termination details at the pier and around the periphery of the installation. In addition, various filter types and extents were investigated. The design intent for the riprap coverage tests included examination of the following:

- Areal coverage and edge treatment with recommended geotextiles.
- Areal coverage variation from HEC-23 with recommended geotextiles.
- Areal coverage and thickness variation from HEC-23 with recommended geotextiles.
- Scour hole extent with recommended geotextiles.
- Scour hole extent without filters.
- HEC-18 guidelines.⁽³⁵⁾
- Thickness and filter variation from HEC-23 guidelines.
- Mounded riprap without filters.

Riprap used for pier protection is often placed on the surface of the channel bed because of the ease and lower cost of placement and because it is more easily inspected, but it may also be placed in a pre-existing scour hole, or in a hole excavated around the pier. Test results indicated that when the stable baseline riprap configuration was mounded on the surface without a filter, the performance was poor. Given the same areal extent of riprap coverage, none of the riprap in the mounded riprap test configurations performed as well as riprap in test configurations with the top of the riprap level flush with the bed,. This study concluded that mounding riprap around a

pier is not acceptable for design in most cases, because it obstructs flow, captures debris, and increases scour at the periphery of the installation.

Numerous riprap studies suggest that thickness of the riprap layer placed around the bridge piers should be between 2 to 3 times median stone size of the riprap.⁽²⁾ Testing for NCHRP Report 593 indicated that 3 times the median stone size is appropriate for specifying minimum thickness and that performance improved with increasing riprap layer thickness.

Results from riprap testing indicated that riprap areal coverage should be a minimum of two pier widths in all directions. Riprap should be placed in a pre-excavated hole around the pier so that the top of the riprap layer is level with the surrounding channel bed elevation. Placing the top of the riprap flush with the bed is ideal for inspection purposes, and does not obstruct the flow. The riprap layer should have a minimum thickness of 3 times the median rock size.

Additional tests confirmed that the lateral extent of riprap protection at rectangular piers must be increased when the longitudinal axis of the pier is skewed to the flow direction. Tests also confirmed that a filter should not be extended fully beneath the riprap; instead, the filter should be terminated two-thirds the distance from the pier to the edge of the riprap. Other recommendations regarding the riprap extent and layer thickness were included in the report.

Periodic and post-flood inspection practices were also evaluated. Pier riprap is typically inspected during biennial bridge inspection programs. However, more frequent inspection might be required for a particular bridge or group of bridges that are designated as vulnerable or after floods exceeding a critical threshold. The following guidance is presented in a National Highway Institute (NHI) course for bridge inspectors:⁽³⁶⁾

- Riprap should be angular and interlocking.
- Riprap should have a granular or synthetic geotextile filter between the riprap and the subgrade material.
- Riprap should be well graded (a wide range of rock sizes). The maximum rock size should be no greater than about twice the median size.
- For bridge piers, riprap should generally extend up to the bed elevation so that the top of the riprap is visible to the inspector during and after floods.
- Riprap inspections should determine the following, which are strong indicators of problems:
 - Has riprap been displaced downstream?
 - Has angular riprap blanket slumped down slope?
 - Has angular riprap material been replaced over time by smoother river run material?
 - Has riprap material physically deteriorated, disintegrated, or been abraded over time?
 - Are there holes in the riprap blanket where the filter has been exposed or breached?

RIPRAP AT BRIDGE ABUTMENTS OR IN STREAM CHANNELS

Riprap is frequently used as a countermeasure to protect bridge abutments from scour, as well as to stabilize stream channels. In a United States Geological Survey (USGS) study for FHWA, Brice and Blodgett developed guidelines supporting the design, maintenance, and construction of countermeasures for reducing bridge losses attributable to scour and bank erosion.⁽³⁷⁾ These guidelines are based on case histories of 224 bridge sites in the U.S. and Canada, interviews with bridge engineers in 34 states, and a survey of published work on countermeasures. Each case history (in volume 2) includes data on bridge, geomorphic, and flow characteristics; a chronological account of relevant events at the site; and an evaluation of hydraulic problems and countermeasures. Problems at piers and abutments were identified at 100 and 80 sites, respectively. While the study does not focus on riprap for pier scour protection, several relevant conclusions were included:

- Hydraulic problems are attributed to local scour at about 50 sites, to general scour at about 55 sites, and to lateral erosion by stream action at about 105 sites.
- Countermeasure performance is rated primarily on how well it served its intended function, but also on whether it sustained damage or produced any unwanted effects. According to the "principle of expendability," a countermeasure that serves its purpose most economically is likely to be damaged.
- Flexible revetment has a better record of performance at study sites than rigid revetment such as concrete pavement. Failures of riprap, a flexible revetment, are attributed to factors already taken into account by existing design guidelines.
- Riprap keyed in place by tamping is more stable than loose riprap, and a lesser volume of rock per unit area is required.
- As protection for piers, dumped rock riprap proved to be effective at most sites where it could be evaluated. There is some evidence that the riprap should be placed so that the top is below, rather than level with, the streambed.

Blodgett and McConaughy developed guidance for riprap design for stream channels near highway structures.⁽³⁸⁾ Design procedures used for design of rock riprap revetment installations were evaluated using data from 26 field sites. Four riprap failure Modes were identified: (1) particle erosion, (2) translational slide, (3) modified slump, and (4) slump. Particle erosion occurs when individual particles are dislodged by the hydraulic forces generated by flowing water. Particle erosion can be initiated by abrasion, impingement of flowing water, eddy action/reverse flow, local flow acceleration, freeze/thaw action, ice, or toe erosion. Factors associated with riprap failure included stone size, bank side slope, size gradation, layer thickness, insufficient toe or end wall, failure of the bank material, overtopping during floods, and geomorphic changes in the channel. One conclusion from a review of field data and the design procedures suggested that estimates of hydraulic forces acting on the boundary based on flow velocity rather than shear stress were more reliable. Several adjustments for local conditions, such as channel curvature, superelevation, or boundary roughness, may be unwarranted in view of the difficulty in estimating critical hydraulic forces for which the riprap is to be designed. Success of riprap is related not only to the appropriate procedure for selecting stone size, but also to reliability of estimated hydraulic and channel factors applicable to the site.

While not specific to pier riprap, the authors discuss general characteristics of riprap failure and note that inadequate recognition of the type of erosion process that is occurring or improper riprap design may lead to failure of the riprap. Types of erosion that can be successfully controlled by riprap include channel degradation, bank erosion, scour, and changes in alignment associated with meandering, branching, and braiding of streams. The rate of channel erosion varies with time, but is primarily a function of the magnitude of streamflow. The major characteristics of the riprap layer include: (1) thickness, (2) placement method, (3) toe construction, (4) stone gradation, and (5) filter blankets.

A comprehensive design manual on the use of rock in hydraulic engineering was prepared by the Netherlands Center for Civil Engineering Research and Codes (CUR) and the Rijkswaterstaat, Dutch Public Works Department (RWS) between April 1988 and December 1993 under a collaborative project.⁽⁷⁾ In many countries, rock is a commonly used construction material in hydraulic engineering. This Manual provides a standard reference on this subject, addressing the entire lifecycle of rock structures. The Manual sets out to answer the question "Why use rock in hydraulic engineering?" with the following observation:

Rock is basically used as a material to protect all kinds of hydraulic structures against erosion and as such it has a number of major qualifications. Protective and other layers when made of rock are flexible and follow slight settlements. Besides, local damage or loss is easily repaired, construction is generally not complicated and rock is usually durable and recoverable. Last but not least, depending on transport distance and means of transport, for many locations rock is the most cost-effective material for the protection of erosion-prone slopes of structures or beds in a marine or inland environment.

Section 2.2.2 of the Manual describes various failure mechanisms (or failure Modes) of rock structures, with emphasis on the functions of rock in these structures. Failure can be simply defined as the exceedance of a predefined limit state, which occurs when the loading exceeds the strength. When this exceedance occurs, a failure response of the structure (or parts of it) can be defined. Failures can occur both during construction and operation. Typical loadings and responses for rock are wave height and displacement relative to the as-built position. Both loading and response are functions of time. The response is also determined by the characteristics of the rock system such as weight and shape. The loading may, to a certain extent, be affected by the system, for example through permeability.

Failure corresponds to unacceptable displacements and/or deformations. The associated loading is defined as a failure loading. In general, failure mechanisms (or failure Modes) are named after their consequent displacements or movements and the common characteristic is a relatively large increase of response (e.g., stone movements) resulting from a minor increase in loading (e.g., wave height).

The Manual emphasizes the importance of inspection and maintenance for any riprap installation and notes that a proper balance of costs for inspection and maintenance and the capital costs of the scheme is desirable. To achieve this scheme, an inspection and maintenance plan is necessary. This maintenance plan should be available at the design stage so that the design can be adjusted to suit the inspection and maintenance procedure or vice-versa. For instance, if after

construction inspection and maintenance is not possible then the design must have a low probability of failure.

In order to develop an inspection and maintenance plan, it is necessary to consider the following ways riprap armor may fail:

- Sudden collapse of embankment of which the rock structure forms a part:
 - Sliding of embankment along failure planes in the subsoil, for instance caused by rapid decrease of water level in rivers or reservoirs or caused by scour at the toe of a slope.
 - Liquefaction caused by earthquakes.
 - Failure of transitions.
- Sudden collapse of bed protection layer:
 - Damage by ships (negative keel clearance, dragging anchors, propeller jets).
 - Attack by high waves or current.
 - Scour at the edge, followed by liquefaction.
 - Vandalism (removal of elements).
- Sudden local failure of bed protection:
 - Transition failure.
 - Vandalism (removal of individual elements of protection layer).
- Rapid degradation of bed protection from a grossly undersized protection layer.
- Gradual degradation of embankment and bed protection:
 - Deterioration of individual elements of protection layer from climate and solar effects.
 - Deterioration of exposed geotextile caused by ultraviolet radiation.
 - Clogging up of underlying filter.

The Manual treats the following as special structures regarding bed/scour/bank protection works:

- Pipeline and cable crossings.
- Fish sluices.
- Anchoring structures.
- Bridge piers.
- Jetties.

As such, the design of these and similar structures is outside the scope of the Manual. However, the Manual does provide example calculations for bridge pier scour (Section 8.4). For designing

protection against pier scour, the Manual notes that it is more important to know the areal extent vulnerable to scour than the depth of scour.

In October 1998, the FHWA, the American Association of State Highway and Transportation Officials (AASHTO), and the Transportation Research Board (TRB) sponsored a scanning review of European practice for bridge scour and stream instability countermeasures.⁽³⁹⁾ This review involved a Panel of representatives from FHWA, state departments of transportation (California, Illinois, Maryland, Minnesota, Oregon, and South Carolina), universities, and the private sector. The review included visits to highway research institutes, hydraulic research laboratories, and field sites in four countries: Switzerland, Germany, the Netherlands, and the United Kingdom. Scanning review objectives were as follows:

- Review and document innovative techniques used to mitigate the effects of scour and stream instability at bridges.
- Evaluate these techniques for potential application in the United States.
- Share information on U.S. practice.

The scan found that the use of riprap, in combination with a geotextile or granular filter, is by far the most common scour and stream instability countermeasure in all four countries visited. The availability, economy, ease of installation, and flexibility of riprap were considered highly desirable characteristics. As a result, considerable effort has been devoted to techniques for determining size, gradation, layer thickness and horizontal extent, filters, and placement techniques and equipment for revetment and coastal applications. In Europe, riprap is considered an effective and permanent countermeasure against channel instability and scour, including local scour at bridge piers.

The scan also noted that great care is taken in placing riprap at critical locations, and in many cases stones are placed individually in the riprap matrix. Highly specialized equipment has been developed by construction contractors in Europe for placing riprap, particularly for coastal installations. The use of bottom dump or side dump pontoons (barges) is common in both Germany and the Netherlands. Some of the smaller pontoon systems, particularly the bottom dump pontoons developed in Germany could be used to place riprap in water at larger bridges.

European hydraulic engineers consider placing an effective filter beneath riprap in flowing or deep water critical to the success of the installation. The use of large geotextile sand containers at the Eidersperrwerk in Germany, the use of a geotextile mattress filled with granular filter material at the Eastern Scheldt Barrier in the Netherlands, and the use of fascine sinker mats at both locations are examples of these innovative placement techniques. The availability of testing apparatus to ensure that geotextiles perform as required and the development of specific codes to guide the design and installation of geotextiles contribute to the success of these installations. Engineers in all four countries referred to a Dutch design manual for rock applications in hydraulic engineering as a primary reference guide.⁽⁷⁾

NCHRP Report 568 represented a major synthesis effort to develop riprap design criteria, recommended specifications, and quality control guidelines for riprap for a range of applications.⁽²⁾ The applications included revetment on streams and riverbanks, bridge piers and

abutments, and bridge scour countermeasures such as guide banks and spurs. This synthesis study did not involve any original laboratory or field work. A fundamental premise of the study was that riprap is an integrated system and that successful performance of a riprap installation depends on the response of each component of the system to hydraulic and environmental stresses throughout its service life.

For pier scour riprap protection, the report includes laboratory results and design recommendations from a concurrent study for countermeasures to protect bridge piers from scour.⁽⁵⁾ The recommendations included filter requirements, riprap extent, and other construction and installation guidelines for riprap at piers. Guidelines for the use of geotextile containers as a means of placing a filter for pier riprap derived from European practice are presented. Construction and installation guidelines and constructability issues are investigated, including: dumping vs. controlled placement, underwater versus dry installation, and buried versus mounded placement.

HEC-23 identifies and provides design guidelines for bridge scour and stream instability countermeasures that have been implemented by various State departments of transportation (DOTs) in the United States.⁽¹⁾ Countermeasure experience, selection, and design guidance are consolidated from other FHWA publications and NCHRP research studies in this document to support a comprehensive analysis of scour and stream instability problems and provide a range of solutions to those problems. Selected innovative countermeasure concepts and guidance derived from practice outside the United States are introduced.

Volume 1 contains a chapter on riprap design, specifications, and quality control as well as an expanded chapter on biotechnical countermeasures. Volume 2 contains nineteen detailed countermeasure design guidelines grouped into six categories: (1) stream instability, (2) streambank and roadway embankment protection, (3) bridge pier protection, (4) abutment protection, (5) filter design, and (6) special applications.

Volume II DG 11 provides specific guidance for rock riprap at bridge piers. DG 11 notes that design of a pier scour countermeasure system using riprap requires knowledge of the river bed and foundation material; flow conditions including velocity, depth and orientation; pier size, shape, and skew with respect to flow direction; riprap characteristics of size, density, durability, and availability; and the type of interface material between the riprap and underlying foundation. The system typically includes a filter layer, either a geotextile fabric or a filter of sand and/or gravel, specifically selected for compatibility with the subsoil. The filter allows infiltration and exfiltration to occur while providing particle retention.

Bridge pier riprap design is based, primarily, on research conducted under laboratory conditions with limited field verification. Flow turbulence and velocities around a pier are of sufficient magnitude that large rocks move over time. Bridges have been lost as a result of the removal of riprap at piers resulting from turbulence and high velocity flow. Usually the loss of riprap does not happen during one storm, but is the result of the cumulative effect of a sequence of high flows (e.g., Schoharie Creek). Therefore, if rock riprap is placed as scour protection around a pier, the bridge should be monitored and inspected during and after each high flow event to ensure that the riprap is stable.

APPENDIX B. COUPLING AND VALIDATION OF THE FSI MODELS

This appendix provides details of the coupling and verification for the FSI solutions used in this study. This information is taken from Bojanowski et al.⁽¹⁰⁾ Readers interested in more information should consult that reference.

COUPLING METHODOLOGIES FOR SOLVING FSI PROBLEMS

While there has been an interest in solving FSI problems for decades, large computer clusters capable of solving them for full scale systems have only become widely available to engineers in the past decade. In addition, moving and morphing mesh capabilities in CFD software needed to solve FSI problems have only recently matured to the point at which they can be reliably used. This maturity was necessary before the coupling of CFD and CSM software could be expected to be successful.

The Fluid and Structural Domains

Figure 49 presents a schematic of a discretized computational domain with fluid occupying space (Ω_f) and solid body occupying space (Ω_s). The symbol Γ represents boundary conditions with the subscripts s and f referencing the solid and fluid boundaries, respectively. The numerical subscripts on the boundary conditions represent different types of boundary conditions. Application of the RANS equations for Newtonian incompressible fluids with a k-epsilon turbulence model to solve for the flow field and pressure distribution on the boundaries is a standard computational approach.

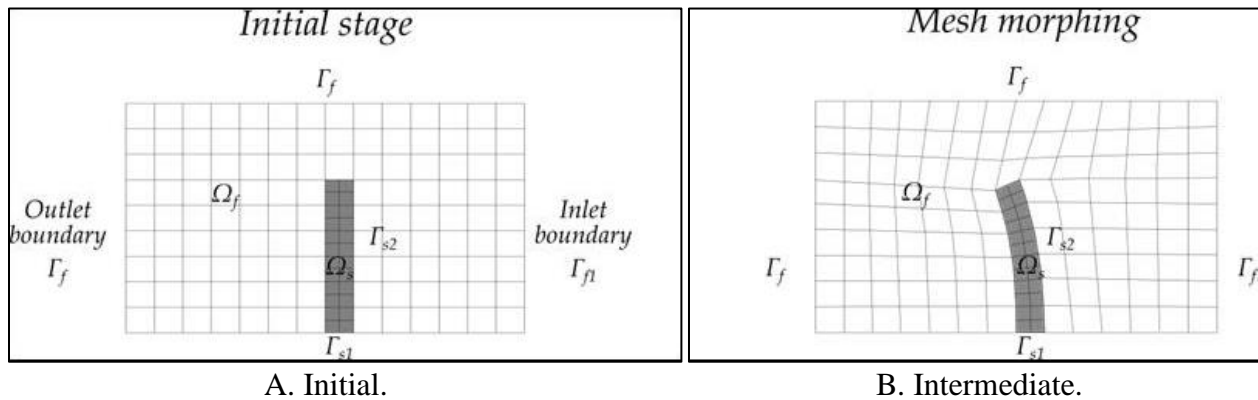


Figure 49. Schematics. Stages of FSI mesh morphing.

In most classic CFD problems, the boundaries are fixed during the analysis, and the computational mesh does not change. Notable exceptions are turbo machinery and in-cylinder combustion simulation in which special techniques were developed to handle the moving boundaries. In FSI problems, the fluid boundaries may be part of a structure that will move or deform in response to surface and body forces that are determined as part of the solution of the problem as shown in figure 50. In this case, fixed rocks in the riprap layers represent solid boundary conditions (Γ_{sl}) while the movable rocks are represented as solid body occupying

space (Ω_s). As the boundary motion is calculated, the computational mesh in the fluid domain has to be updated either by a morphing procedure or by a complete domain remesh process.

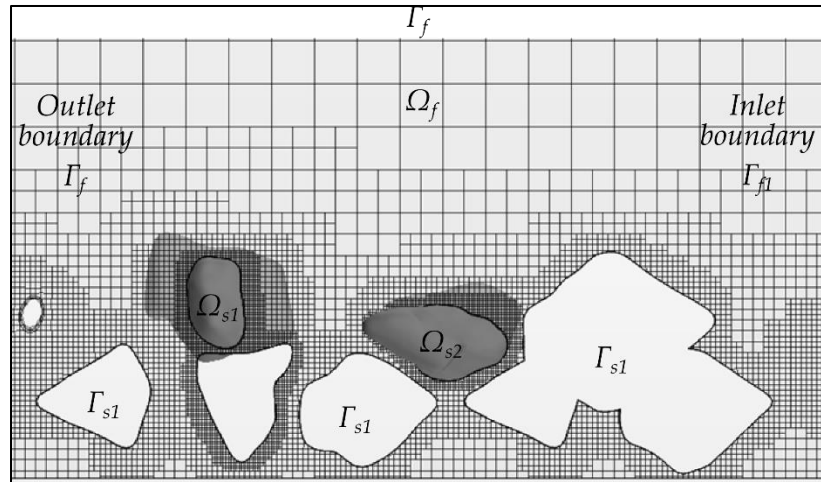


Figure 50. Sketch. Definition of the domains for FSI analysis of riprap stability.

The CFD solution of the fluid flow equations yields the detailed distribution of fluid stress on the solid surfaces. This stress distribution is passed to the CSM software to solve for the response of the solid bodies, and that solution yields the displacement rate (velocity) distribution of the solid surfaces. In general, the surface velocity distribution may include both deformation and rigid body motion. In the analysis of riprap rock motion, it includes only rigid body motion. The motion computed by the CSM software is passed back to the CFD software as a boundary condition that is a function of time.

Methodologies of Coupling Codes

In general, there are two groups of coupling solutions for FSI problems: monolithic and partitioned.⁽⁴⁰⁾ The monolithic approach involves solving the coupled set of equations for the fluid and structural domain as a single problem. Although this approach may seem the most desirable, it can be more difficult to adjust solver parameters to obtain a converged solution than with the partitioned approach. The use of robust CFD and CSM software from vendors who specialize in those areas naturally leads to using a partitioned approach in which the equations are solved iteratively one domain at a time and coupling conditions are set via file-based data exchange from the solution of the other domain.

Depending on the influence of interface boundary condition changes from either the solid or fluid domain on the other domain one-way or two-way coupling may be needed to solve the problem. If, for example, displacements of the solid resulting from fluid forces are small enough so that they do not substantially influence the fluid flow, then one way coupling from the fluid domain to the solid domain can be used. In this case, the pressure distribution on the solid is not affected much by its motion, and therefore flow equations need to be solved only once to obtain the load from the flow on the solid. However, for FSI analysis of riprap the motion of a rock results in an evolving position and orientation that substantially changes the pressure distribution over the surface of the rock, requiring two-way coupling.

Two-way coupling can be either weak or strong. In a weak coupling, as shown in figure 51, the solution in the fluid region at time step (n) including the pressure and shear stress distribution, is found on the movable riprap wall boundaries at the start of time step obtained from the structural solver from the previous step ($n - 1$). This distribution is passed subsequently to the structural solver, which yields a solution giving the solid boundary displacement and velocity that is passed to the CFD solver for use in time step ($n + 1$). The structural solver may require a smaller time step (δt_s) than the fluid solver time step (δt_f) if contact, such as a rock colliding with surrounding rocks on the bed, is modeled. The number of structural solver time steps within each fluid solver time steps is represented by a multiplier (m). The coupling time step represents the frequency of data exchange between the two solvers. The coupling time step must be an integer multiplier of both solver time steps. In figure 51, the coupling time step is equal to the fluid solver time step. The number of steps and length of time steps for each solver is determined by the complexity of the physics modeled in each solver.

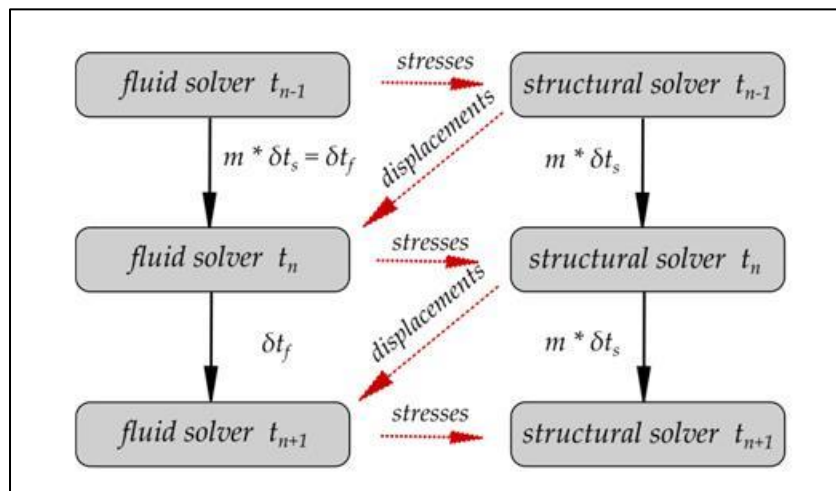


Figure 51. Flowchart. Weak FSI coupling scheme.

Figure 52 presents a schematic of a strong coupling procedure. In this scheme, the two problems are also numerically decoupled. However, within each time step (n) the CFD and CSM solvers exchange interface conditions computed by the separate solvers during the iteration (i_m) to converge during the time step. An updated location of the structure boundary in the structural step is fed to the CFD model and a new pressure field is found. Instead of progressing to the next step, the updated pressures are used again to find a different state of the structure within the same time step.

Workflow of the File-Based Data Exchange with Weak Coupling

The weak coupling for this study involved two separate solvers: STAR-CCM+ performing CFD calculations and LS-DYNA performing structural analysis.^(3,4,41) Both of these software packages have limited FSI capabilities. However, LS-DYNA does not yet have sufficiently robust fluid flow solvers and the wide range of flow physics models available in STAR-CCM+. Conversely, STAR-CCM+ recently implemented the contact capabilities for rigid bodies, but the algorithm is not able to efficiently model multiple rocks colliding with each other. A variety of models for particle-particle and particle-wall interactions exist in STAR-CCM+, but these are sub-grid

models of particles not represented in the mesh. For the purpose of analyzing the onset of motion of riprap rocks, modeling the effects of contact forces between objects represented in the mesh is an essential feature.

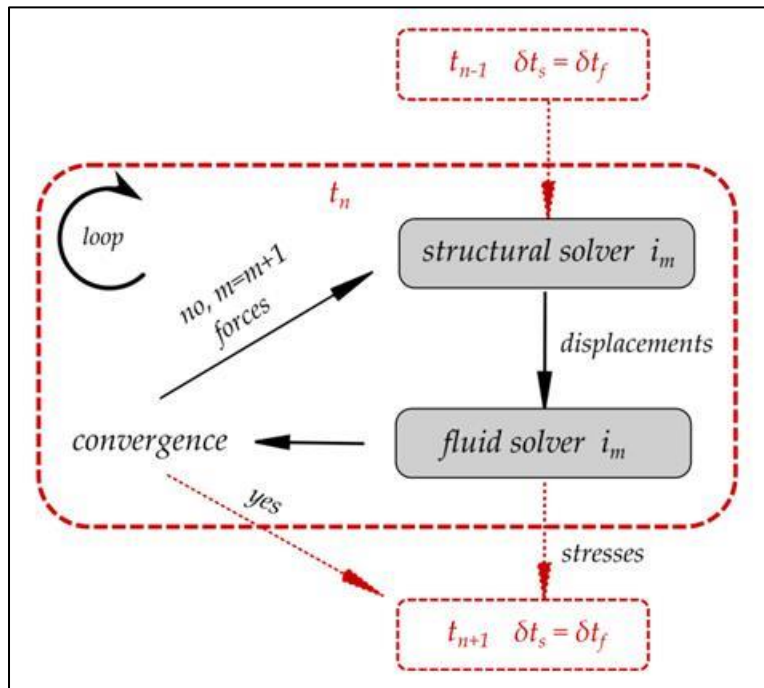


Figure 52. Flowchart. Strong FSI coupling scheme.

Therefore, the analysis is split into two different problems. STAR-CCM+ calculates the flow field and the pressure distribution on rocks. LS-DYNA calculates the motion of rocks resulting from the stresses exerted by the fluid on the rock surface and the effects of contact forces. A new position of a rock after the coupling step is subsequently imported into STAR-CCM+ as a basis for calculation at the next time step. Because the rocks are treated as rigid bodies, a weak coupling procedure is sufficient to obtain first order accuracy in the solution of rock motion. The small time step required in LS-DYNA to model body interactions and in STAR-CCM+ to maintain stable mesh morphing was assumed to be sufficient to compute the onset of rock motion and the trajectory.

Figure 53 presents the workflow of the procedure to analyze incipient motion of riprap for a given arrangement and flow velocity. The workflow is executed by a combination of tools including manual execution, macros (in Java), and a control program (in Python). The control program initiates execution of needed components of LS-DYNA and STAR-CCM+, including the solvers and meshing software. It also translates output files into a format recognized by both software packages.

The analysis procedure begins with initialization runs in both solvers. The LS-DYNA run provides the initial position of the rocks under gravity loading. This position is used as a basis for CFD domain geometry. The CFD model is run until quasi steady state conditions are achieved with all rocks stationary. Execution of the CFD part is quite complex and requires an internal Java macro to run within STAR-CCM+ to import rock displacements and map them from the

CSM mesh to the CFD mesh and vice versa. It is almost always the case that the resolution between the fluid and structural grids is different, especially when two separate solvers are handling the fluid and solid domains. STAR-CCM+ provides accurate data mappers for non-conforming meshes.⁽³⁾ This mapping is performed at each time step as the underlying mesh deforms. The displacements of the body are distributed throughout the morphed fluid domain to maintain cell quality. No cells are added or removed in the morphing process and their neighbor relationships are preserved, thus the mesh topology remains constant. The Arbitrary Lagrangian-Eulerian (ALE) algorithm is invoked to solve transport equations resulting from the moving underlying mesh.^(3,41) Furthermore, this algorithm allows for retaining the exact shape of the interface between the solid and the fluid.

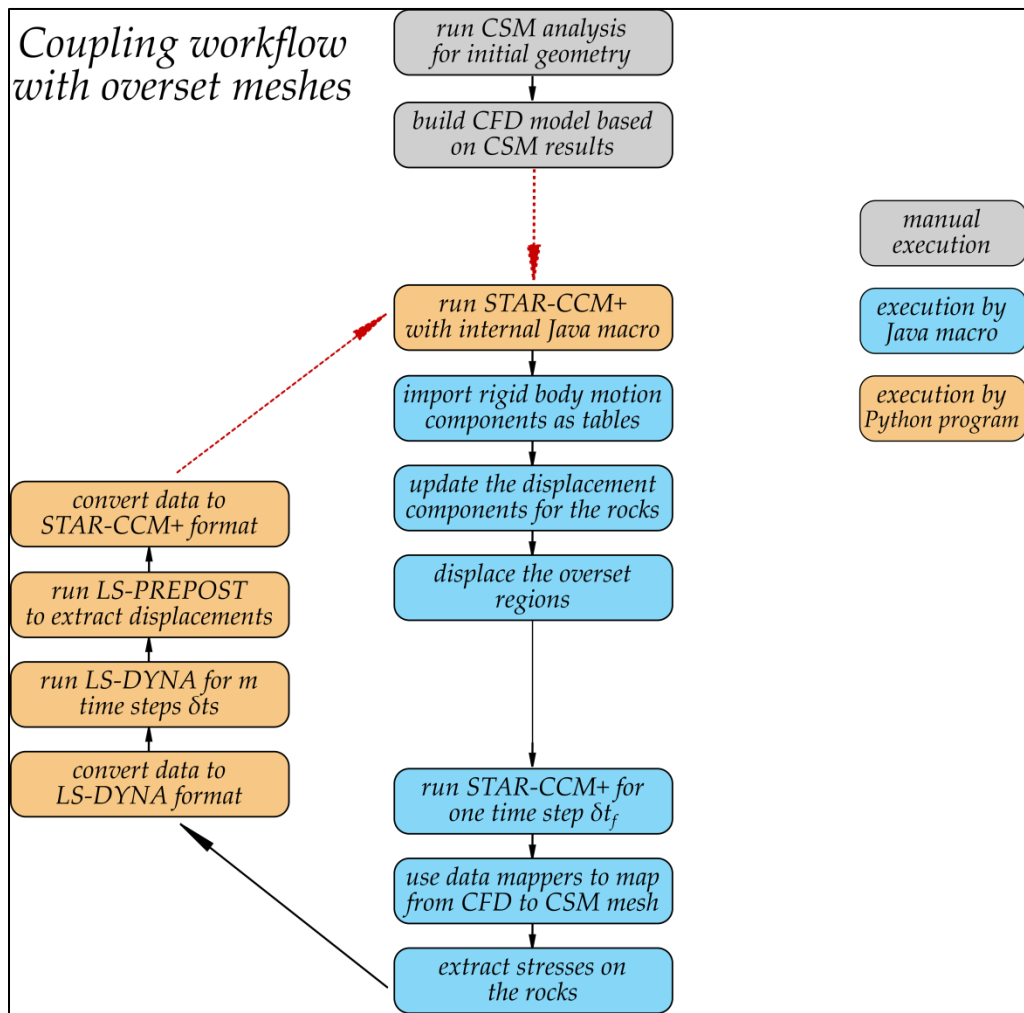


Figure 53. Flowchart. Implementation of coupling workflow between STAR-CCM+ and LS-DYNA.

Most of the effort in the FSI coupling was investing in resolving moving and morphing mesh problems that arise when rock motion collapses the space between a rock and another solid surface and problems that arose in the mapping and data exchange between the CFD and CSM software. The resolution of these problems yields coupling software for data mapping, data exchange, and automated mesh morphing failure recovery that make it possible to carry out the analysis.

The mesh morpher uses a sophisticated algorithm that yields a high-quality mesh in the whole computational domain based on the initial mesh and the displacement of the boundaries. However, in cases during which the displacement of a rock becomes large or it comes in contact with a solid boundary, the cells may become too distorted and of such poor quality that the solver either diverges or encounters a floating point exception condition. In such cases the Java macro executes a computationally demanding remeshing of the whole domain. The time step of calculations is selected such that full domain remeshing is avoided in the initial steps. The functioning of automated procedures is demonstrated in computation of water flow at increasing velocities until rock motion into the downstream occurs.

The initial proof-of-concept used the geometries of four rocks in which only the top rock was free to move as presented in figure 54-A. The coupling procedure worked very well in the first several steps. The volume mesh in STAR-CCM+ was morphed each time a new position of the moving rock was imported. However, after several remeshing cycles the shape of the moving rock started to degenerate. During the remeshing stage a standard approach was to extract the current surface mesh in STAR-CCM+ and build the new volume mesh based on that extracted surface. It was discovered that the interpolation and discretization process introduced an error forcing the fluid volume to expand slightly beyond the boundary on irregular surfaces. As a consequence, the moving rock shrinks in size through repeated remeshing operation as the water moves the movable rock off of the others as shown in the sequence of figure 54.

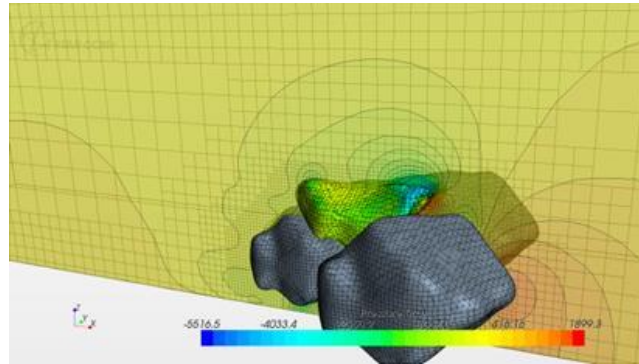
It was concluded that the only workaround for this problem was to preserve the irregular rock shape by wrapping the rock mesh with a large number of curves, called feature curves. The meshing algorithms treat features differently from general vertices defining the position of a surface. For feature curves, the meshing algorithm tries to maintain the geometry of the curve within a much smaller tolerance than that of the surface in general. Figure 55 shows the finely meshed surface of a rock with dense feature curves.

Challenges of Commercial Software and an Overset Mesh Alternative

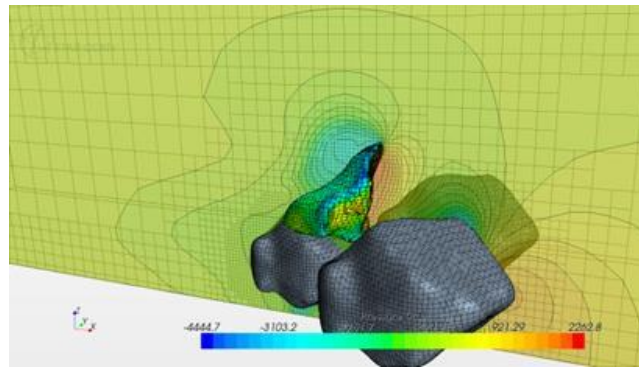
Using commercial software rather than research software has many advantages. The primary advantage is the large industrial user base engaged in using commercial software successfully to solve problems. Consequently, computed results are reliable within the accuracy of the physics models used. Vendors responding to the needs of industry also implement a wide array of physics models, methods to solve a variety of moving mesh problems, and advanced solver algorithms. They normally provide a means for users to add new physics models in the form of user defined subroutines or functions. As such, they provide an excellent foundation for building models to solve new problems, or analyze classic problems using advanced analysis techniques.

One disadvantage of using commercial software is that the users do not normally have direct access to the source code and therefore cannot make even minor modifications that might be needed for a new model development outside of the means provided by the vendor. That confines the user to the set of models and tools provided by the vendor. The current implementation of coupling between STAR-CCM+ and LS-DYNA allows for capturing the main effects of rock motion, however, when domain remeshing occurs, some of the information about the motion of a rock through time is lost. In addition, the grid fluxes are not included in the momentum equations immediately after remeshing. As a result, the reduction in drag from the

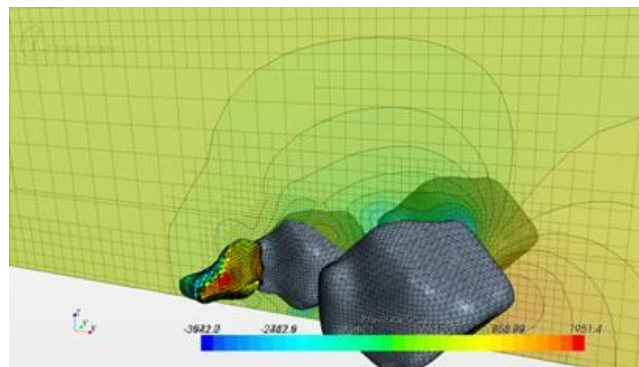
acceleration of a rock is not fully considered and rock motion with large displacements will occur at a slightly lower velocity difference between the rock and mean flow. The error in this case is conservative in the sense that it would lead to slightly oversizing the riprap for a particular application. At the onset of motion the displacements and velocities of the rocks are so small that this effect should be small.



A. Initial.



B. Intermediate.



C. Final.

Figure 54. Schematics. Stages in the coupled simulation for water induced rock motion.

The fact that only a weak coupling was implemented has its advantages and disadvantages. The obvious advantage is the computational time. Because within each coupling time step there are no inner iterations and only one exchange of the data is performed per time step, this type of coupling is sometimes called explicit. For flexible structures vibrating in the flow frequently this approach diverges quickly and a strong coupling (implicit) is needed to stabilize the solution. For

rigid rocks this behavior was not observed and weak coupling was assumed to be sufficient for this work.

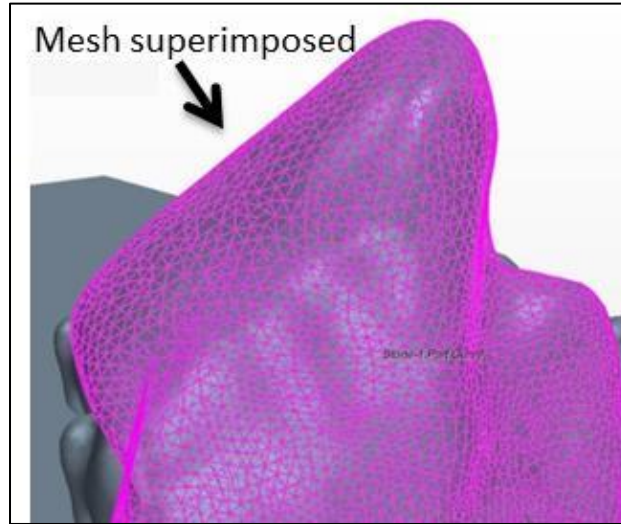


Figure 55. Graphic. Rock representation with feature curves created on all edges of the mesh.

While the coupling procedure was under the development for this study, Siemens introduced a new approach to modeling the motion of objects within the computational domain using so-called overset meshes. This approach does not rely on morphing and remeshing of the domain. Instead, it encapsulates a moving object in its own small domain that shares the space with the background global domain. During the computation, the background mesh is carved out in the place where the local mesh is and new internal boundaries are built between the local and the global mesh. The results are interpolated from the global mesh to the local mesh on these boundaries and the local mesh is treated as a part of the global model. Potentially, this method offers several advantages for modeling FSI problems: (1) reduction of overall run time because there is no need for time consuming remeshing, (2) improvement of stability because only one mesh is used throughout the simulation, and (3) improved accuracy.

In the new procedure, an overlap of the subregions and the background mesh is computed at each time step and an interpolation interface between these regions is redefined accordingly. Active and inactive cells are found in the rock and background regions at the beginning of each time step. In addition, motion of the overset regions is defined as rigid body motion based on the calculations performed in LS-DYNA (or internal finite element solver of STAR-CCM+). For overset regions, rigid body motion is specified by using just six components per time step. Previously, a displacement vector for each vertex on the rock boundary was defined separately.

The overset mesh procedure is more computationally efficient than the procedure based on mesh morphing and remeshing. The coupling iterations were executed faster than the previously described implementation. However, while the procedure with overset meshes solves some problems, it introduces new ones. When tracing the forces acting on a single rock during its motion, it was noticed that this approach generates unrealistically high forces on the rocks that do not converge to reasonable values within one time step.

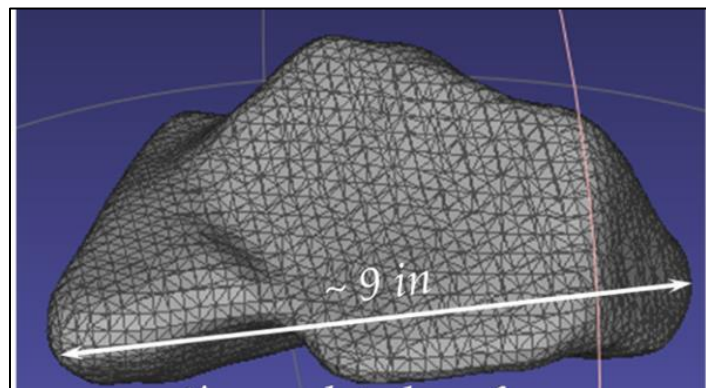
The overset mesh method has been under heavy development and improvements are expected in future releases of STAR-CCM+. In addition, recent implementations of the overset mesh approach also allow for contact between moving objects and wall boundaries. Initial tests indicated that the implementation of contact algorithms in STAR-CCM+ is not robust yet. However, with the short development cycles of STAR-CCM+ it may be possible to simulate the entire FSI riprap problem in STAR-CCM+ only once these components and models work well together with the finite element solver internal to STAR-CCM+ in the near future.

At the time of this study, the procedure with morphing and remeshing seems to be conceptually most reliable and it appears to generate the most stable results. In addition, the results from the procedure are conservative. Therefore, it was used to perform all the calculations reported in this study.

APPLICATION OF THE METHODOLOGY TO A SIMPLE RIPRAP CASE

The coupling procedures described in this report were developed primarily for analyzing incipient motion of rocks used in riprap around piers or abutments to prevent scour of the riverbed at these structures. Prior to this more complex case, a simple, flatbed geometry case with only riprap rocks was used as a development case until all of coupling problems were resolved. This simple case also allowed for comparison with Laursen's and Neill's equations for critical velocities.⁽⁴²⁾

Model development started by processing the surface point cloud data from a 3D laser scan of a rock to be used in the demonstration. MeshLab software was used to generate a surface triangulation of the rock as shown in figure 56.⁽¹²⁾ The initial shape was subsequently modified by simple geometrical operations to create a set of rocks with similar shapes to populate the domain for testing.

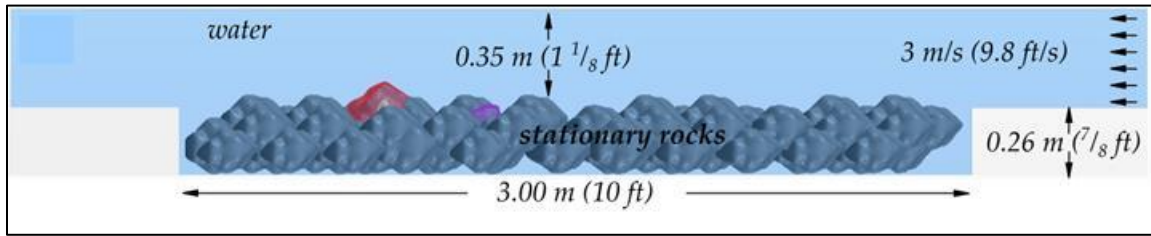


1 inch = 25.4 mm

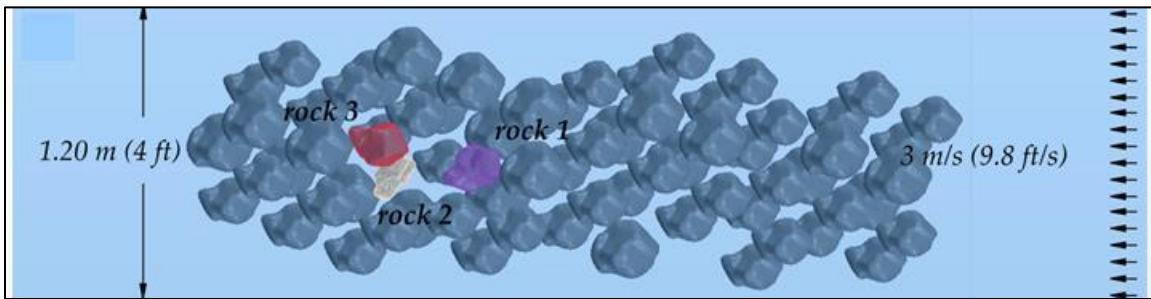
Figure 56. Graphic. Surface triangulated representation of a rock.

Two layouts were considered for these simple tests. Layout 1 is placement of a riprap layer in a depressed section so that the top of the layer is flush with the surrounding surface. Profile and plan views are shown in figure 57-A and figure 57-B respectively. Layout 2 includes an abutment along with a similar riprap layout as shown in figure 57-C. All of the rocks in the figure are stationary except for the three individually labeled as rock 1, rock 2, and rock 3. The

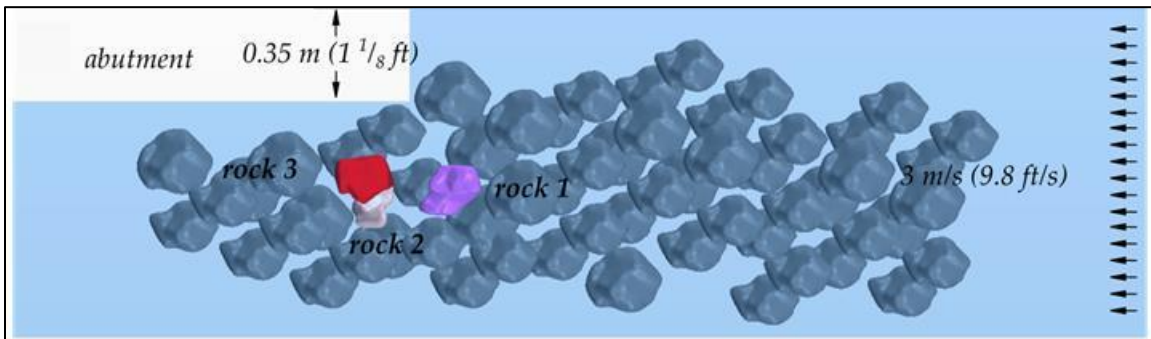
movable rocks can interact with other boundaries and among themselves through contact algorithms enabled in LS-DYNA.



A. Layout 1, profile view.



B. Layout 1, plan view.



C. Layout 2, plan view.

Figure 57. Graphics. Test CFD models.

Rock shapes and layout influence when they are picked up and moved by the passing flow. Placing the rocks at different locations ensures that each of them will have a different critical velocity determined by the detailed geometry and flow field computed in the simulation. Rock 1 and rock 2 are the same shape as the originally scanned rock in figure 56. Rock 1 is placed flush among the other rocks in the bed. Rock 2 is placed quite deep under the top surface. Rock 3 is bigger and more round than the other two and is protruding slightly above the bed.

A CFD domain was built with dimensions 16.4 ft long, 3.94 ft wide, and 2.1 ft high (5.0 m long, 1.2 m wide, and 0.65 m high) in the recessed area containing the rocks of the riprap layer. The height of the water from the top to the riprap bed top surface was approximately 1.15 ft (0.35 m). The size of the domain was designed to be small to conserve computational resources and provide fast turnaround times during development and testing of the coupling procedures. A single phase rigid lid model of the channel flow was used to keep the model simple.

The initial water velocity in the domain and the velocity at the inlet was a variable parameter that was manually set for each test. The sides of the domain were set as symmetric planes. The downstream end of the model was set as an outflow boundary. In layout 2 (with the abutment), the abutment was set as a wall boundary and the approach flow boundary on the abutment side of the domain was also set as wall boundary. The opposite side was set as a symmetry plane.

The domain was meshed using hexahedral cells with varying cell size from 0.16 inches (0.004 m) around the rocks up to 2.4 inches (0.06 m) away from the rocks and other boundaries. The total count of cells in the model varied between 1.5 million up to 2.0 million cells depending on the layout (without or with abutment) and the evolving position of rocks during the simulation. A k-epsilon turbulence model with RANS equations was used to solve for the flow field. An implicit unsteady solver with time step of 0.01 s was used in the flow solver. The same time step was also used as the coupling time step, that is, the rate at which data between the CFD and CSM solvers was exchanged.

In LS-DYNA, the rocks were modeled as rigid bodies with a density similar to granite: 0.091 T/ft³ (2.9 t/m³). The mass of rocks 1 and 2 were each 4.1 kg (9.0 lb) and the mass of rock 3 was 7.1 kg (15.6 lb).

Three contact definitions were incorporated in the model: (1) among the moving rocks, (2) between the moving rocks and the stationary rocks, and (3) between the moving rocks and the boundaries. It is sometimes advantageous in LS-DYNA to wrap solid bodies with null, massless shell elements to have more flexibility in defining the contact properties. One of advantages of such an approach is the use of a non-zero thickness layer around the rocks that prevents them from coming into a full contact in STAR-CCM+. Using this method prevents morphed cells in a near contact zone from being squeezed to near zero volume and causing flow acceleration to unrealistically high velocities in crevices.

The time step of calculations in the LS-DYNA explicit solver was set to 4.5×10⁻⁶ s. Use of the explicit solver and a small time step was needed to stabilize the contact forces between rocks colliding with other rocks or wall boundaries. A time step that is too large can cause excessive contact forces and abnormal behavior of the rocks. Once the STAR-CCM+ and LS-DYNA models were initialized, the coupling between them was activated.

The velocities at which motion for the movable rocks was initiated were compared with estimated critical velocities as a partial evaluation of the FSI simulations. Approximate values for critical velocity of the modeled rocks can be found by using the Neill and Laursen equations, both of which are applicable to the rock sizes being modeled.⁽⁴²⁾ Laursen's equation is given by the equation in figure 58.

$$V_{CL} = K_u y^{1/6} D_{50}^{1/3}$$

Figure 58. Equation. Laursen's equation for critical velocity.

Where:

V_{CL} = Critical velocity estimated from Laursen's equation (ft/s (m/s)).

K_U = Unit conversion constant (11.7 for US customary units (6.19 for SI units)).

y = Flow depth (ft (m)).

D_{50} = Median particle size (ft (m)).

For median particle sizes above 0.1 ft (0.03 m), Neill's equation for critical velocity is defined in figure 59.

$$V_{CN} = 11.5K_u y^{1/6} D_{50}^{1/3}$$

Figure 59. Equation. Neill's equation for critical velocity.

Where:

V_{CN} = Critical velocity estimated from Neill's equation (ft/s (m/s)).

K_U = Unit conversion constant (1 for US customary units (0.55217 for SI units)).

Taking $y = 1.15$ ft (0.35 m) and $D_{50} = 0.79$ ft (0.24 m), the critical velocities are 10.8 ft/s (3.31 m/s) and 10.6 ft/s (3.23 m/s) according to Neill and Laursen, respectively.

The computer simulations were run with inlet velocities of 6.6, 8.2, and 9.8 ft/s (2.0, 2.5, and 3.0 m/s) for each of the two layouts. The simulations were observed for motion of the movable rocks. For both layouts (without and with the abutment) motion was not observed at an inlet velocity of 6.6 ft/s (2.0 m/s). Because this velocity is less than the estimated critical velocity from both Neill and Laursen, motion was not expected. At a velocity of 8.2 ft/s (2.5 m/s) local motion (rocking in place) of rock 3 was noticeable, but it did not move from its position. Recall that rock 3 is the largest of the three movable rocks, but also is the most exposed to the flow field.

At a velocity of 9.8 ft/s (3.0 m/s) for layout 1 (without abutment), rock 3 was lifted out of position and moved downstream as shown in the time series of graphics shown in figure 60. (Several of the stationary rocks were removed from the view to more easily see the position of the moving rocks.) The figure also displays a semi-transparent cross-section through the domain showing the velocity distribution in the flow field. In addition to the displacement of rock 3, rock 2 exhibited local motion, but did not leave its position.

Similarly, at a velocity of 9.8 ft/s (3.0 m/s) for layout 2 (with abutment), rocks 1 and 3 were lifted out of position and moved downstream as shown in the time series in figure 61. The presence of the abutment altered the flow field and altered the movable rock responses, as a result.

Simulated rock movement at 9.8 ft/s (3.0 m/s), in both layouts, occurred at a velocity less than 10 percent lower than the values anticipated by the Laursen and Neill equations. It had been noted previously that the use of the closed lid approximation would result in rock motion at somewhat lower velocities than would be observed in the physical world. Therefore, this test was considered to be a successful demonstration of the coupled FSI modeling developed for this study.

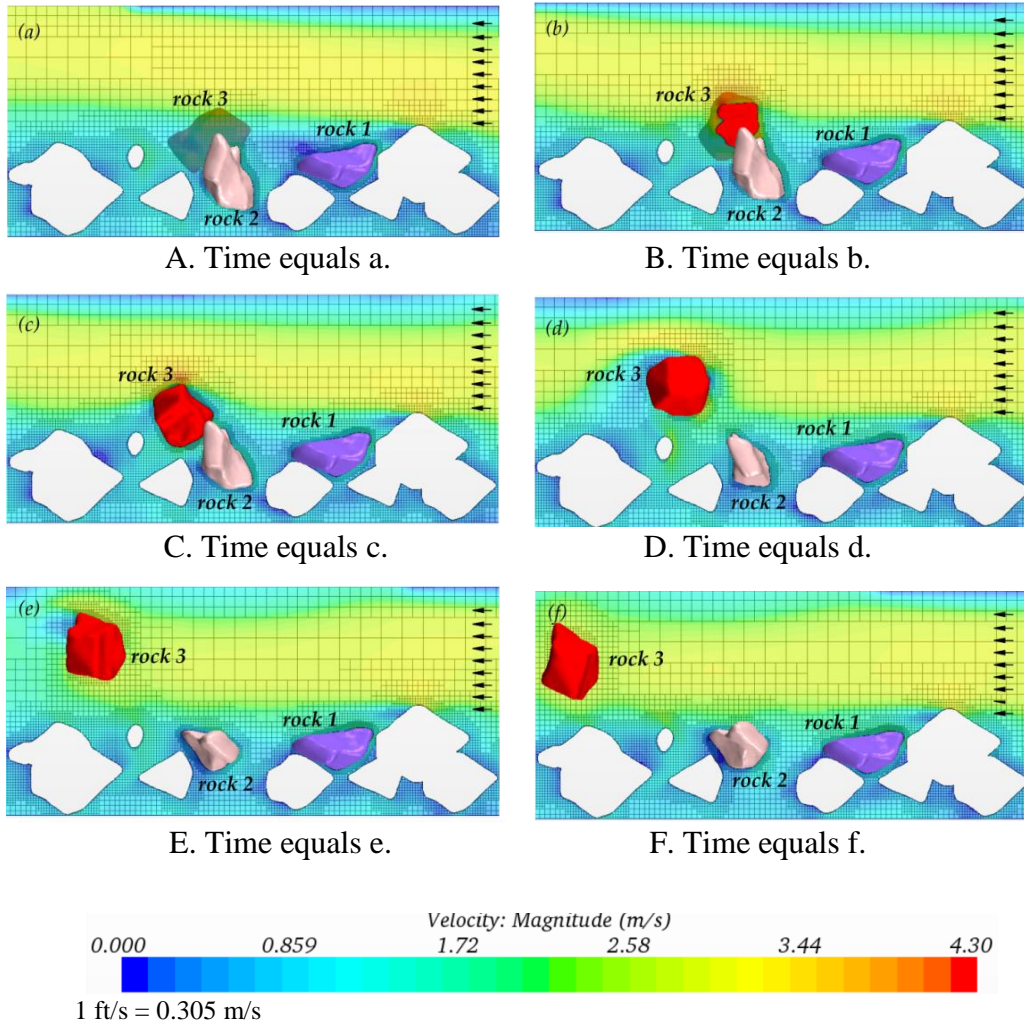


Figure 60. Graphics. Time series for layout 1 at an inlet velocity of 9.8 ft/s (3.0 m/s).

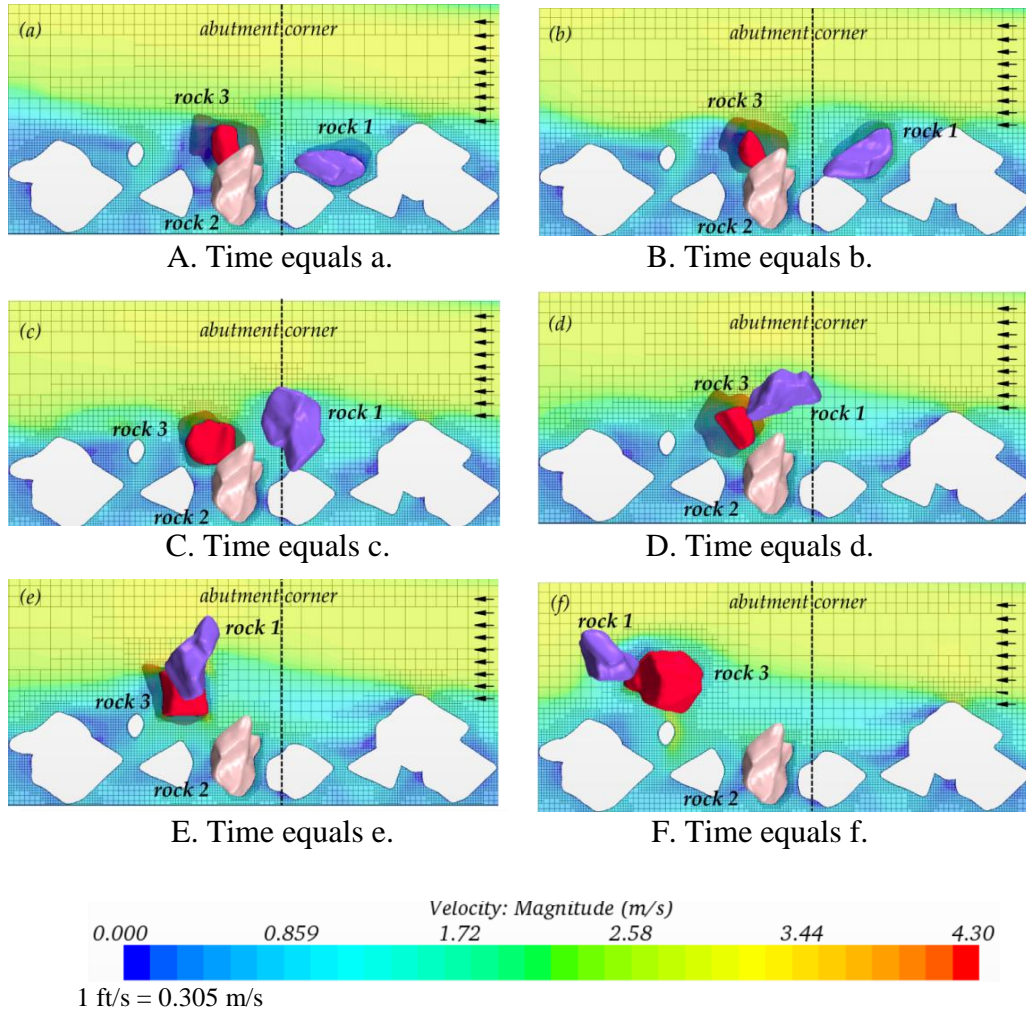


Figure 61. Graphics. Time series for layout 2 at an inlet velocity of 9.8 ft/s (3.0 m/s).

VERIFICATION OF THE COUPLING MECHANISM BY COMPARISON WITH A STAR-CCM+/ABAQUS BENCHMARK FSI PROBLEM

The STAR-CCM+ manual contains an FSI example solved in a coupled system of STAR-CCM+ and Abaqus. STAR-CCM+ has a built-in interface for this coupling that allows for strong and weak coupling of the codes. For verification purposes this same FSI example problem was also solved using coupling procedure developed for this study.

The problem is to model the vibrations of a flexible rectangular plate standing in a 32.8 ft/s (10 m/s) cross wind as shown in figure 62. The plate is constrained at its bottom edge perpendicular to the wind flow. The plate is 0.33 ft high, 0.26 ft wide, and 0.0082 ft thick (0.1 m high, 0.08 m wide, and 0.0025 m thick). The flexible plate was modeled with the following elastic properties and material constants: (1) Young's modulus of 5570 lbf/in² (38.4 MPa), (2) Poisson's ratio of 0.3, and (3) density of 255 lb/ft³ (4096 kg/m³). The model domain has a width, height, and length of 0.95 ft, 0.66 ft, and 2.95 ft (0.29 m, 0.2 m, and 0.9 m), respectively, with the plate located 1.3 ft (0.4 m) from the model inlet.

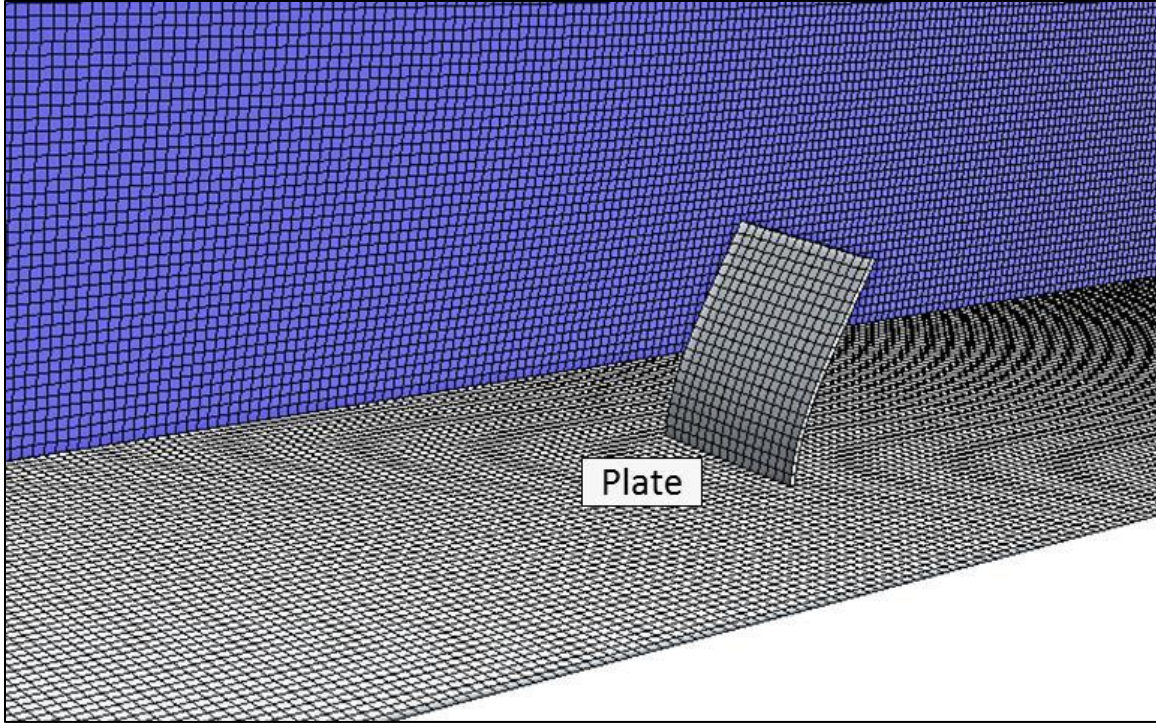
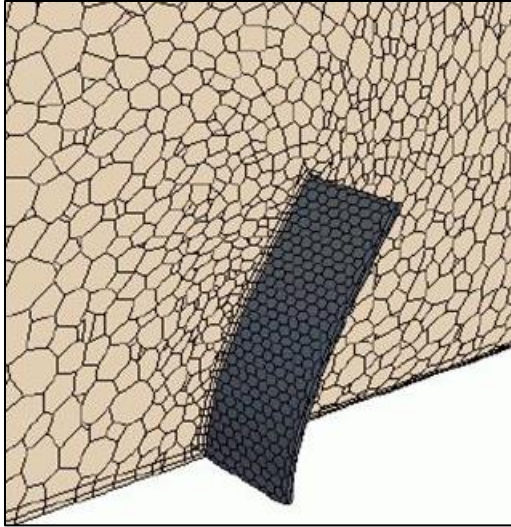
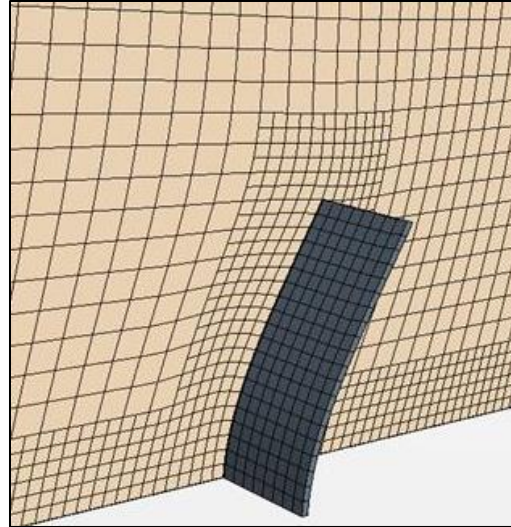


Figure 62. Schematic. CFD domain and grid for analysis of flexible plate protruding into the flow setup for FSI analysis coupling with LS-DYNA.

Figure 63 shows the mesh in proximity to the deformed plate for the coupling with Abaqus and LS-DYNA. The domain was modeled in Abaqus with polyhedral cells and in LS-DYNA with hexahedral cells. The overall model was built with around 300,000 cells. The configuration shown is captured at the state of the largest deflection of the plate. Figure 64 shows the displacement history of the two top corners of the plate. The maximum amplitude and the period of vibrations were predicted to be about the same magnitude by both coupling mechanisms. The local oscillations of corners of the plate behaved slightly differently. This was attributed to differences in coupling handling and different theoretical formulation of the solid elements. The comparison between the two modeling approaches showed general agreement.

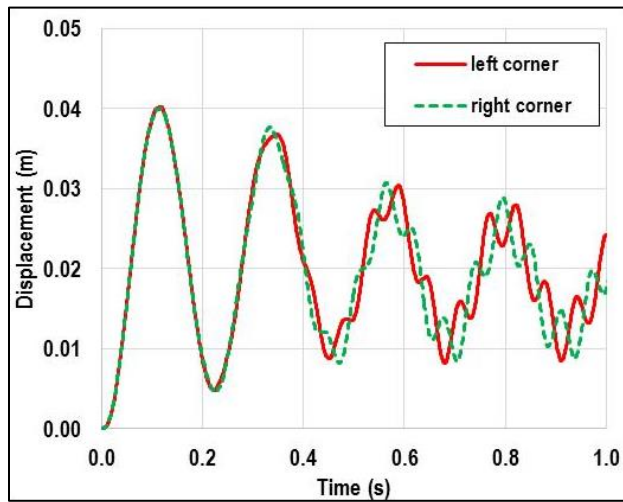


A. Abaqus coupling.



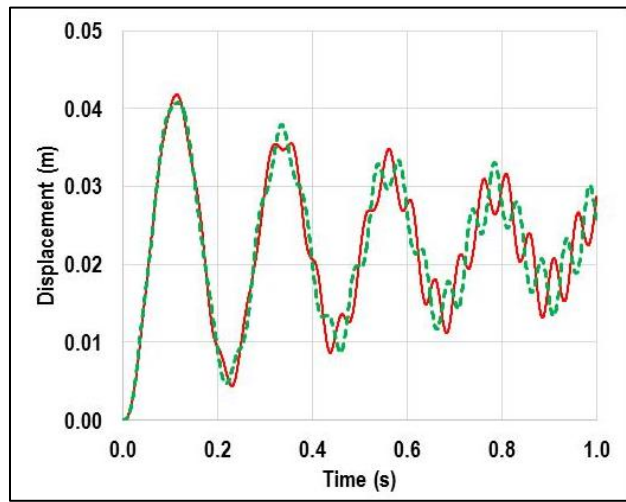
B. LS-DYNA coupling.

Figure 63. Schematics. Morphed mesh at maximum plate deflection.



1 ft = 0.305 m

A. LS-DYNA-STAR-CCM+ coupling.



1 ft = 0.305 m

B. Abaqus - STAR-CCM+ coupling.

Figure 64. Graphs. Plate deflection.

REFERENCES

1. Lagasse, P.F., Clopper, P.E., Pagán-Ortiz, J.E., Zevenbergen, L.W., Arneson, L.A., Schall, J.D., and Girard, L.G. (2009). *Bridge Scour and Stream Instability Countermeasures, Experience, Selection, and Design Guidelines, volumes 1 and 2*, Hydraulic Engineering Circular No. 23, Third Edition, Federal Highway Administration, FHWA-NHI 09-111 and -112, Washington, DC.
2. Lagasse, P.F., Clopper, P.E., Zevenbergen, L.W., and Ruff, J.F. (2006). *Riprap Design Criteria, Recommended Specifications, and Quality Control*, NCHRP Report 568, Transportation Research Board, National Academies of Science, Washington, DC.
3. STAR-CCM+ version 8.02 [Computer software]. CD-Adapco, Melville, NY.
4. LS-DYNA version 971 [Computer software]. Livermore Software Technology Corporation, Livermore, CA.
5. Lagasse, P.F., Clopper, P.E., Zevenbergen, L.W., and Girard, L.G. (2007). *Countermeasures to Protect Bridge Piers from Scour*, NCHRP Report 593, Transportation Research Board, National Academies of Science, Washington, DC.
6. Melville, B.W. and Coleman, S.E. (2000). *Bridge Scour*, p. 550, Water Resources Publications, LLC, Highlands Ranch, CO.
7. Centre for Civil Engineering Research and Codes (CUR). (1995). *Manual on the Use of Rock in Hydraulic Engineering*, A.A. Balkema Publishers, Brookfield, VT.
8. Richardson, E.V. and Lagasse, P.F. (eds.). (1999). *Stream Stability and Scour at Highway Bridges*, Compendium of Papers, ASCE Water Resources Engineering Conferences 1991–1998, American Society of Civil Engineers, Reston, VA.
9. Pagán-Ortiz J.E. (1991). *Stability of Rock Riprap for Protection at the Toe of Abutments Located at the Floodplain*, FHWA-RD-91-057, Federal Highway Administration, Washington, DC.
10. Bojanowski, C., Lottes, S.A., Kerényi, K., and Shen J. (In press). *Development of a Computational Approach to Detect Instability and Incipient Motion of Large Riprap Rocks*, Argonne National Laboratory, Department of Energy, Washington, DC.
11. Flora K., (2014). *Advanced Hydraulic Report for Pier Riprap Stability, Middle Fork Feather River Br. N. 09-0063*, California Department of Transportation, Sacramento, CA.
12. MeshLab [Computer software]. ISTI-CNR Research Center, Pisa, Italy.
13. Matlab [Computer software]. Mathworks, Natick, MA.

14. Engels, H. (1929). "Experiments Pertaining to the Protection of Bridge Piers Against Undermining," *Hydraulic Laboratory Practice*, Chapter V, American Society of Mechanical Engineers, New York.
15. de Sousa, Pinto, L.N. (1959). *Riprap Protection Against Scour Around Bridge Piers*," thesis submitted in partial fulfillment of the requirements for the degree of Master of Science in the Department of Mechanics and Hydraulics in the Graduate College of the State University of Iowa, Iowa City, IA.
16. Ruff, J.F. and Nickelson, J.R. (1993). "Riprap Coverage Around Bridge Piers," in Richardson, E.V. and Lagasse, P.F. (eds.), (1999), *Stream Stability and Scour at Highway Bridges*, Compendium of Papers, ASCE Water Resources Engineering Conferences 1991–1998, American Society of Civil Engineers, Reston, VA.
17. Parola, A.C. (1995). "Boundary Stress and Stability of Riprap at Bridge Piers," in Thorne, C.R., Abt, S.R., Barends, F.B.J., Maynard, S.T., and Pilarczyk, K.W. (eds.), *River, Coastal, and Shoreline Protection: Erosion Control Using Riprap and Armourstone*, pp. 149–158, John Wiley & Sons Ltd., Chichester, UK.
18. Posey, C.J. (1981). "Test of Scour Protection for Bridge Piers," *Journal of the Hydraulics Division*, pp. 1773-1783, American Society of Civil Engineers, Reston, VA.
19. Hjorth, P. (1975). *Studies on the Nature of Local Scour*, Bulletin, Series A, No. 46, Institutionen for Teknisk Vattenresurslara, Lund, Sweden.
20. Bertoldi, D.A., Jones, S.J., Stein, S.M., Kilgore, R.T., and Atayee, A.T. (1996). *An Experimental Study of Scour Protection Alternatives at Bridge Piers*, FHWA-RD-95-187, Federal Highway Administration, Washington, DC.
21. Chiew, Y.M. (1995). "Mechanics of Riprap Failure at Bridge Piers," *Journal of Hydraulic Engineering*, 121(9), pp. 635–643, American Society of Civil Engineers, Reston, VA.
22. Lim, F.H. and Chiew, Y.M. (1996). "Stability of Riprap Layer Under Live-Bed Conditions," in Maxwell, W.H.C., Preul, H.C., and Stout, G.E. (eds.), *Proceedings Rivertech96: 1st International Conference on New/Emerging Concepts for Rivers*, 2, pp. 830–837, Chicago, IL.
23. Lim, F.H. and Chiew, Y.M. (1997). "Failure Behavior of Riprap Layer Around Bridge Piers," in: Holly, F.M., Jr., Alsaffar, A., English, M., and Szollosi-Nagy, A. (eds.), *Managing Water: Coping with Scarcity and Abundance*, pp. 185-189, Proceedings of Theme A, 27th IAHR Congress, San Francisco, CA.
24. Melville, B.W., Lauchlan, C.S., and Coleman, S.E. (1997). "Pier Riprap Protection," in Richardson, E.V. and Lagasse, P.F. (eds.) (1999), *Stream Stability and Scour at Highway Bridges*, Compendium of Papers, ASCE Water Resources Engineering Conferences 1991–1998, American Society of Civil Engineers, Reston, VA.

25. Melville, B.W., Lauchlan, C.S., and Hadfield, A.C. (1997). "Bridge Pier Scour Countermeasures," in Wang, S.S.Y., Langendoen, E.J., and Shields, Jr., F.D., (eds.), *Proceedings of the Conference on Management of Landscapes Disturbed by Channel Incision: Stabilization, Rehabilitation, Restoration*, Oxford, MS.
26. Hoffmans, G.J.C.M. and Verheij, H.J. (1997). *Scour Manual*, A.A. Balkema Publishers, Brookfield, VT.
27. Bonasoundas, M. (1973). *Strömungsvorgang und Kolkproblem*, Report No. 28, Oskar V. Miller, Institut, Tech. Univ., Munich, Germany.
28. Parker, G., Toro-Escobar, C., and Voigt, R.L. Jr. (1998). *Countermeasures to Protect Bridge Piers from Scour*, Users Guide (revised 1999) and Final Report, NCHRP Project 24-07(1), p. 360, Transportation Research Board, Washington, DC.
29. Fotherby, L.M. and Ruff, J.F. (1999). "Riprap and Concrete Armor to Prevent Pier Scour," in Richardson, E.V. and Lagasse, P.F. (Eds.), *Stream Stability and Scour at Highway Bridges*, Compendium of Papers, ASCE Water Resources Engineering Conferences 1991 to 1998, pp. 893-904, American Society of Civil Engineers, Reston, VA.
30. Chiew, Y.M. and Lim, F.H. (2000). "Failure Behavior of Riprap Layer at Bridge Piers Under Live-Bed Conditions," *Journal of Hydraulic Engineering*, ASCE, 126(1), pp. 43–55, American Society of Civil Engineers, Reston, VA.
31. Lim, F.H. and Chiew, Y.M. (2001). "Parametric Study of Riprap Failure Around Bridge Piers," *Journal of Hydraulic Research*, 39(1), pp. 61–72, Taylor and Francis Group, Oxford, UK.
32. Lauchlan, C.S. and Melville, B.W. (2001). "Riprap Protection at Bridge Piers," *Journal of Hydraulic Engineering*, 127(5), pp. 412–418, American Society of Civil Engineers, Reston, VA.
33. Parola, A.C. (1993). "Stability of Riprap at Bridge Piers," *Journal of Hydraulic Engineering*, 119(10), pp. 1080–1093, American Society of Civil Engineers, Reston, VA.
34. Chiew, Y.M. (2004). "Local Scour and Riprap Stability at Bridge Piers in a Degrading Channel," *Journal of Hydraulic Engineering*, 130(3), pp. 218–226, American Society of Civil Engineers, VA.
35. Arneson, L.A., Zevenbergen, L.W., Lagasse, P.F., and Clopper, P.E. (2012). *Evaluating Scour at Bridges*, Fifth Edition, Federal Highway Administration, Report FHWA-HIF-12-003, Hydraulic Engineering Circular No. 18, U.S. Department of Transportation, Washington, DC.
36. National Highway Institute. (2009). *Stream Instability, Bridge Scour, and Countermeasures: A Field Guide for Bridge Inspectors*, FHWA-NHI-08-106, Federal Highway Administration, Department of Transportation, Washington, DC.

37. Brice, J.C. and Blodgett, J.C. (1978). *Countermeasure for Hydraulic Problems at Bridges, volumes 1 and 2*, FHWA-RD-78-162 and -163, U.S. Geological Survey, Federal Highway Administration, Washington, DC.
38. Blodgett, J.C. and McConaughy, C.E. (1986). *Rock Riprap Design for Protection of Stream Channels Near Highway Structures, Volume 2 – Evaluation of Riprap Design Procedures*, Water Resources Investigations Report 86-4128, U.S. Geological Survey, prepared in Cooperation with Federal Highway Administration, Washington, DC.
39. National Cooperative Highway Research Program. (1999). "1998 Scanning Review of European Practice for Bridge Scour and Stream Instability Countermeasures," *Research Results Digest, 241*, Transportation Research Board, Washington, DC.
40. Hou G., Wang J., and Layotn A. (2012). "Numerical Methods for Fluid Structure Interaction – A Review," *Communication in Computational Physics, 12*(2), pp. 337–377, Cambridge University Press, Cambridge UK.
41. Livermore Software Technology Corporation. (2013). *Incompressible Fluid Solver in LS-DYNA*, Livermore Software Technology Corporation, Livermore, CA.
42. Kerenyi K., Jones J., and Stein S. (2007). *Bottomless Culvert Scour Study: Phase II Laboratory Report*, FHWA-HRT-07-026, U.S. Department of Transportation, Washington, DC.
43. Lauchlan, C.S. (1999). *Pier Scour Countermeasures*, Ph.D. Thesis, University of Auckland, Auckland, NZ.*

*Revised 10/17/18.

ACKNOWLEDGMENT*

Figure 1 was modified by FHWA from figure 2.5 of NCHRP report 568, which in turn was modified from an original graph in C.S. Lauchlan's thesis, "Pier Scour Countermeasures."⁴³

*Revised 10/17/18.

